

Thin-film flow in helical channels

David John Arnold

Thesis submitted for the degree of
Doctor of Philosophy
in
Applied Mathematics
at
The University of Adelaide
School of Mathematical Sciences

June 2016



THE UNIVERSITY
of ADELAIDE

Abstract

In this thesis, we study fluid flows in helical channels. The primary motivating application for this work is the segregation of particles of different weights/densities in spiral particle separators, devices used in the mining and mineral processing industries to separate ores and clean coal. These devices feature very shallow flows, and so we use the thin-film approximation which enables significant analytic progress. It is most convenient to use a non-orthogonal, helicoidal coordinate system which allows a natural representation of helical channels with arbitrary cross-sectional profile, and arbitrary centreline slope and radius. We begin by studying particle-free flow in channels with rectangular cross-section. On taking the thin-film limit of the Navier-Stokes equations, we obtain a system of equations which has an analytic solution. This solution is investigated to determine the effects of changing the slope and curvature of the channel centreline, and the fluid flux down the channel. We then consider particle-free flow in helical channels with shallow, but otherwise arbitrary cross-section, and investigate the effect of changing the cross-sectional shape of the channel, guided in part by questions raised from studying rectangular channels. Except in a special case, this model must be solved numerically. Finally, we consider monodisperse particle-laden flow, using the diffusive-flux model proposed by Leighton and Acrivos (1987). We present the thin-film particle-laden flow model for shallow channels of arbitrary geometry and, assuming the particles are uniformly distributed in the vertical direction, solve the resulting system of equations numerically. We conclude by outlining future research directions.

Signed Statement

I certify that this work contains no material which has been accepted for the award of any other degree or diploma in my name in any university or other tertiary institution and, to the best of my knowledge and belief, contains no material previously published or written by another person, except where due reference has been made in the text. In addition, I certify that no part of this work will, in the future, be used in a submission in my name for any other degree or diploma in any university or other tertiary institution without the prior approval of the University of Adelaide and where applicable, any partner institution responsible for the joint award of this degree.

I consent to this copy of my thesis, when deposited in the University Library, being available for loan and photocopying, subject to the provisions of the Copyright Act 1968.

I also give permission for the digital version of my thesis to be made available on the web, via the University's digital research repository, the Library Search and also through web search engines, unless permission has been granted by the University to restrict access for a period of time.

SIGNED: DATE:

Acknowledgements

I wish to thank my supervisors, A. Prof. Yvonne Stokes and Dr Ed Green for all their help over the last few years. Not only have they given me so much of their expertise, but they have helped me to learn how to be a researcher in mathematics. I remain grateful for the time they have given me, and for the opportunities and introductions that they have given me.

I would also acknowledge Prof. Brian Duffy and Dr Stephen Wilson, for their comments on the paper that became chapter 4, and Dr Glen Wheeler for useful advice regarding the non-orthogonal coordinate system.

I also thank my fellow postgraduate students, particularly Ben, Mingmei, David, and Nic, who helped to make my postgraduate study as enjoyable as it was.

Finally, I thank my parents, Clive and Anne, for their unfailing support, and Michael and Emma, for doing so much to help me in so many ways.

Contents

1	Introduction	1
1.1	Spiral particle separators	1
1.2	Particle-free flow in curved geometries	3
1.3	Particle-laden flow	6
1.4	Scope of this study	7
1.5	Published works	8
2	The Navier-Stokes equations in helical coordinates	9
2.1	Introduction	9
2.2	Coordinate system definition and differential operators	11
2.3	The Navier-Stokes equations for particle-free flow	16
3	Particle-free flow in channels with rectangular cross-section	25
3.1	Introduction	25
3.2	Orthonormal coordinates	26
3.3	Thin film equations	28
3.4	The thin-film solution	30
3.5	Results	36
3.6	Conclusions	48
4	Particle-free flow in shallow channels with arbitrary cross-section	51
4.1	Thin-film equations	52
4.2	Solution of the thin-film equations	54
4.3	Results	58
4.4	Conclusions	74

5	Particle-laden flow in shallow channels	77
5.1	The particle-laden flow model	78
5.2	Governing equations for particle-laden flow in a helical channel . .	82
5.3	Thin-film equations	84
5.4	The thin-film solution for $\phi = \phi(y)$	87
5.5	Results	93
5.6	Conclusions	103
6	Conclusions	107
	Bibliography	111

Chapter 1

Introduction

1.1 Spiral particle separators

This project is motivated by spiral particle separators, devices used in the mining and mineral-processing industries to separate ores and clean coal. Spiral particle separators feature a spiral channel, down which a slurry of crushed rock/ore and water is run. The complex secondary motion, along with the inertia of the particles and their tendency to settle under gravity, act to sort the particles across the width of the channel according to their weight. Thus, particles of different densities can be separated from each other by splitting the flow at the bottom of the channel. A diagram of a spiral particle separator is shown in figure 1.1. To our knowledge, the earliest description of such a device is an 1899 US patent (Pardee, 1899), although particle separators did not see widespread adoption until the late 1940s and 1950s, with the Humphrey's Spiral Concentrator (Humphreys, 1943; Richards et al., 1985).

Spiral particle separators have been used for many years, and experiments have been performed (Holland-Batt, 1975, 1989, 1995b; Holland-Batt and

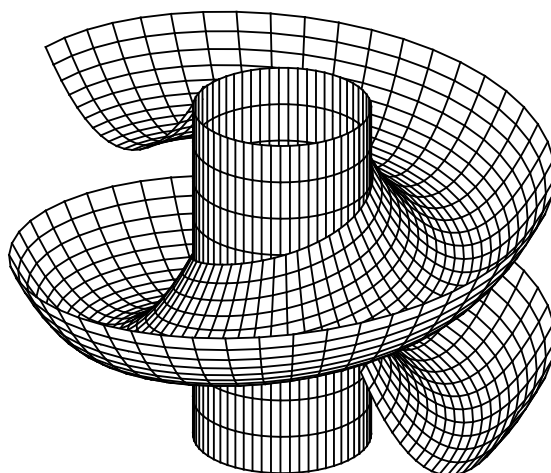


Figure 1.1: A spiral particle separator featuring (in this case) a channel with parabolic cross-section, wound around a central column.

Holtham, 1991; Holtham, 1990, 1992; Boucher et al., 2014, 2015). However, the very thin fluid depth that typifies spiral separators makes accurate results very difficult to obtain. Holtham (1992) reports errors as high as $\pm 30\%$, and Boucher et al. (2014, 2015) only track tracer particles, and do not measure the fluid depth or vertical component of the secondary flow.

The design of spiral particle separators is largely experimental, and improved mathematical models could help this process (Holland-Batt, 1995a, 2009). Spiral particle separators are sensitive to the composition of the input slurry, and small changes to the size, density, or concentration of the particles can lead to dramatically impaired separation efficiency. Often, spiral particle separators operate at a regime very close to beaching, where particles are deposited on the channel bottom at its edges, and don't flow to the outlet of the channel (Holland-Batt, 1995a). Mathematical modelling has the capability to improve prediction of flows in spiral separators, reducing the dependence on experimentation in their design. Some computational studies into particle-laden flow in helical channels using CFD have been undertaken, for example Wang and Andrews (1994); Matthews et al. (1998, 1999); Das et al. (2007), but there have been very few analytical studies. Analytic stud-

ies into particle-free flow in helical channels include Stokes (2001a); Stokes et al. (2004, 2013) . An study of particle-laden flow in helical channels that will be of particular interest in this thesis is Lee et al. (2014), which used numerical methods only to solve an ordinary differential equation.

1.2 Particle-free flow in curved geometries

Fluid flows in curved geometries have been studied for over 100 years. The motivation for these studies have included flow around river bends, in curved pipes, and blood flow in the circulatory system.

Early published work by Thomson (1876, 1877) considered the flow of water in a river bend, and in particular, the tendency for sedimentation to occur against the inner bank of the curve, even though the fluid velocity is higher there than at the outer bank. Thomson made reference to a secondary flow from the inner to outer bank at the surface of the water, and from the outer to the inner bank near the river bed. Experimental evidence for the existence of such complex secondary flows was given by Eustice (1910), who performed experiments with curved and straight pipes carrying water, and found significant differences in the pressure drop and transition to turbulence for the different geometries. Subsequently, Eustice (1911) presented streamlines observed in pipes of various shapes, showing the complex secondary flow induced by curvature.

Dean (1927, 1928) performed a mathematical analysis of the flow in a torus with large radius, allowing the flow to be considered as a perturbation to a straight pipe flow. Dean derived expressions for the fluid velocity and the streamfunction of the secondary flow, showing that the flow split into two separate vortices, one above and one below the equator of the torus. The pioneering work of Dean led to the naming of a parameter used in his derivation, a Reynolds number modified by curvature, as the Dean number.

There has been significant research into flows in curved geometries since Dean's work, and two early review articles are Berger et al. (1983) and Ito (1987). The two-vortex solution found by Dean does not persist over all values of the Dean number. Two- and four-vortex solutions were found for higher Dean numbers, and the bifurcation structure of such flows was studied by, for example, Winters (1987) and Daskopoulos and Lenhoff (1989). Blood flow in arteries has motivated several studies into curved pipes. Lynch et al. (1996) studied flow in pipes with varying curvature, and Siggers and Waters (2008) considered pulsatile flow in pipes of small constant curvature.

Dean studied flow in toroidal pipes, which feature small (but non-zero) curvature and zero torsion. An open question for some time after his work was how torsion would affect the flow. Wang (1981) and Germano (1982) extended the work of Dean by considering flow in helical pipes with small torsion and small curvature, assuming the flow was helically-symmetric, that is, that the flow is independent of position along any helix with the same pitch as the channel centreline. Their results did not agree, with Wang claiming a leading order effect of torsion on the flow, whilst Germano claimed the effect was of second order (and hence far less significant). Wang used a non-orthogonal coordinate system based on arc-length along the pipe with a 2D coordinate system in the pipe cross-section, and Germano showed that, by rotating the reference line of the cross-sectional coordinates, the coordinate system could be made orthogonal. It was this difference in the coordinate system, and the interpretation by Wang of the contra/covariant components of the flow, that led to the disagreement. Tuttle (1990) resolved the differences between the two approaches to determine that torsion did indeed have a leading order effect on the flow.

Since the work of Germano and Wang, many authors have studied flows in helical pipes. Bolinder (1995) studied the bifurcation structure of flow in helical pipes, making comparisons to previous studies in toroidal pipes. Many studies used Germano's coordinate system, however Zabielski and Mestel (1998a) showed that it did not allow for helical symmetry to be imposed,

except in the limit of small centreline torsion. Further, Zabielski and Mestel (1998a) proved that helical symmetry could only be imposed in a non-orthogonal coordinate system, and introduced a non-orthogonal coordinate system that allowed for helical symmetry to be imposed and for pipes with large curvature and torsion to be studied. They studied rectangular and circular pipes, using both analytic and numeric methods. In a later paper Zabielski and Mestel (1998b) extended their work to consider pulsatile flows to model blood flow in arteries. Germano's coordinate system is orthogonal, and hence simpler to work with than Zabielski and Mestel's, and was used by Gammack and Hydon (2001) to study pulsatile flows in circular pipes with slowly varying curvature and torsion. The orthogonal coordinate system of Germano (1982) requires the cross-sectional coordinate system to rotate along the length of the pipe, so non-circular cross-sectional shapes are difficult to model. The non-orthogonal coordinate system of Zabielski and Mestel (1998a,b) is difficult to visualise and implement, and does not allow for varying curvature and/or torsion. Manoussaki and Chadwick (2000) introduced a new non-orthogonal coordinate system that allowed the study of strongly curved pipes with non-circular cross-sections, with nonconstant torsion and curvature. They studied inviscid flow in the cochlea, modelled as a helical pipe with slowly varying curvature and rectangular cross-section.

The presence of a free-surface, the shape of which is a priori unknown, makes the problem for flow in helical channels more difficult. Helical channel flows feature in spiral particle separators, and early progress came in the form of empirical formulae based on experiments, notably from Holland-Batt and Holtham (1991). They performed experiments on spiral particle separators and tried to explain the results by forming empirical equations based on a Manning equation near the inner wall and a free-vortex in the main section of the flow. Stokes (2001a,b) studied flow in a helical channel with small centreline torsion and curvature, and with a semi-circular cross-section. Following this, efforts were made to find solutions valid under more relaxed conditions of non-small curvature and torsion, and different channel cross-sections. In particular, the thin-film assumption was used to allow significant progress

for flows in rectangular channels (Stokes et al., 2004; Lee et al., 2012; Stokes et al., 2013; Lee et al., 2014), although all of these studies required some limits on the channel centreline, be it small torsion, small curvature, or small centreline slope.

1.3 Particle-laden flow

Particle-laden flows are ubiquitous in nature and industry, and have been a topic of research for many years. Einstein (1906) developed a leading order approximation for the increase in effective viscosity of a dilute mixture of particles in a fluid. It wasn't until the 1970's that the second order term was found, by Batchelor and Green (1972) and Batchelor (1977). For dilute suspensions, the particles have a relatively minor effect on the bulk flow, but as the volume fraction of particles increases, the particles have a larger effect. In order to study more concentrated suspensions, models that allow for two-way coupling between the fluid and particle motion are required. Such models can be split into two main categories, discrete and continuum models. Discrete models track the motion of individual particles and their effect on the bulk flow, and are very computationally intensive so only dilute suspensions can be considered (Matthews et al., 1998). Continuum models treat the fluid and particles as two separate phases, treating each as a continuum, and writing coupled equations for each phase. Two important continuum models for suspension flows are the diffusive-flux model introduced by Leighton and Acrivos (1987), and the suspension-balance model of Nott and Brady (1994). The diffusive-flux model allows for study of various phenomena acting on the particle phase, such as Brownian diffusion, settling under the effect of gravity, and shear-induced migration, and can be analytically tractable in some cases (Lee et al., 2014). The suspension-balance model is based on averaging the mass, momentum, and energy balance equations, and is more general, as it actually contains the diffusive-flux model (Nott and Brady, 1994). Nott and

Brady claimed their model was valid in the case of small shear, whilst the Leighton and Acrivos model was not.

The diffusive-flux migration model has been used by Cook et al. (2008) and Murisic et al. (2011, 2013) to study particle laden thin films flowing down straight inclined planes. Murisic et al. (2011) performed experiments, and observed three distinct behaviours, depending on the angle of inclination of the channel, and the particle volume fraction. The particles can settle to the bottom of the fluid, rise to the surface, or disperse uniformly throughout the channel depth. For shallow angles, and low particle concentrations, the particles settle to the bed and the suspending liquid flows over the top of the particles, with higher speed. For steeper angles of inclination, and higher particle volume fractions, the particles group near the surface of the film, causing a ridge of particles at the front of the particle-rich region. The particles flow at a higher velocity over the top of the suspending liquid. Between the settled and ridged regimes is the well-mixed regime, where the particles disperse uniformly throughout the film thickness, and the fluid and particle velocities are similar. Lee et al. (2014) studied particle-laden flows in helical channels and found solutions in the well-mixed regime.

1.4 Scope of this study

In this work, we consider steady, helically-symmetric flows of fluids in helical channels. The steady assumption means the flow is not time-dependent, and the assumption of helical symmetry means the flow is unchanged along any helix with the same pitch as the channel centreline. Together, these assumptions mean the results obtained are valid for fully developed, but still laminar, flow. Experiments (Holtham, 1990, 1992; Holland-Batt and Holtham, 1991) have shown that flows in industrial spiral particle separators become fully-developed within 2-3 turns, and remain laminar in most of the flow domain, justifying the use of these assumptions.

In chapter 2, the choice of coordinate system is discussed, and the helical coordinate system is defined. The equations governing particle-free fluid motion are derived in this non-orthogonal coordinate system, which are then studied in chapters 3 and 4. In chapter 3, the equations are simplified using the thin-film approximation and solved analytically in the simplest case of clear-fluid flow in a rectangular channel. In this simple case, significant analytic progress is possible, and the solutions can be analysed in detail to determine the effects of changing the radius and pitch of the channel centreline. The conclusions are used to inform the study of flows in more complex geometries. Chapter 4 considers flow in channels of arbitrary but shallow cross-section. Finally, in chapter 5, the diffusive-flux model for particle-laden flow is introduced, and the governing equations for particle-laden are presented. Some results are given and discussed for the effect of channel shape and particle density. Finally, conclusions are drawn, and future research directions are identified in chapter 6.

1.5 Published works

Material from chapter 3 appears in D. J. Arnold, Y. M. Stokes, and J. E. F. Green. Thin-film flow in helically-wound rectangular channels of arbitrary torsion and curvature. *J. Fluid Mech.*, 764:76–94, 2015.

Material from chapter 4 has been submitted for publication in D. J. Arnold, Y. M. Stokes, and J. E. F. Green. Thin-film flow in helically-wound shallow channels of arbitrary cross-sectional shape. *Phys. Fluids*, submitted, 2016.

Chapter 2

The Navier-Stokes equations in helical coordinates

2.1 Introduction

Throughout this thesis, we will study helical channels such as that shown in figure 2.1. The channel centreline is a helix of radius A and pitch $2\pi P$. The channel is wound around a central axis, which is aligned with the direction of gravitational acceleration, \mathbf{g} . We consider steady, helically-symmetric flow of a viscous fluid driven by gravity. This means we assume the flow reaches an equilibrium configuration, and study the steady-state conditions. The assumption of helical symmetry means fluid properties are independent of distance along any helix with the same pitch as the channel centreline. Holland-Batt (1995b) gives evidence to suggest that these assumptions could be valid after as few as one or two turns down a channel.

We leave consideration of particle-laden flow to chapter 5 and begin by assuming a clear-fluid flow. The governing equations of the flow are the steady

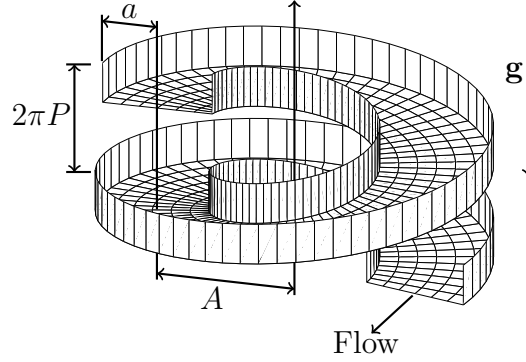


Figure 2.1: Diagram of a helical channel.

Cauchy momentum equations,

$$\rho(\mathbf{v} \cdot \nabla \mathbf{v}) = -\nabla p + \nabla \cdot (\mu \mathcal{S}) + \mathbf{F}, \quad (2.1.1)$$

where ρ is the fluid density, \mathbf{v} is the fluid velocity, p is the pressure, μ is the viscosity, \mathcal{S} is the rate-of-strain tensor, and \mathbf{F} represents any applied body forces. We will use $\mathcal{S} = \nabla \mathbf{v} + (\nabla \mathbf{v})^T$ and so have the Navier-Stokes equations. The fluid is assumed incompressible, so we also have the continuity equation,

$$\nabla \cdot \mathbf{v} = 0. \quad (2.1.2)$$

Zabieliski and Mestel (1998a) proved that helical symmetry could not be imposed in an orthogonal coordinate system, and so we have no choice but to use a non-orthogonal one. We use natural helicoidal coordinates similar to those used in Manoussaki and Chadwick (2000) for the study of perilymph in the cochlea. They modelled the cochlea as a helical pipe with rectangular cross-section and slowly decreasing radius of curvature. Their model was derived for inviscid, irrotational, incompressible flow. Lee et al. (2014) used a similar coordinate system to study particle-laden and clear-fluid flows in spiral particle separators for channels of rectangular cross-section and with small centreline slope. Here, we derive a model for a viscous, incompressible flow in a channel of arbitrary cross-section, generalising the equations from

Manoussaki and Chadwick (2000) and the clear-fluid equations from Lee et al. (2014).

To work with differential operators in a non-orthogonal coordinate system, we use the techniques of tensor calculus. For comprehensive introductions to the methods used here, see, for example, Simmonds (1994) or Eringen (1962). However, we briefly highlight some conventions that will be used herein. We employ the Einstein summation notation, where an index that appears once as a subscript and once as a superscript implies summation with respect to that index, and single indices mean the equation is valid for each choice of that index. For example,

$$g_{ij}x^i = \sum_i g_{ij}x^i \quad \text{for each } j. \quad (2.1.3)$$

We use subscript commas to indicate partial differentiation,

$$x_{,i} = \frac{\partial x}{\partial \xi^i}, \quad (2.1.4)$$

where ξ^i refers to the variable corresponding to the i -th basis vector. The Kronecker delta symbol is used frequently when manipulating tensors, and is defined as

$$\delta_j^i = \begin{cases} 1 & \text{if } i = j \\ 0 & \text{otherwise.} \end{cases} \quad (2.1.5)$$

2.2 Coordinate system definition and differential operators

Points \mathbf{p} on a helical curve of radius r and pitch $2\pi P$ are given by

$$\mathbf{p}(r, \beta) = r \cos(\beta) \hat{\mathbf{i}} + r \sin(\beta) \hat{\mathbf{j}} + P\beta \hat{\mathbf{k}}, \quad (2.2.1)$$

where β is the angle measured from a reference direction, as illustrated in figure 2.2 and $\hat{\mathbf{i}}$, $\hat{\mathbf{j}}$ and $\hat{\mathbf{k}}$ are the standard Cartesian basis vectors. Now let

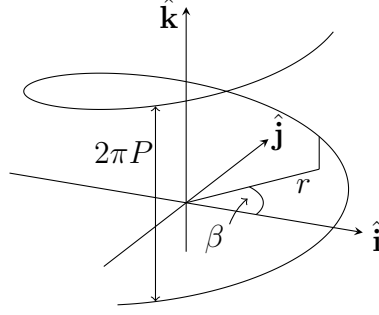


Figure 2.2: A helix with radius r and pitch $2\pi P$.

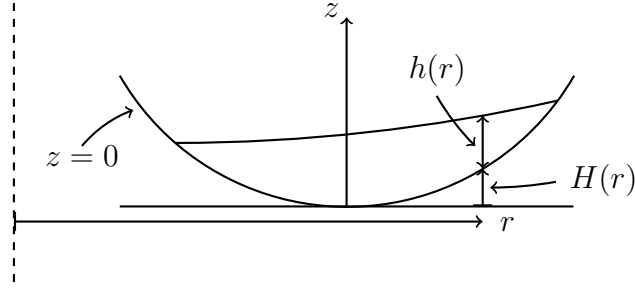


Figure 2.3: Vertically cut cross-section at some angle β of a channel with a curved bottom.

$H(r)$ define the channel cross-sectional profile, and z be the vertical distance from the channel bottom. Any point \mathbf{x} in the fluid domain can now be represented as, illustrated in figure 2.3,

$$\mathbf{x}(r, \beta, z) = r \cos(\beta) \hat{\mathbf{i}} + r \sin(\beta) \hat{\mathbf{j}} + (P\beta + H(r) + z) \hat{\mathbf{k}}. \quad (2.2.2)$$

The fluid depth at a given radial position r is denoted by $h(r)$, and the fluid domain is bounded below by the channel bottom $z = 0$, bounded above by the free surface $z = h(r)$, and bounded radially by the points where $h(r) > 0$.

We will make heavy use of the following notation. The slope of the channel at any radial position r is given as,

$$\Lambda = \frac{P}{r}, \quad (2.2.3)$$

and, for notational convenience,

$$\Upsilon = 1 + \Lambda^2, \quad (2.2.4)$$

which is related to the path length of a helix with pitch $2\pi P$ and radius r . We define the radius of the channel centreline to be A , and its slope is given by,

$$\lambda = \Lambda(A) = \frac{P}{A}. \quad (2.2.5)$$

Torsion and curvature are two very important quantities for any space curve, and indeed a helix can be defined as the only non-trivial space curve with constant torsion and curvature. When studying flow in helical geometries, many previous studies assume the curvature and torsion are constant across the fluid domain, and that one or both of curvature and torsion are negligibly small. Care must be taken, however, since torsion and curvature are not one-to-one functions, and there are different ways of having a small torsion or small curvature limit. The torsion of a helical path with pitch $2\pi P$ at radius r is given by,

$$\tau(r) = \frac{P}{r^2 + P^2}, \quad (2.2.6)$$

and the curvature is

$$\kappa(r) = \frac{r}{r^2 + P^2}. \quad (2.2.7)$$

For a small torsion limit, we can have very small pitch relative to centreline radius, $A \gg P$, or very large pitch, $P \gg 1$, with any radius of the channel centreline. The behaviour in these cases will be significantly different, so we will not use torsion and curvature as parameters in our solutions, preferring to use quantities that correspond more directly to the pitch and radius of the channel centreline. By way of example, Stokes et al. (2013) considered flow in helical channels with rectangular cross-section in the small-torsion limit, but their results are valid only in the $A \gg P$ case. We also note that small curvature can be realised by requiring very large radius, $A \gg 1$, the usual sense of small curvature, or very large pitch, $P \gg A$.

2.2.1 Basis vectors, the metric tensor and Christoffel symbols

We are now in a position to write the differential operators that appear in the governing equations (2.1.1) and (2.1.2) in their expanded component forms. The procedure to obtain these is as follows. Starting with equation (2.2.2), we find the basis vectors and metric tensor, and use them to find the Christoffel symbols of the second kind. We use these symbols to find differential operators, and then finally write out the full governing equations in our helicoidal coordinate system. The process is described in, for example, Simmonds (1994), and here we give only a summary.

The covariant basis vectors, given by $\mathbf{g}_i = \mathbf{x}_{,i}$, are

$$\mathbf{g}_r = \cos(\beta)\hat{\mathbf{i}} + \sin(\beta)\hat{\mathbf{j}} + H'(r)\hat{\mathbf{k}}, \quad (2.2.8a)$$

$$\mathbf{g}_\beta = -r \sin(\beta)\hat{\mathbf{i}} + r \cos(\beta)\hat{\mathbf{j}} + P \hat{\mathbf{k}}, \quad (2.2.8b)$$

$$\mathbf{g}_z = \hat{\mathbf{k}}, \quad (2.2.8c)$$

and are illustrated in figure 2.4. The Jacobian matrix is

$$G = [\mathbf{g}_r \ \mathbf{g}_\beta \ \mathbf{g}_z] = \begin{bmatrix} \cos(\beta) & -r \sin(\beta) & 0 \\ \sin(\beta) & r \cos(\beta) & 0 \\ H'(r) & P & 1 \end{bmatrix}. \quad (2.2.9)$$

The elements of the covariant metric tensor are given by $g_{ij} = \mathbf{g}_i \cdot \mathbf{g}_j$, which gives

$$[g_{ij}] = \begin{bmatrix} 1 + H'(r)^2 & PH'(r) & H'(r) \\ PH'(r) & r^2 + P^2 & P \\ H'(r) & P & 1 \end{bmatrix}. \quad (2.2.10)$$

The non-zero off-diagonal elements show that this coordinate system is not orthogonal.

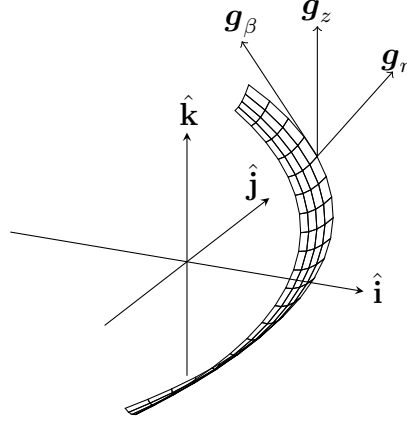


Figure 2.4: A section of a curved channel bottom with the covariant basis vectors shown at one point.

The inverse Jacobian matrix is

$$G^{-1} = \begin{bmatrix} \mathbf{g}^r \\ \mathbf{g}^\beta \\ \mathbf{g}^z \end{bmatrix} = \begin{bmatrix} \cos(\beta) & \sin(\beta) & 0 \\ -\sin(\beta)/r & \cos(\beta)/r & 0 \\ -H'(r)\cos(\beta) + \Lambda\sin(\beta) & -H(r)\sin(\beta) - \Lambda\cos(\beta) & 1 \end{bmatrix}, \quad (2.2.11)$$

so the contravariant basis vectors are

$$\mathbf{g}^r = \cos(\beta)\hat{\mathbf{i}} + \sin(\beta)\hat{\mathbf{j}}, \quad (2.2.12a)$$

$$\mathbf{g}^\beta = -\frac{\sin(\beta)}{r}\hat{\mathbf{i}} + \frac{\cos(\beta)}{r}\hat{\mathbf{j}}, \quad (2.2.12b)$$

$$\mathbf{g}^z = (-H'(r)\cos(\beta) + \Lambda\sin(\beta))\hat{\mathbf{i}} - (H'(r)\sin(\beta) + \Lambda\cos(\beta))\hat{\mathbf{j}} + \hat{\mathbf{k}}. \quad (2.2.12c)$$

We can express the contravariant basis vectors in terms of the covariant basis vectors as

$$\mathbf{g}^r = \mathbf{g}_r - H'(r)\mathbf{g}_z, \quad (2.2.13a)$$

$$\mathbf{g}^\beta = \frac{1}{r^2}\mathbf{g}_\beta - \frac{\Lambda}{r}\mathbf{g}_z, \quad (2.2.13b)$$

$$\mathbf{g}^z = -H'(r)\mathbf{g}_r - \frac{\Lambda}{r}\mathbf{g}_\beta + \Phi\mathbf{g}_z, \quad (2.2.13c)$$

which gives the contravariant metric tensor,

$$[g^{ij}] = \begin{bmatrix} 1 & 0 & -H'(r) \\ 0 & 1/r^2 & -P/r^2 \\ -H'(r) & -P/r^2 & \Phi \end{bmatrix}, \quad (2.2.14)$$

where $\Phi = \Upsilon + H'(r)^2$.

The physical components of a vector are defined as $v^{(i)} = v^i |\mathbf{g}_i|$, and are given by,

$$v^{(r)} = \sqrt{1 + H'(r)^2} v^r, \quad v^{(\beta)} = r \sqrt{\Upsilon} v^\beta, \quad v^{(z)} = v^z. \quad (2.2.15)$$

Now we calculate $\mathbf{g}_{i,j} = \mathbf{x}_{,ij}$, which will be used to find the Christoffel symbols of the second kind,

$$\begin{aligned} \mathbf{g}_{r,r} &= H''(r) \hat{\mathbf{k}}, \quad \mathbf{g}_{r,\beta} = -\sin(\beta) \hat{\mathbf{i}} + \cos(\beta) \hat{\mathbf{j}}, \quad \mathbf{g}_{r,z} = \mathbf{0}, \\ \mathbf{g}_{\beta,r} &= -\sin(\beta) \hat{\mathbf{i}} + \cos(\beta) \hat{\mathbf{j}}, \quad \mathbf{g}_{\beta,\beta} = -r \cos(\beta) \hat{\mathbf{i}} - r \sin(\beta) \hat{\mathbf{j}}, \quad \mathbf{g}_{\beta,z} = \mathbf{0}, \\ \mathbf{g}_{z,r} &= \mathbf{0}, \quad \mathbf{g}_{z,\beta} = \mathbf{0}, \quad \mathbf{g}_{z,z} = \mathbf{0}. \end{aligned} \quad (2.2.16)$$

The Christoffel symbols of the second kind are defined by $\Gamma_{ij}^k = \mathbf{g}_{i,j} \cdot \mathbf{g}^k$, and the non-zero symbols are,

$$\begin{aligned} \Gamma_{\beta\beta}^r &= -r, \quad \Gamma_{r\beta}^\beta = \Gamma_{\beta r}^\beta = \frac{1}{r}, \quad \Gamma_{rr}^z = H''(r), \\ \Gamma_{\beta\beta}^z &= rH'(r), \quad \Gamma_{r\beta}^z = \Gamma_{\beta r}^z = -\Lambda. \end{aligned} \quad (2.2.17)$$

2.3 The Navier-Stokes equations for particle-free flow

We now present particular differential operators that appear in the Navier-Stokes equations. We impose helical symmetry throughout by setting all quantities to be independent of β , so all derivatives with respect to β are set to zero.

2.3.1 The continuity equation

The continuity equation for a fluid of constant density is,

$$\nabla \cdot \mathbf{v} = 0, \quad (2.3.1)$$

and is evaluated using,

$$\nabla \cdot \mathbf{v} = v^i_{,i} + v^j \Gamma^i_{ij}, \quad (2.3.2)$$

to give,

$$\frac{\partial v^r}{\partial r} + \frac{\partial v^z}{\partial z} + \frac{v^r}{r} = 0. \quad (2.3.3)$$

2.3.2 The pressure gradient

The gradient of a scalar function, for example pressure, is given simply by $\nabla p = p_{,i} \mathbf{g}^i = p_{,i} g^{ij} \mathbf{g}_j$, which gives,

$$\nabla p = \left(\frac{\partial p}{\partial r} - H'(r) \frac{\partial p}{\partial z} \right) \mathbf{g}_r - \frac{\Lambda}{r} \frac{\partial p}{\partial z} \mathbf{g}_\beta + \left(-H'(r) \frac{\partial p}{\partial r} + \Phi \frac{\partial p}{\partial z} \right) \mathbf{g}_z. \quad (2.3.4)$$

2.3.3 The rate of strain tensor

The rate of strain tensor, \mathcal{S} , is defined by $\mathcal{S} = (\nabla \mathbf{v}) + (\nabla \mathbf{v})^T$. The velocity gradient $\nabla \mathbf{v}$ is given by,

$$\begin{aligned} \nabla \mathbf{v} &= \mathbf{g}^i \nabla_i (v^j \mathbf{g}_j) \\ &= \mathbf{g}^i \mathbf{g}_j \nabla_i v^j \\ &= \mathbf{g}^i \mathbf{g}_j (v^j_{,i} + v^k \Gamma^j_{ik}) \\ &= \mathbf{g}_i \mathbf{g}_j (g^{im} v^j_{,m} + g^{im} v^k \Gamma^j_{mk}), \end{aligned} \quad (2.3.5)$$

2. The Navier-Stokes equations in helical coordinates

so we can write \mathcal{S} as,

$$\begin{aligned}\mathcal{S} &= \mathbf{g}_i \mathbf{g}_j (g^{im} v_{,m}^j + g^{im} v^k \Gamma_{mk}^j) + \mathbf{g}_i \mathbf{g}_j (g^{jm} v_{,m}^i + g^{jm} v^k \Gamma_{mk}^i) \\ &= \mathbf{g}_i \mathbf{g}_j (g^{im} v_{,m}^j + g^{im} v^k \Gamma_{mk}^j + g^{jm} v_{,m}^i + g^{jm} v^k \Gamma_{mk}^i) \\ &= \mathcal{S}^{ij} \mathbf{g}_i \mathbf{g}_j.\end{aligned}\tag{2.3.6}$$

Evaluating the components of the rate of strain tensor, \mathcal{S}^{ij} , and using the contravariant metric tensor and Christoffel symbols given earlier, we obtain,

$$S^{rr} = 2 \frac{\partial v^r}{\partial r} - 2H'(r) \frac{\partial v^r}{\partial z}, \tag{2.3.7a}$$

$$S^{r\beta} = S^{\beta r} = \frac{\partial v^\beta}{\partial r} + \frac{1}{r^2} \frac{\partial v^r}{\partial \beta} - H'(r) \frac{\partial v^\beta}{\partial z} - \frac{P}{r^2} \frac{\partial v^r}{\partial z}, \tag{2.3.7b}$$

$$S^{rz} = S^{zr} = -H'(r) \frac{\partial v^r}{\partial r} - \frac{P}{r^2} \frac{\partial v^r}{\partial \beta} + \Phi \frac{\partial v^r}{\partial z} + \frac{\partial v^z}{\partial r} - H'(r) \frac{\partial v^z}{\partial z} + H''(r) v^r, \tag{2.3.7c}$$

$$S^{\beta\beta} = \frac{2}{r^2} \frac{\partial v^\beta}{\partial \beta} + \frac{2}{r^3} v^r - \frac{2P}{r^2} \frac{\partial v^\beta}{\partial z}, \tag{2.3.7d}$$

$$S^{\beta z} = S^{z\beta} = -H'(r) \frac{\partial v^\beta}{\partial r} - \frac{P}{r^2} \frac{\partial v^\beta}{\partial \beta} + \Phi \frac{\partial v^\beta}{\partial z} - \frac{2P}{r^3} v^r + \frac{1}{r^2} \frac{\partial v^z}{\partial \beta} - \frac{P}{r^2} \frac{\partial v^z}{\partial z}, \tag{2.3.7e}$$

$$S^{zz} = -\frac{2P}{r^2} \frac{\partial v^z}{\partial \beta} + \frac{2P^2}{r^3} v^r + 2\Phi \frac{\partial v^z}{\partial z} - 2H'(r) \frac{\partial v^z}{\partial r} - 2H''(r) H'(r) v^r. \tag{2.3.7f}$$

2.3.4 Divergence of the rate of strain tensor

The divergence of the rate of strain tensor is found using

$$\begin{aligned}\nabla \cdot \mathcal{S} &= \mathbf{g}^i \cdot \mathcal{S}_{,i} \\ &= \mathbf{g}_k \nabla_j \mathcal{S}^{jk} \\ &= \mathbf{g}_k \left(\mathcal{S}_{,j}^{jk} + \mathcal{S}^{jk} \Gamma_{ij}^i + \mathcal{S}^{ij} \Gamma_{ij}^k \right),\end{aligned}\tag{2.3.8}$$

the non-zero terms of which give,

$$\begin{aligned}\nabla \cdot \mathcal{S} = & \left(\mathcal{S}_{,r}^{rr} + \mathcal{S}_{,\beta}^{\beta r} + \mathcal{S}_{,z}^{zr} + \Gamma_{\beta r}^{\beta} \mathcal{S}^{rr} + \Gamma_{\beta\beta}^r \mathcal{S}^{\beta\beta} \right) \mathbf{g}_r \\ & + \left(\mathcal{S}_{,r}^{r\beta} + \mathcal{S}_{,\beta}^{\beta\beta} + \mathcal{S}_{,z}^{z\beta} + \Gamma_{\beta r}^{\beta} \mathcal{S}^{r\beta} + \Gamma_{r\beta}^{\beta} \mathcal{S}^{\beta r} + \Gamma_{\beta r}^{\beta} \mathcal{S}^{r\beta} \right) \mathbf{g}_{\beta} \\ & + \left(\mathcal{S}_{,r}^{rz} + \mathcal{S}_{,\beta}^{\beta z} + \mathcal{S}_{,z}^{zz} + \Gamma_{\beta r}^{\beta} \mathcal{S}^{rz} + \Gamma_{rr}^z \mathcal{S}^{rr} \right. \\ & \left. + \Gamma_{r\beta}^z \mathcal{S}^{\beta r} + \Gamma_{\beta r}^z \mathcal{S}^{r\beta} + \Gamma_{\beta\beta}^z \mathcal{S}^{\beta\beta} \right) \mathbf{g}_z.\end{aligned}\quad (2.3.9)$$

We will now impose helical symmetry, by neglecting derivatives with respect to β , and exploit the symmetry of the Christoffel symbols and the stress tensor to simplify $\nabla \cdot \mathcal{S}$ to

$$\begin{aligned}\nabla \cdot \mathcal{S} = & \left(\mathcal{S}_{,r}^{rr} + \mathcal{S}_{,z}^{zr} + \Gamma_{\beta r}^{\beta} \mathcal{S}^{rr} + \Gamma_{\beta\beta}^r \mathcal{S}^{\beta\beta} \right) \mathbf{g}_r + \left(\mathcal{S}_{,r}^{r\beta} + \mathcal{S}_{,z}^{z\beta} + 3\Gamma_{\beta r}^{\beta} \mathcal{S}^{r\beta} \right) \mathbf{g}_{\beta} \\ & + \left(\mathcal{S}_{,r}^{rz} + \mathcal{S}_{,z}^{zz} + \Gamma_{\beta r}^{\beta} \mathcal{S}^{rz} + \Gamma_{rr}^z \mathcal{S}^{rr} + 2\Gamma_{r\beta}^z \mathcal{S}^{\beta r} + \Gamma_{\beta\beta}^z \mathcal{S}^{\beta\beta} \right) \mathbf{g}_z.\end{aligned}\quad (2.3.10)$$

Substitution of known quantities gives,

$$\begin{aligned}\nabla \cdot \mathcal{S} = & \left[2\frac{\partial^2 v^r}{\partial r^2} + \frac{2}{r}\frac{\partial v^r}{\partial r} - \left\{ \frac{2}{r}H'(r) + H''(r) \right\} \frac{\partial v^r}{\partial z} - 3H'(r)\frac{\partial^2 v^r}{\partial z\partial r} \right. \\ & + \frac{\partial^2 v^z}{\partial r\partial z} + \Phi\frac{\partial^2 v^r}{\partial z^2} - H'(r)\frac{\partial^2 v^z}{\partial z^2} + \frac{2P}{r}\frac{\partial v^{\beta}}{\partial z} - \frac{2}{r^2}v^r \left. \right] \mathbf{g}_r \\ & + \left[\frac{\partial^2 v^{\beta}}{\partial r^2} - \left\{ H''(r) + \frac{3}{r}H'(r) \right\} \frac{\partial v^{\beta}}{\partial z} - 2H'(r)\frac{\partial^2 v^{\beta}}{\partial z\partial r} - \frac{P}{r^2}\frac{\partial^2 v^r}{\partial z\partial r} \right. \\ & + \frac{2P}{r^3}\frac{\partial v^r}{\partial z} - \frac{P}{r^2}\frac{\partial^2 v^z}{\partial z^2} + \Phi\frac{\partial^2 v^{\beta}}{\partial z^2} - \frac{2P}{r^3}\frac{\partial v^r}{\partial z} + \frac{3}{r}\frac{\partial v^{\beta}}{\partial r} - \frac{3P}{r^3}\frac{\partial v^r}{\partial z} \left. \right] \mathbf{g}_{\beta} \\ & + \left[\left\{ 2H''(r) - \frac{H'(r)}{r} \right\} \frac{\partial v^r}{\partial r} + \left\{ H'''(r) + \frac{H''(r)}{r} + \frac{2H'(r)}{r^2} \right\} v^r \right. \\ & - H'(r)\frac{\partial^2 v^r}{\partial r^2} + \frac{\partial^2 v^z}{\partial r^2} + \left\{ \frac{2P^2}{r^3} + \frac{\Phi}{r} - 2H''(r)H'(r) \right\} \frac{\partial v^r}{\partial z} \\ & + \Phi\frac{\partial^2 v^r}{\partial z\partial r} - \left\{ H''(r) + \frac{H'(r)}{r} \right\} \frac{\partial v^z}{\partial z} - 3H'(r)\frac{\partial^2 v^z}{\partial z\partial r} \\ & \left. + 2\Phi\frac{\partial^2 v^z}{\partial z^2} + \frac{1}{r}\frac{\partial v^z}{\partial r} - \frac{2P}{r}\frac{\partial v^{\beta}}{\partial r} \right] \mathbf{g}_z.\end{aligned}\quad (2.3.11)$$

We use the continuity equation, differentiated with respect to r and z , to remove some of the mixed derivatives from equation (2.3.11). Adding,

$$-\frac{\partial(\nabla \cdot \mathbf{v})}{\partial r} \mathbf{g}_r + \frac{P}{r^2}\frac{\partial(\nabla \cdot \mathbf{v})}{\partial z} \mathbf{g}_{\beta} + \Phi\frac{\partial(\nabla \cdot \mathbf{v})}{\partial z} \mathbf{g}_z = 0 \quad (2.3.12)$$

to equation (2.3.11) gives,

$$\begin{aligned}
 \nabla \cdot \mathcal{S} = & \left[\frac{\partial^2 v^r}{\partial r^2} + \frac{1}{r} \frac{\partial v^r}{\partial r} - \left\{ \frac{2}{r} H'(r) + 2H''(r) \right\} \frac{\partial v^r}{\partial z} - 3H'(r) \frac{\partial^2 v^r}{\partial z \partial r} \right. \\
 & + \Phi \frac{\partial^2 v^r}{\partial z^2} - H'(r) \frac{\partial^2 v^z}{\partial z^2} + \frac{2P}{r} \frac{\partial v^\beta}{\partial z} - \frac{1}{r^2} v^r \left. \right] \mathbf{g}_r \\
 & + \left[\frac{\partial^2 v^\beta}{\partial r^2} - \left\{ H''(r) + \frac{3}{r} H'(r) \right\} \frac{\partial v^\beta}{\partial z} - 2H'(r) \frac{\partial^2 v^\beta}{\partial z \partial r} \right. \\
 & + \Phi \frac{\partial^2 v^\beta}{\partial z^2} + \frac{3}{r} \frac{\partial v^\beta}{\partial r} - \frac{2P}{r^3} \frac{\partial v^r}{\partial z} \left. \right] \mathbf{g}_\beta + \left[\left\{ 2H''(r) - \frac{H'(r)}{r} \right\} \frac{\partial v^r}{\partial r} \right. \\
 & + \left\{ H'''(r) + \frac{H''(r)}{r} + \frac{2H'(r)}{r^2} \right\} v^r - H'(r) \frac{\partial^2 v^r}{\partial r^2} + \frac{\partial^2 v^z}{\partial r^2} \\
 & + \left\{ \frac{2P^2}{r^3} - 2H''(r)H'(r) \right\} \frac{\partial v^r}{\partial z} - \left\{ H''(r) + \frac{H'(r)}{r} \right\} \frac{\partial v^z}{\partial z} \\
 & \left. - 3H'(r) \frac{\partial^2 v^z}{\partial z \partial r} + \Phi \frac{\partial^2 v^z}{\partial z^2} + \frac{1}{r} \frac{\partial v^z}{\partial r} - \frac{2P}{r} \frac{\partial v^\beta}{\partial r} \right] \mathbf{g}_z. \tag{2.3.13}
 \end{aligned}$$

2.3.5 Convective acceleration

The convective acceleration term is given by $\mathbf{v} \cdot \nabla \mathbf{v}$ and is evaluated as,

$$\begin{aligned}
 \mathbf{v} \cdot \nabla \mathbf{v} &= (v^i \mathbf{g}_i) \cdot (\mathbf{g}^l \mathbf{g}_j [v_{,l}^j + v^k \Gamma_{lk}^j]) \\
 &= v^i (v_{,l}^j + v^k \Gamma_{lk}^j) \delta_i^l \mathbf{g}_j \\
 &= (v^i v_{,i}^j + v^i v^k \Gamma_{ik}^j) \mathbf{g}_j, \tag{2.3.14}
 \end{aligned}$$

giving

$$\begin{aligned}
 \mathbf{v} \cdot \nabla \mathbf{v} = & \left(v^r \frac{\partial v^r}{\partial r} + v^z \frac{\partial v^r}{\partial z} - r(v^\beta)^2 \right) \mathbf{g}_r + \left(v^r \frac{\partial v^\beta}{\partial r} + v^z \frac{\partial v^\beta}{\partial z} + \frac{2}{r} v^r v^\beta \right) \mathbf{g}_\beta \\
 & + \left(v^r \frac{\partial v^z}{\partial r} + v^z \frac{\partial v^z}{\partial z} + rH'(r)v^\beta v^\beta + H''(r)v^r v^r - 2\Lambda v^r v^\beta \right) \mathbf{g}_z. \tag{2.3.15}
 \end{aligned}$$

2.3.6 The helically-symmetric Navier-Stokes equations

We are now in a position to write out the steady, helically-symmetric Navier-Stokes equations for a particle-free fluid of constant density and viscosity. Equation (2.1.1) gives

$$\rho(\mathbf{v} \cdot \nabla \mathbf{v}) = -\nabla p + \mu \nabla \cdot \mathcal{S} + \mathbf{F}, \quad (2.3.16)$$

where \mathbf{F} is the body force. The only body force acting on the system is gravity, and hence,

$$\mathbf{F} = -\rho g \hat{\mathbf{k}} = -\rho g \mathbf{g}_z. \quad (2.3.17)$$

Then the Navier-Stokes equations are,

$$\begin{aligned} & \rho \left[v^r \frac{\partial v^r}{\partial r} + v^z \frac{\partial v^r}{\partial z} - r v^\beta v^\beta \right] \mathbf{g}_r + \rho \left[v^r \frac{\partial v^\beta}{\partial r} + v^z \frac{\partial v^\beta}{\partial z} + \frac{2}{r} v^r v^\beta \right] \mathbf{g}_\beta \\ & + \rho \left[v^r \frac{\partial v^z}{\partial r} + v^z \frac{\partial v^z}{\partial z} + r H'(r) v^\beta v^\beta + H''(r) v^r v^r - \frac{2P}{r} v^\beta v^r \right] \mathbf{g}_z \\ & = - \left(\frac{\partial p}{\partial r} - H'(r) \frac{\partial p}{\partial z} \right) \mathbf{g}_r + \frac{P}{r^2} \frac{\partial p}{\partial z} \mathbf{g}_\beta - \left(-H'(r) \frac{\partial p}{\partial r} + \Phi \frac{\partial p}{\partial z} \right) \mathbf{g}_z \\ & + \mu \left[\frac{\partial^2 v^r}{\partial r^2} + \frac{1}{r} \frac{\partial v^r}{\partial r} - \left\{ \frac{2}{r} H'(r) + 2H''(r) \right\} \frac{\partial v^r}{\partial z} - 3H'(r) \frac{\partial^2 v^r}{\partial z \partial r} + \Phi \frac{\partial^2 v^r}{\partial z^2} \right. \\ & \quad \left. - H'(r) \frac{\partial^2 v^z}{\partial z^2} + \frac{2P}{r} \frac{\partial v^\beta}{\partial z} - \frac{1}{r^2} v^r \right] \mathbf{g}_r + \mu \left[\frac{\partial^2 v^\beta}{\partial r^2} - \left\{ H''(r) + \frac{3}{r} H'(r) \right\} \frac{\partial v^\beta}{\partial z} \right. \\ & \quad \left. - 2H'(r) \frac{\partial^2 v^\beta}{\partial z \partial r} + \Phi \frac{\partial^2 v^\beta}{\partial z^2} + \frac{3}{r} \frac{\partial v^\beta}{\partial r} - \frac{2P}{r^3} \frac{\partial v^r}{\partial z} \right] \mathbf{g}_\beta \\ & + \mu \left[\left\{ 2H''(r) - \frac{H'(r)}{r} \right\} \frac{\partial v^r}{\partial r} + \left\{ H'''(r) + \frac{H''(r)}{r} + \frac{2H'(r)}{r^2} \right\} v^r \right. \\ & \quad \left. - H'(r) \frac{\partial^2 v^r}{\partial r^2} + \left\{ \frac{2P^2}{r^3} - 2H''(r)H'(r) \right\} \frac{\partial v^r}{\partial z} - \left\{ H''(r) + \frac{H'(r)}{r} \right\} \frac{\partial v^z}{\partial z} \right. \\ & \quad \left. + \frac{\partial^2 v^z}{\partial r^2} - 3H'(r) \frac{\partial^2 v^z}{\partial z \partial r} + \Phi \frac{\partial^2 v^z}{\partial z^2} + \frac{1}{r} \frac{\partial v^z}{\partial r} - \frac{2P}{r} \frac{\partial v^\beta}{\partial r} \right] \mathbf{g}_z - \rho g \mathbf{g}_z. \quad (2.3.18) \end{aligned}$$

Split into three equations, we get, in the radial direction,

$$\begin{aligned} & \rho \left[v^r \frac{\partial v^r}{\partial r} + v^z \frac{\partial v^r}{\partial z} - r v^\beta v^\beta \right] \\ &= -\frac{\partial p}{\partial r} + H'(r) \frac{\partial p}{\partial z} + \mu \left[\frac{\partial^2 v^r}{\partial r^2} + \frac{1}{r} \frac{\partial v^r}{\partial r} - \left\{ \frac{2}{r} H'(r) + 2H''(r) \right\} \frac{\partial v^r}{\partial z} \right. \\ & \quad \left. - 3H'(r) \frac{\partial^2 v^r}{\partial z \partial r} + \Phi \frac{\partial^2 v^r}{\partial z^2} - H'(r) \frac{\partial^2 v^z}{\partial z^2} + \frac{2P}{r} \frac{\partial v^\beta}{\partial z} - \frac{1}{r^2} v^r \right], \end{aligned} \quad (2.3.19a)$$

in the axial direction,

$$\begin{aligned} & \rho \left[v^r \frac{\partial v^\beta}{\partial r} + v^z \frac{\partial v^\beta}{\partial z} + \frac{2}{r} v^r v^\beta \right] \\ &= \frac{P}{r^2} \frac{\partial p}{\partial z} + \mu \left[\frac{\partial^2 v^\beta}{\partial r^2} - \left\{ H''(r) + \frac{3}{r} H'(r) \right\} \frac{\partial v^\beta}{\partial z} \right. \\ & \quad \left. - 2H'(r) \frac{\partial^2 v^\beta}{\partial z \partial r} + \Phi \frac{\partial^2 v^\beta}{\partial z^2} + \frac{3}{r} \frac{\partial v^\beta}{\partial r} - \frac{2P}{r^3} \frac{\partial v^r}{\partial z} \right], \end{aligned} \quad (2.3.19b)$$

and in the vertical direction,

$$\begin{aligned} & \rho \left[v^r \frac{\partial v^z}{\partial r} + v^z \frac{\partial v^z}{\partial z} + r H'(r) v^\beta v^\beta + H''(r) v^r v^r - \frac{2P}{r} v^\beta v^r \right] \\ &= H'(r) \frac{\partial p}{\partial r} - \Phi \frac{\partial p}{\partial z} + \mu \left[\left\{ 2H''(r) - \frac{H'(r)}{r} \right\} \frac{\partial v^r}{\partial r} \right. \\ & \quad - H'(r) \frac{\partial^2 v^r}{\partial r^2} + \left\{ H'''(r) + \frac{H''(r)}{r} + \frac{2H'(r)}{r^2} \right\} v^r + \frac{\partial^2 v^z}{\partial r^2} \\ & \quad + \left\{ \frac{2P^2}{r^3} - 2H''(r)H'(r) \right\} \frac{\partial v^r}{\partial z} - \left\{ H''(r) + \frac{H'(r)}{r} \right\} \frac{\partial v^z}{\partial z} \\ & \quad \left. - 3H'(r) \frac{\partial^2 v^z}{\partial z \partial r} + \Phi \frac{\partial^2 v^z}{\partial z^2} + \frac{1}{r} \frac{\partial v^z}{\partial r} - \frac{2P}{r} \frac{\partial v^\beta}{\partial r} \right] - \rho g. \end{aligned} \quad (2.3.19c)$$

2.3.7 Boundary conditions

The boundary conditions are no slip on the channel boundaries ($v^r = v^\beta = v^z = 0$ at $z = 0$), no stress at the free surface, and the kinematic condition

at the free surface. At the free surface, the no stress condition is, neglecting surface tension,

$$(\mu \mathcal{S}^{ij} - p g^{ij}) n_i = 0, \quad \text{for each } j \in \{1, 2, 3\}, \quad (2.3.20)$$

where n_i is the i -th component of the normal to the free surface. The free surface can be written as the solution to $F(r, z) = 0$, and then $\mathbf{n} = \nabla F = (F_{,r}, 0, F_{,z})$. Substituting \mathcal{S}^{ij} and g^{ij} in equation (2.3.20) gives,

$$\begin{aligned} 0 = & F_{,r} \left(2\mu \frac{\partial v^r}{\partial r} - 2\mu H'(r) \frac{\partial v^r}{\partial z} - p \right) \\ & + F_{,z} \left(\mu \left[-H'(r) \frac{\partial v^r}{\partial r} + \frac{\partial v^z}{\partial r} + \Phi \frac{\partial v^r}{\partial z} - H'(r) \frac{\partial v^z}{\partial z} + H''(r) v^r \right] + H'(r) p \right), \end{aligned} \quad (2.3.21a)$$

$$\begin{aligned} 0 = & \mu F_{,r} \left(\frac{\partial v^\beta}{\partial r} - H'(r) \frac{\partial v^\beta}{\partial z} - \frac{\Lambda}{r} \frac{\partial v^r}{\partial z} \right) \\ & + F_{,z} \left(\mu \left[-H'(r) \frac{\partial v^\beta}{\partial z} + \Phi \frac{\partial v^\beta}{\partial z} - \frac{2\Lambda}{r^2} v^r - \frac{\Lambda}{r} \frac{\partial v^z}{\partial z} \right] + \frac{\Lambda}{r} p \right), \end{aligned} \quad (2.3.21b)$$

$$\begin{aligned} 0 = & F_{,r} \left(\mu \left[-H'(r) \frac{\partial v^r}{\partial r} + \frac{\partial v^z}{\partial r} + \Phi \frac{\partial v^r}{\partial z} - H'(r) \frac{\partial v^z}{\partial z} + H''(r) v^r \right] + H'(r) p \right) \\ & + F_{,z} \left(\mu \left[\frac{2\Lambda^2}{r} v^r + 2\Phi \frac{\partial v^z}{\partial z} - 2H'(r) \frac{\partial v^z}{\partial r} - 2H''(r) H'(r) v^r \right] - \Phi p \right). \end{aligned} \quad (2.3.21c)$$

The kinematic condition is $\mathbf{v} \cdot \mathbf{n} = 0$ at the free surface $F(r, z) = 0$, and gives

$$v^r F_{,r} + v^z F_{,z} = 0. \quad (2.3.22)$$

2.3.8 Discussion

We have derived the Navier-Stokes equations in a non-orthogonal coordinate system that naturally describes the geometry of a helical channel with arbitrary cross-section. This extends the equations given in Lee et al. (2014),

which were derived for channels with rectangular cross-section, $H(r) = 0$. Their equations were derived for fluids with variable density and viscosity, whilst we here considered these quantities to be constant. In chapter 5 we will extend our model to account for variable density and viscosity, as in Lee et al. (2014).

Chapters 3 and 4 are concerned with the solution of the system of equations (2.3.3), (2.3.19), (2.3.21) and (2.3.22). In chapter 3, we consider rectangular channels for which $H(r) = 0$, where, after taking the thin-film limit, significant analytic progress is possible. In chapter 4, we study channels with non-rectangular cross-section, using rectangular channels as a baseline case. In chapter 5, we introduce a particle model, which requires some extension to the model presented here.

Chapter 3

Particle-free flow in channels with rectangular cross-section

3.1 Introduction

Having derived the Navier-Stokes equations in chapter 2 for the general case of channels with arbitrary curvature, torsion, and cross-sectional shape, we now consider channels with rectangular cross-section. Such channels are the simplest type of helical channel, and significant analytic progress is possible. Although our motivation for this study is spiral particle separators which feature non-rectangular cross-section and particle-laden flows, understanding the simpler case will help inform the study of more complex flows.

Stokes et al. (2013) found analytic solutions for flow in rectangular channels under the assumption of small centreline curvature and torsion, and Lee et al. (2014) found an analytic solution for clear-fluid flow in channels with small centreline slope. In this chapter, we find an analytic solution for flow

in rectangular channels of arbitrary curvature and torsion, generalising the results from these previous studies.

3.2 Orthonormal coordinates

To facilitate comparison with Lee et al. (2014), we move to an orthonormal coordinate system, by normalising the basis vectors and replacing the vertical coordinate direction \mathbf{g}_z with a normal direction, \mathbf{e}_n , perpendicular to the radial, \mathbf{e}_r , and axial, \mathbf{e}_β , coordinate directions. The new direction \mathbf{e}_n is, therefore, normal to the channel bottom. Here we use \mathbf{e}_i to represent the unit-length basis vector in the direction of \mathbf{g}_i . We find \mathbf{e}_n as,

$$\mathbf{e}_n = \mathbf{e}_r \times \mathbf{e}_\beta = \frac{1}{r\sqrt{\Upsilon}} \left(P \sin \beta \hat{\mathbf{i}} - P \cos \beta \hat{\mathbf{j}} + r \hat{\mathbf{k}} \right). \quad (3.2.1)$$

We write \mathbf{e}_z in terms of \mathbf{e}_β and \mathbf{e}_n as,

$$\mathbf{e}_z = \frac{1}{\sqrt{\Upsilon}} \mathbf{e}_n + \frac{\Lambda}{\sqrt{\Upsilon}} \mathbf{e}_\beta, \quad (3.2.2)$$

and so rewrite the physical velocity components (given in equation (2.2.15)), $v^{(i)}$, from the r, β, z coordinates in terms of the new r, β, n coordinates, using u^i to represent the i -th component of velocity in the new coordinates (noting $u^i = u^{(i)}$ as the basis vectors have unit length) using,

$$\begin{aligned} \mathbf{v} &= v^{(i)} \mathbf{e}_i = v^{(r)} \mathbf{e}_r + v^{(\beta)} \mathbf{e}_\beta + v^{(z)} \mathbf{e}_z \\ &= v^{(r)} \hat{\mathbf{e}}_r + v^{(\beta)} \hat{\mathbf{e}}_\beta + v^{(z)} \left(\frac{1}{\sqrt{\Upsilon}} \hat{\mathbf{e}}_n + \frac{\Lambda}{\sqrt{\Upsilon}} \hat{\mathbf{e}}_\beta \right) \\ &= v^{(r)} \hat{\mathbf{e}}_r + \left(v^{(\beta)} + \frac{\Lambda}{\sqrt{\Upsilon}} v^{(z)} \right) \hat{\mathbf{e}}_\beta + \frac{1}{\sqrt{\Upsilon}} v^{(z)} \hat{\mathbf{e}}_n \\ &= u^r \hat{\mathbf{e}}_r + u^\beta \hat{\mathbf{e}}_\beta + u^n \hat{\mathbf{e}}_n = u^i \hat{\mathbf{e}}_i, \end{aligned} \quad (3.2.3)$$

where,

$$u^r = v^r, \quad u^\beta = r\sqrt{\Upsilon}v^\beta + \frac{\Lambda}{\sqrt{\Upsilon}}v^z, \quad u^n = \frac{1}{\sqrt{\Upsilon}}v^z, \quad (3.2.4)$$

or,

$$v^r = u^r, \quad v^\beta = \frac{1}{r\sqrt{\Upsilon}}u^\beta - \frac{\Lambda}{r\sqrt{\Upsilon}}u^n, \quad v^z = \sqrt{\Upsilon}u^n. \quad (3.2.5)$$

We must also rewrite vector equations of the form $f^i \mathbf{g}_i = \mathbf{0}$ (such as the Navier-Stokes equations) in terms of the new coordinate directions,

$$\begin{aligned} f^i \mathbf{g}_i &= f^r \mathbf{g}_r + f^\beta \mathbf{g}_\beta + f^z \mathbf{g}_z \\ &= f^r \hat{\mathbf{e}}_r + r\sqrt{\Upsilon} \left(f^\beta + \frac{\Lambda}{r\Upsilon} f^z \right) \hat{\mathbf{e}}_\beta + \frac{1}{\sqrt{\Upsilon}} f^z \hat{\mathbf{e}}_n. \end{aligned} \quad (3.2.6)$$

The variables z and n are related by $z = \sqrt{\Upsilon}n$, so that

$$\frac{\partial}{\partial z} = \frac{1}{\sqrt{\Upsilon}} \frac{\partial}{\partial n}. \quad (3.2.7)$$

Using this transformation, the continuity equation (2.3.3) becomes,

$$\frac{\partial u^r}{\partial r} + \frac{\partial u^n}{\partial n} + \frac{u^r}{r} = 0. \quad (3.2.8)$$

The Navier-Stokes equations transform to give, in the radial direction,

$$\begin{aligned} &\rho \left(u^r \frac{\partial u^r}{\partial r} + u^n \frac{\partial u^r}{\partial n} - \frac{1}{r\Upsilon} [u^\beta - \Lambda u^n]^2 \right) \\ &= -\frac{\partial p}{\partial r} + \mu \left(\frac{\partial}{\partial r} \left[\frac{1}{r} \frac{\partial}{\partial r} [r u^r] \right] + \frac{\partial^2 u^r}{\partial n^2} + \frac{2\Lambda}{r\Upsilon} \frac{\partial}{\partial n} (u^\beta - \Lambda u^n) \right), \end{aligned} \quad (3.2.9a)$$

in the axial direction,

$$\begin{aligned} &\rho \left(r\sqrt{\Upsilon} u^r \frac{\partial}{\partial r} \left[\frac{1}{r\sqrt{\Upsilon}} u^\beta - \frac{\Lambda}{r\sqrt{\Upsilon}} u^n \right] + u^n \frac{\partial u^\beta}{\partial n} \right. \\ &\quad \left. + \frac{2}{r\Upsilon} u^r [u^\beta - \Lambda u^n] + \frac{\Lambda}{\sqrt{\Upsilon}} u^r \frac{\partial}{\partial r} [\sqrt{\Upsilon} u^n] \right) \\ &= \mu \left(r\sqrt{\Upsilon} \frac{\partial^2}{\partial r^2} \left[\frac{1}{r\sqrt{\Upsilon}} u^\beta - \frac{\Lambda}{r\sqrt{\Upsilon}} u^n \right] + \frac{\partial^2 u^\beta}{\partial n^2} \right. \\ &\quad \left. - \frac{2\Lambda}{r\Upsilon} \frac{\partial u^r}{\partial n} + \frac{\Lambda}{r\sqrt{\Upsilon}} \frac{\partial}{\partial r} [\sqrt{\Upsilon} u^n] + \frac{\Lambda}{\sqrt{\Upsilon}} \frac{\partial^2}{\partial r^2} [\sqrt{\Upsilon} u^n] \right. \\ &\quad \left. + \frac{2 + \Upsilon}{\sqrt{\Upsilon}} \frac{\partial}{\partial r} \left[\frac{1}{r\sqrt{\Upsilon}} u^\beta - \frac{\Lambda}{r\sqrt{\Upsilon}} u^n \right] \right) - \rho g \frac{\Lambda}{\sqrt{\Upsilon}}, \end{aligned} \quad (3.2.9b)$$

and, in the normal direction,

$$\begin{aligned} & \rho \left(\frac{1}{\sqrt{\Upsilon}} u^r \frac{\partial}{\partial r} [\sqrt{\Upsilon} u^n] + u^n \frac{\partial u^n}{\partial n} - \frac{2\Lambda}{r\Upsilon} u^r [u^\beta - \Lambda u^n] \right) \\ &= -\frac{\partial p}{\partial n} + \mu \left(\frac{1}{\sqrt{\Upsilon}} \frac{\partial^2}{\partial r^2} [\sqrt{\Upsilon} u^n] - \frac{\partial}{\partial r} \frac{2\Lambda}{\sqrt{\Upsilon}} \left[\frac{1}{r\sqrt{\Upsilon}} u^\beta - \frac{\Lambda}{r\sqrt{\Upsilon}} u^n \right] \right. \\ & \quad \left. + \frac{\partial^2 u^n}{\partial n^2} + \frac{1}{r\sqrt{\Upsilon}} \frac{\partial}{\partial r} [\sqrt{\Upsilon} u^n] + \frac{2\Lambda^2}{r\Upsilon} \frac{\partial u^r}{\partial n} \right) - \rho g \frac{1}{\sqrt{\Upsilon}}. \end{aligned} \quad (3.2.9c)$$

The no-stress boundary condition becomes, in the radial component,

$$0 = \frac{\partial F}{\partial r} \left(2\mu \frac{\partial u^r}{\partial r} - p \right) + \mu \frac{\partial F}{\partial n} \left(\frac{\partial}{\partial r} [\sqrt{\Upsilon} u^n] + \frac{\partial u^r}{\partial n} \right), \quad (3.2.10a)$$

the axial component,

$$\begin{aligned} 0 = & \mu \frac{\partial F}{\partial r} \left(\frac{\partial}{\partial r} \left[\frac{1}{r\sqrt{\Upsilon}} u^\beta - \frac{\Lambda}{r\sqrt{\Upsilon}} u^n \right] - \frac{\Lambda}{r\sqrt{\Upsilon}} \frac{\partial u^r}{\partial n} \right) \\ & + \frac{\partial F}{\partial z} \left(\mu \left[-\frac{2\Lambda}{r^2\sqrt{\Upsilon}} u^r - \frac{\Lambda}{r\sqrt{\Upsilon}} \frac{\partial u^n}{\partial n} \right. \right. \\ & \quad \left. \left. + \frac{\partial}{\partial n} \left\{ \frac{1}{r\sqrt{\Upsilon}} u^\beta - \frac{\Lambda}{r\sqrt{\Upsilon}} u^n \right\} \right] + \frac{\Lambda}{r\sqrt{\Upsilon}} p \right), \end{aligned} \quad (3.2.10b)$$

and the normal component,

$$0 = \mu \frac{\partial F}{\partial r} \left(\frac{\partial}{\partial r} [\sqrt{\Upsilon} u^n] + \sqrt{\Upsilon} \frac{\partial u^r}{\partial n} \right) \quad (3.2.10c)$$

$$+ \frac{\partial F}{\partial n} \left(\mu \left[\frac{2\Lambda^2}{r\sqrt{\Upsilon}} u^r + 2\sqrt{\Upsilon} \frac{\partial u^n}{\partial n} \right] - \sqrt{\Upsilon} p \right). \quad (3.2.10d)$$

3.3 Thin film equations

A feature of flows in spiral separators, discussed in chapter 1, is that the fluid depth in the normal direction is very small relative to the width of the channel. For example, in experiments performed using commercial particle separators, (Holtham, 1992), the fluid depth was 1–12mm in a 280mm wide channel. We now nondimensionalise and scale the equations derived previously, using $\delta \ll 1$ as a typical measure of the aspect ratio of the fluid domain.

This simplifies the model considerably. Using carets to denote dimensionless variables, the relationships between the dimensional and nondimensional scaled variables are,

$$(\hat{r}, \hat{n}) = \left(\frac{r}{a}, \frac{n}{a\delta} \right), \quad (\hat{v}, \hat{u}, \hat{w}) = \left(\frac{u^r}{U\delta}, \frac{u^\beta}{U}, \frac{u^n}{U\delta^2} \right), \quad \hat{p} = \frac{a\delta}{U\mu_f} p, \quad (3.3.1a)$$

where μ_f is the fluid viscosity and a is the channel half-width. Explicit scales for the velocity scale U and film-thickness parameter δ will be given later. We also define a new variable

$$\hat{y} = \frac{r - A}{a}, \quad (3.3.1b)$$

a modified radial variable, which measures distance from the channel centreline, rather than from the vertical axis. The dimensional radius of the channel centreline is A , which is scaled with the channel half-width a to give the nondimensional radius as $\hat{A} = A/a$, so that $-1 \leq \hat{y} \leq 1$. The nondimensional pitch of the channel centreline \hat{P} is similarly given by $\hat{P} = P/a$. We also define a modified curvature parameter, $\epsilon = a/A = 1/\hat{A}$, which represents the curvature of the circle formed by the projection of channel centreline onto a horizontal plane. Using ϵ , we write $\hat{r} = (1 + \epsilon\hat{y})/\epsilon$. We also recall the definition of the slope of the channel centreline, $\lambda = P/A = \hat{P}/\hat{A}$. The Reynolds and Froude numbers are defined as,

$$\text{Re} = \frac{\rho U a \delta}{\mu_f}, \quad \text{Fr} = \frac{U}{\sqrt{g a \delta}}, \quad (3.3.2)$$

where the thin-film parameter has been included in the length scale $a\delta$.

At leading order in δ , and dropping the carets as all variables are non-dimensional, the Navier-Stokes equations are,

$$-\frac{\partial p}{\partial y} + \frac{\text{Re} \epsilon}{(1 + \epsilon y) \Upsilon} u^2 + \frac{\partial^2 v}{\partial n^2} + 2 \frac{\epsilon \Lambda}{(1 + \epsilon y) \Upsilon} \frac{\partial u}{\partial n} = 0, \quad (3.3.3a)$$

$$\frac{\partial^2 u}{\partial n^2} - \frac{\text{Re}}{\text{Fr}^2} \frac{\Lambda}{\sqrt{\Upsilon}} = 0, \quad (3.3.3b)$$

$$\frac{\partial p}{\partial n} + \frac{\text{Re}}{\text{Fr}^2} \frac{1}{\sqrt{\Upsilon}} = 0, \quad (3.3.3c)$$

3. Particle-free flow in channels with rectangular cross-section

the continuity equation is,

$$\frac{\partial v}{\partial y} + \frac{\epsilon v}{1 + \epsilon y} + \frac{\partial w}{\partial n} = 0, \quad (3.3.3d)$$

and the boundary conditions are,

$$u = v = w = 0 \quad \text{at the channel bottom } n = 0, \quad (3.3.3e)$$

and

$$p = 0, \quad \frac{\partial v}{\partial n} = 0, \quad \frac{\partial u}{\partial n} = 0, \quad w = \frac{dh}{dy}v, \quad \text{at the free surface } n = h(y). \quad (3.3.3f)$$

3.4 The thin-film solution

We now have a system of equations (3.3.3) that can be solved analytically, by sequentially integrating and applying the boundary conditions. We begin by integrating for the pressure, p , and primary down-stream (or axial) velocity, to obtain

$$p = -\frac{\text{Re}}{\text{Fr}^2} \frac{1}{\sqrt{\Upsilon}} (n - h), \quad (3.4.1)$$

and

$$u = \frac{\text{Re}}{\text{Fr}^2} \frac{\Lambda}{\sqrt{\Upsilon}} \frac{n}{2} (n - 2h), \quad (3.4.2)$$

which is substituted into equation (3.3.3a) to give

$$\begin{aligned} \frac{\partial^2 v}{\partial n^2} &= -\frac{\text{Re}}{\text{Fr}^2} \frac{\partial}{\partial y} \left(\frac{1}{\sqrt{\Upsilon}} [n - h] \right) - \frac{\text{Re} \epsilon}{(1 + \epsilon y) \Upsilon} \left(\frac{\text{Re}}{\text{Fr}^2} \frac{\Lambda}{\sqrt{\Upsilon}} \frac{n}{2} [n - 2h] \right)^2 \\ &\quad - 2 \frac{\epsilon \Lambda}{(1 + \epsilon y) \Upsilon} \frac{\partial}{\partial n} \left(\frac{\text{Re}}{\text{Fr}^2} \frac{\Lambda}{\sqrt{\Upsilon}} \frac{n}{2} [n - 2h] \right) \\ &= -3 \frac{\text{Re}}{\text{Fr}^2} \frac{\Lambda^2 \epsilon (n - h)}{\Upsilon^{3/2} (1 + \epsilon y)} + \frac{\text{Re}}{\text{Fr}^2} \frac{1}{\sqrt{\Upsilon}} \frac{dh}{dy} - \frac{\text{Re}^3 \epsilon \Lambda^2 n^2 (n - 2h)^2}{4 \text{Fr}^4 (1 + \epsilon y) \Upsilon^2}. \end{aligned} \quad (3.4.3)$$

Integrating and applying boundary conditions gives the radial velocity component,

$$v = -3 \frac{\text{Re}}{\text{Fr}^2} \frac{\Lambda^2 \epsilon}{\Upsilon^{3/2}(1 + \epsilon y)} \frac{(n - h)^3 + h^3}{6} + \frac{\text{Re}}{\text{Fr}^2} \frac{1}{\sqrt{\Upsilon}} \frac{dh}{dy} \frac{n}{2} (n - 2h) - \frac{\text{Re}^3 \epsilon \Lambda^2}{\text{Fr}^4 (1 + \epsilon y) \Upsilon^2} \frac{n(n - 2h)(n^4 - 4hn^3 + 2h^2n^2 + 4h^3n + 8h^4)}{120}. \quad (3.4.4)$$

The continuity equation (3.3.3d) can be integrated with respect to n , from the channel bottom to the free surface, at an arbitrary radial position y , to give

$$\begin{aligned} 0 &= \int_0^{h(y)} \frac{\partial}{\partial y} ([1 + \epsilon y]v) + (1 + \epsilon y) \frac{\partial w}{\partial n} dn \\ &= \int_0^{h(y)} \frac{\partial}{\partial y} ([1 + \epsilon y]v) dn + \int_0^{h(y)} (1 + \epsilon y) \frac{\partial w}{\partial n} dn. \end{aligned} \quad (3.4.5)$$

We rearrange this equation to give

$$\int_0^{h(y)} \frac{\partial}{\partial y} (1 + \epsilon y) v dn = - (1 + \epsilon y) \left(w|_{n=h(y)} - w|_{n=0} \right). \quad (3.4.6)$$

We use the no penetration condition on the channel bottom to substitute for w on the right hand side of equation (3.4.6), then use Leibniz's rule to interchange the order of differentiation and integration on the left-hand side, to give,

$$\frac{\partial}{\partial y} \int_0^{h(y)} (1 + \epsilon y) v dn - (1 + \epsilon y) v \frac{\partial h}{\partial y} \Big|_{n=h(y)} = - (1 + \epsilon y) w|_{n=h(y)} \quad (3.4.7)$$

or,

$$\frac{\partial}{\partial y} \int_0^{h(y)} (1 + \epsilon y) v dn = - (1 + \epsilon y) \left(w - v \frac{\partial h}{\partial y} \right) \Big|_{n=h(y)}. \quad (3.4.8)$$

The kinematic boundary condition implies the right hand side is zero. Integrating with respect to y yields,

$$(1 + \epsilon y) \int_0^{h(y)} v dn = C(n), \quad (3.4.9)$$

3. Particle-free flow in channels with rectangular cross-section

and since the left-hand side is a function of y , $C(n)$ must be constant. The constant C effectively sets the net radial flow at a radial position y . We therefore set $C = 0$ which means there is no net flow in to or out of the channel, and obtain the integrated continuity equation,

$$\int_0^{h(y)} v \, dn = 0. \quad (3.4.10)$$

Substituting v into the integrated continuity equation, gives,

$$\begin{aligned} 0 = \int_0^{h(y)} & -3 \frac{\text{Re}}{\text{Fr}^2} \frac{\Lambda^2 \epsilon}{\Upsilon^{3/2}(1 + \epsilon y)} \frac{(n - h)^3 + h^3}{6} + \frac{\text{Re}}{\text{Fr}^2} \frac{1}{\sqrt{\Upsilon}} \frac{dh}{dy} \frac{n}{2} (n - 2h) \\ & - \frac{\text{Re}^3 \epsilon \Lambda^2}{\text{Fr}^4(1 + \epsilon y) \Upsilon^2} \frac{n}{120} (n^5 - 6hn^4 + 10h^2n^3 - 16h^5) \, dn \end{aligned} \quad (3.4.11)$$

and after integrating,

$$0 = -3 \frac{\text{Re}}{\text{Fr}^2} \frac{\Lambda^2 \epsilon}{\Upsilon^{3/2}(1 + \epsilon y)} \frac{h^4}{8} - \frac{\text{Re}}{\text{Fr}^2} \frac{1}{\sqrt{\Upsilon}} \frac{dh}{dy} \frac{h^3}{3} + \frac{\text{Re}^3 \epsilon \Lambda^2}{\text{Fr}^4(1 + \epsilon y) \Upsilon^2} \frac{48h^7}{840} \quad (3.4.12)$$

which is rearranged to give a differential equation for the free-surface profile $h(y)$,

$$\frac{dh}{dy} = \frac{6}{35} \frac{\text{Re}^2}{\text{Fr}^2} \frac{\epsilon \Lambda^2}{(1 + \epsilon y) \Upsilon^{3/2}} h^4 - \frac{9}{8} \frac{\Lambda^2 \epsilon}{\Upsilon(1 + \epsilon y)} h. \quad (3.4.13)$$

This equation is a Bernoulli differential equation, which has an analytical solution. We introduce $\xi = h^{-3}$, so $\xi' = -3h^{-4}h'$ (where primes denote differentiation with respect to y), which transforms the free-surface equation to a first-order linear ordinary differential equation,

$$\frac{d\xi}{dy} - \frac{27}{8} \frac{\Lambda^2 \epsilon}{\Upsilon(1 + \epsilon y)} \xi + \frac{6}{35} \frac{\text{Re}^2}{\text{Fr}^2} \frac{\epsilon \Lambda^2}{(1 + \epsilon y) \Upsilon^{3/2}} = 0. \quad (3.4.14)$$

This equation is readily solved using the integrating factor,

$$I(y) = \exp \left(\int -\frac{27}{8} \frac{\Lambda^2 \epsilon}{\Upsilon(1 + \epsilon y)} dy \right) = \Upsilon^{27/16}. \quad (3.4.15)$$

Solving equation (3.4.14) and substituting for $h(y)$, we find,

$$h(y) = \left(-\frac{18}{35} \frac{\text{Re}^2}{\text{Fr}^2} \Upsilon^{-27/16} \left[-\frac{8}{19} \Upsilon^{19/16} + B \right] \right)^{-1/3} \quad (3.4.16)$$

where B may be determined by specifying the fluid depth at a position $y = y_a$ in the channel, i.e. let $h(y_a) = h_a$ for some $-1 \leq y_a \leq 1$, to give

$$h(y) = \Upsilon(y)^{9/16} \left(\frac{144}{665} \frac{\text{Re}^2}{\text{Fr}^2} [\Upsilon(y)^{19/16} - \Upsilon(y_a)^{19/16}] + \Upsilon(y_a)^{27/16} h_a^{-3} \right)^{-1/3}. \quad (3.4.17)$$

This equation describes the shape of the free surface. The choices of y_a and h_a will be discussed later.

The continuity equation (3.3.3d) admits a streamfunction, ψ , to describe the secondary flow. The streamfunction is defined by

$$\frac{\partial \psi}{\partial y} = -(1 + \epsilon y)w \quad \text{and} \quad \frac{\partial \psi}{\partial n} = (1 + \epsilon y)v. \quad (3.4.18)$$

Using equation (3.4.4) for v , we can find the streamfunction and therefore the normal velocity, w . Choosing $\psi = 0$ on the channel bottom, the streamfunction is given by,

$$\begin{aligned} \psi = & -\frac{\text{Re}}{\text{Fr}^2} \frac{\Lambda^2 \epsilon}{\Upsilon^{3/2}} \frac{n^2 (n - h) (2n - 3h)}{16} \\ & - \frac{\text{Re}^3 \epsilon \Lambda^2}{\text{Fr}^4} \frac{n^2 (n - h) (n - 2h)^2 (n^2 - 2hn - 4h^2)}{840}. \end{aligned} \quad (3.4.19)$$

By taking the derivative of ψ with respect to y , we can calculate the normal direction velocity w . Usually, however, we will plot level curves of $\psi(n, y)$, which give the streamlines of the secondary flow.

The dimensional flux down the channel, denoted Q , is given by

$$Q = -Ua^2 \delta \int_{-1}^1 \int_0^h u \, dn \, dy = Ua^2 \delta \hat{Q}, \quad (3.4.20)$$

where \hat{Q} is the dimensionless flux. On substituting for u and integrating, we find \hat{Q} as,

$$\hat{Q} = \frac{1}{3} \frac{\text{Re}}{\text{Fr}^2} \int_{-1}^1 \frac{\Lambda h^3}{\sqrt{\Upsilon}} \, dy. \quad (3.4.21)$$

Note that the minus sign appears in (3.4.20) because our axial coordinate direction, \mathbf{e}_β , points upstream along the channel, and hence fluid flowing

3. Particle-free flow in channels with rectangular cross-section

down the channel has negative axial velocity. The integral (3.4.21) cannot be computed exactly, and so a numerical method must be used. We use the `quadgk` function provided by MATLAB.

The dimensional cross-sectional area of the fluid domain is denoted Ω , and is defined as

$$\Omega = a^2 \delta \int_{-1}^1 h \, dy = a^2 \delta \hat{\Omega} \quad (3.4.22)$$

where $\hat{\Omega}$ is the dimensionless cross-sectional area

$$\hat{\Omega} = \int_{-1}^1 h \, dy. \quad (3.4.23)$$

As with (3.4.21), we cannot evaluate this integral exactly, and must use numerical integration.

When we obtained the free surface profile (3.4.17), we imposed a boundary condition in terms of the fluid depth at some radial position in the channel. In practice however, this is not a practical parameter to control. A more natural quantity to specify is the fluid flux down the channel. Given a prescribed dimensionless flux, \hat{Q} , we need to determine the corresponding value of h_a which sets the fluid depth at a radial position y_a . Since we cannot solve for the flux exactly, we use a numerical method to find the appropriate value of h_a , using numerical quadrature to approximate the flux, and a root finding method to find h_a . We can specify the fluid depth at any location y_a in the channel, but choose $y_a = 1$, and set $h_a = h_r = h(1)$, the depth at the outside wall of the channel, to improve the numerical conditioning of the root-finding algorithm. At the outer wall, the fluid depth is most sensitive to flux, whereas at inner wall it is, in general, least sensitive. Small changes in the depth at the inner wall can cause very large changes in the flux, which makes calculating the appropriate depth there more difficult than at the outer wall. Whilst this is not always the case, we have found that specifying the depth at the outer wall usually results in better conditioning than for other choices.

3.4.1 Scaling

Thus far, we have not specified the velocity scale, U , and depth scale, δ , or equivalently, set the Reynolds and Froude numbers. To choose these scales, we examine the governing equations. Noting that the gravitational forcing term in (3.3.3b) may be written as

$$\frac{\text{Re}}{\text{Fr}^2} \frac{\Lambda}{\sqrt{1 + \Lambda^2}}, \quad (3.4.24)$$

we choose to set

$$\frac{\text{Re}}{\text{Fr}^2} \frac{\lambda}{\sqrt{1 + \lambda^2}} = 1, \quad (3.4.25)$$

so that the term has unit value at the channel centreline $y = 0$. In addition, to ensure non-trivial free-surface profiles for any choice of ϵ and λ , we set the coefficient of h^4 in (3.4.13) to have unit value at $y = 0$, so that

$$\frac{6}{35} \text{Re} \frac{\epsilon \lambda}{1 + \lambda^2} = 1. \quad (3.4.26)$$

With these scalings, the velocity scale is

$$U = \left(\left[\frac{35}{6\epsilon} \right]^2 \frac{[1 + \lambda^2]^{3/2} g \mu}{\lambda \epsilon^2 \rho} \right)^{1/3} \quad (3.4.27)$$

and the thin-film parameter is

$$\delta = \frac{1}{a} \left(\frac{35}{6} \frac{[1 + \lambda^2]^{3/2} \mu^2}{\epsilon \lambda^2 g \rho^2} \right)^{1/3}. \quad (3.4.28)$$

Note that our thin-film assumption requires $\delta \ll 1$, and this limits the possible values of the parameters. For example, for a 1m wide channel ($a = 1/2\text{m}$) carrying water ($\mu = 10^{-3} \text{ kg m}^{-1} \text{ s}^{-1}$, $\rho = 10^3 \text{ kg m}^{-3}$), and substituting $g = 9.81 \text{ m s}^{-2}$, we require

$$\frac{\epsilon \lambda^2}{(1 + \lambda^2)^{3/2}} \gg 5 \times 10^{-12} \quad (3.4.29)$$

to ensure that δ remains small. This inequality fails to hold in only a very small part of the parameter space, when the channel approaches a very

straight ($\epsilon \rightarrow 0$), flat ($\lambda \rightarrow 0$), or steep (very large λ) geometry, which are not of interest here.

With this scaling, and specifying the fluid depth at the outside channel wall, our free-surface equation (3.4.17) becomes

$$h(y) = \Upsilon(y)^{9/16} \left(\Upsilon(1)^{27/16} h_r^{-3} - \frac{24 [1 + \lambda^2]^{3/2}}{19 \epsilon \lambda^2} [\Upsilon(1)^{19/16} - \Upsilon(y)^{19/16}] \right)^{-1/3}. \quad (3.4.30)$$

3.5 Results

We now use our analytic solution to investigate the effects on the free-surface profile and pressure and velocity fields of the main parameters of the model: the modified curvature of the channel centreline, ϵ , the centreline slope, λ , and the flux, \hat{Q} . In section 3.5.1 we consider the free-surface profile from which we determine the fluid velocity components and pressure. In section 3.5.2 we present several velocity and pressure profiles, and discuss general features of the results. We give particular attention to large flux in section 3.5.3.

3.5.1 Free-surface profile

Figures 3.1 and 3.2 show some representative free-surface profiles for different choices of λ and ϵ at a fixed flux $\hat{Q} = 1$. These illustrate some of the qualitatively different types of free-surface profile that are possible with different channel geometry parameters ϵ and λ .

For sufficiently small slope, the fluid depth at the inside (left) wall of the channel, $h_l = h(-1)$, decreases with increasing curvature ϵ and the fluid depth increases monotonically across the width of the channel from the inside

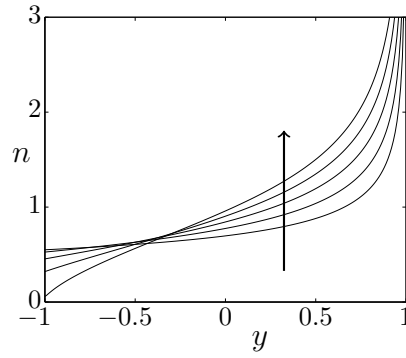
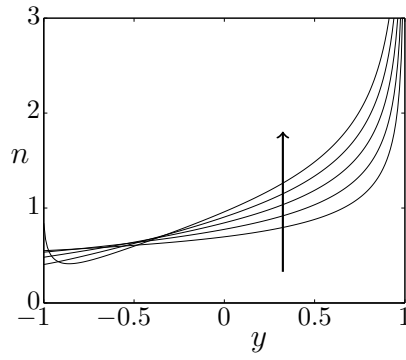
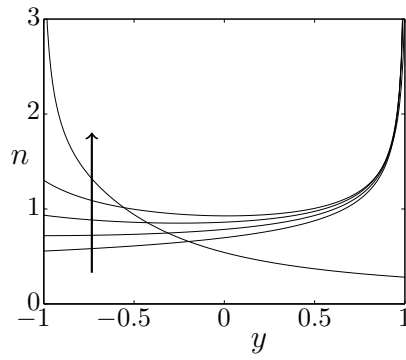
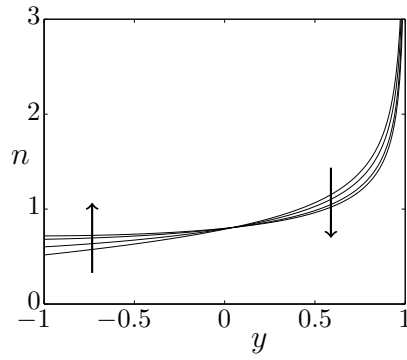
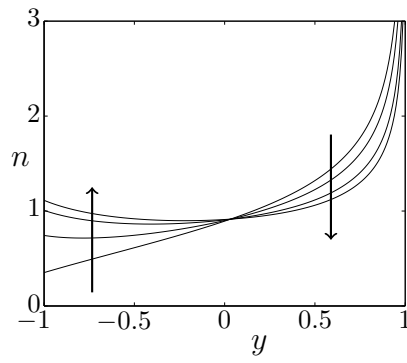
(a) $\lambda = 0.01$ (b) $\lambda = 0.2$ (c) $\lambda = 5$

Figure 3.1: Free-surface profiles for fixed slope λ , for curvatures $\epsilon = 0.01, 0.255, 0.5, 0.745, 0.99$, and flux $\hat{Q} = 1$. Arrows show direction of increasing ϵ .

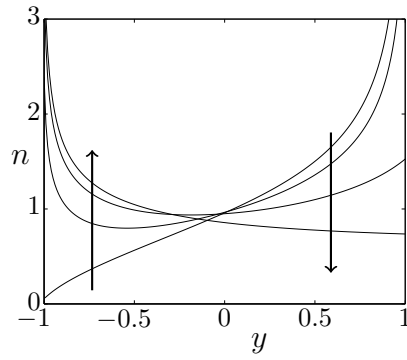
3. Particle-free flow in channels with rectangular cross-section



(a) $\epsilon = 0.3$



(b) $\epsilon = 0.7$



(c) $\epsilon = 0.99$

Figure 3.2: Free-surface profiles for fixed curvature ϵ , with slopes $\lambda = 0.01, 0.67, 1.34, 2$, and flux $\hat{Q} = 1$. Arrows show direction of increasing λ .

to the outside wall; figure 3.1(a). For any ϵ , h_l increases with λ (figure 3.2), and for ϵ not too close to unity, the fluid depth increases monotonically across the width of the channel from inside to outside wall; figures 3.1(a) and 3.2(a). However, for ϵ sufficiently close to unity and sufficiently large λ , the free surface profile changes significantly, with the fluid depth at first decreasing with distance from the inside wall and then increasing; figures 3.1(b), 3.1(c), 3.2(b) and 3.2(c); there is a build-up of fluid near the inside wall where the channel slope is largest. For very large λ and ϵ very close to unity the fluid depth is largest at the inside wall (where the channel bottom will be near vertical) and decreases monotonically across the width of the channel, figures 3.1(c) and 3.2(c).

For small ϵ , we observe that the solutions become nearly independent of λ (figure 3.2(a)), and, indeed, this is seen from the small ϵ limit of (3.4.30) which is independent of λ :

$$h(y) = \left(h_r^{-3} - 3[y - 1] \right)^{-1/3}. \quad (3.5.1)$$

Note that in this limit, exact expressions can be obtained for the flux, \hat{Q} , and area, $\hat{\Omega}$, as, (Stokes et al., 2013),

$$\hat{Q} = \frac{1}{9} \log(6h_r^{-1/3} + 1) \quad (3.5.2)$$

and

$$\hat{\Omega} = \frac{1}{2h_r^2} \left([1 + 6h_r^3]^{2/3} - 1 \right). \quad (3.5.3)$$

In this regime, the depth at the inside wall has a maximum value of $6^{-1/3}$ as $h_r \rightarrow \infty$. In this case, the flux becomes infinite, and the cross-sectional area approaches $(9/2)^{1/3}$.

As ϵ increases to near unity, the free surface solution becomes more sensitive to changes in λ . This is intuitive — at large ϵ the slope of the channel changes significantly across its width, and so the effects of changing λ will be greater.

Increasing flux (with fixed ϵ and λ) always increases the fluid depth at any point in the channel, and the fluid depth at the outer wall, h_r , grows without

bound as flux becomes infinite; see figure 3.3. Increasing flux tends to increase h_r more than h_l , *i.e.*, the depth at the outside wall is much more sensitive to changes in flux.

We can explain the free-surface profiles that we observe physically, in terms of two competing mechanisms, corresponding to the two terms on the right of the free-surface equation (3.4.13). Centrifugal force pushes the fluid to the outside wall of the channel, which is exacerbated by increasing the flux. This effect was also described by Stokes et al. (2013), and is related to the first term on the right of our free-surface equation. However the model presented in the current work also includes the effect of the varying slope across the width of the channel (neglected by Stokes et al. (2013) who assumed constant slope). When ϵ is close to unity, and the channel is tightly wound about the vertical axis, the channel slopes much more steeply near the inside wall than at the outside wall. This means the axial flow direction in this region is more aligned with the direction of gravitational acceleration, which results in a significant gravitational effect, captured by the second term on the right of (3.4.13), so that the fluid effectively cascades down the inside of the channel. This gravitational effect is magnified by increasing the slope of the channel centreline, λ . Thus there is a balance between centrifugal effects pushing the fluid to the outer wall, and gravitational effects pulling the fluid downwards and to the steepest part of the channel.

3.5.2 Velocity and pressure profiles

A representative solution for velocity components and pressure is shown in figure 3.4. The parameters used in this figure are chosen for a channel with curvature and slope that roughly correspond to a Vickers FGL commercial spiral separator, ($\epsilon = 0.67$, $\lambda = 0.33$, Holtham, 1992). Streamlines of the secondary flow and contours of the axial velocity and pressure are shown. The secondary flow shows a single rotating cell, cut off by the outer wall. The streamfunction of the secondary flow, ψ , is zero on the free-surface

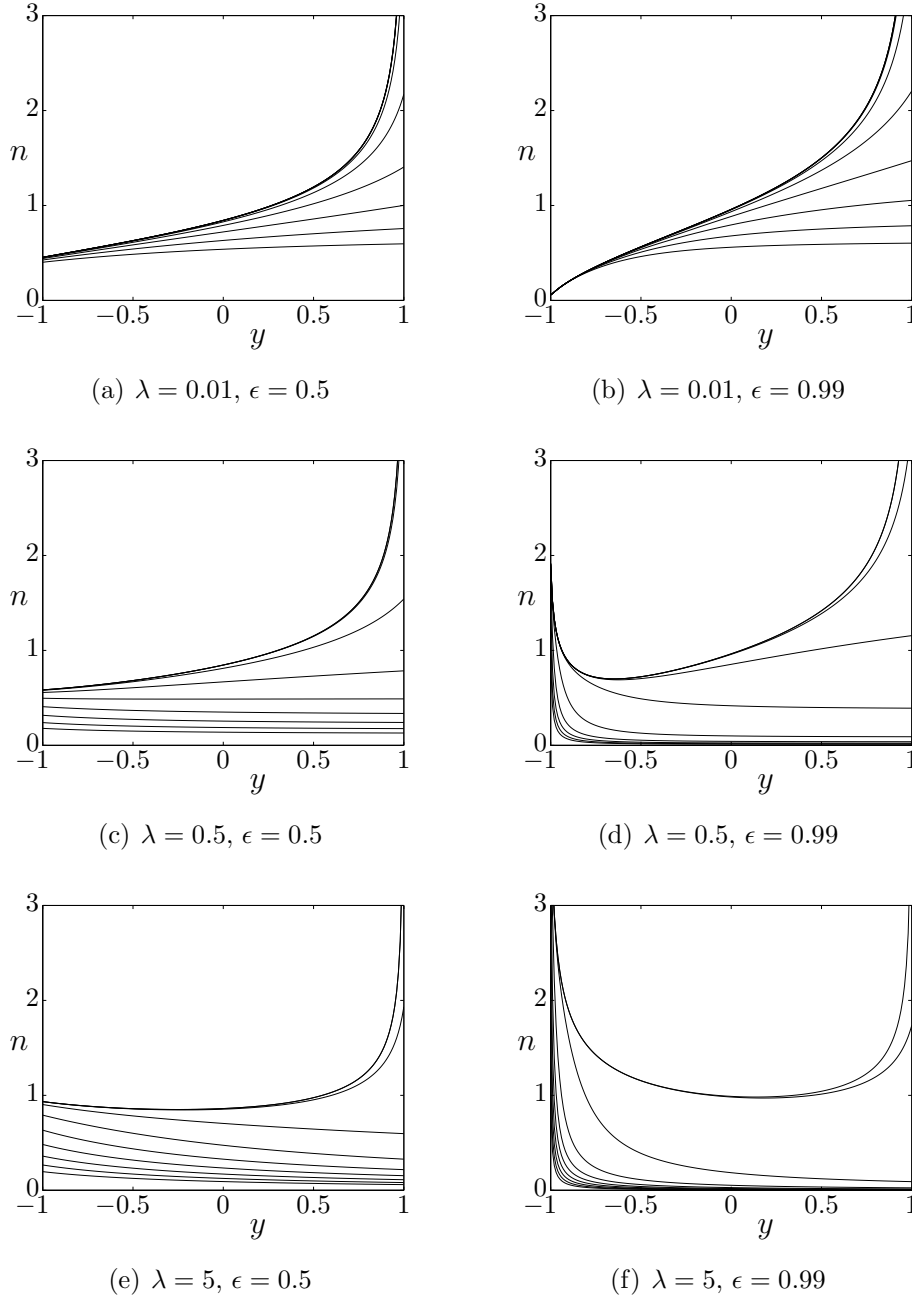


Figure 3.3: Free-surface profile for fixed slope λ and curvature ϵ , with varying flux \hat{Q} ranging from 10^{-3} to the maximum that is computationally possible. From top to bottom, λ is increasing, and from left to right, ϵ is increasing. Increasing flux always increases fluid depth everywhere. Figure 3.3(a) is representative of plots for all λ with $\epsilon \ll 1$.

3. Particle-free flow in channels with rectangular cross-section

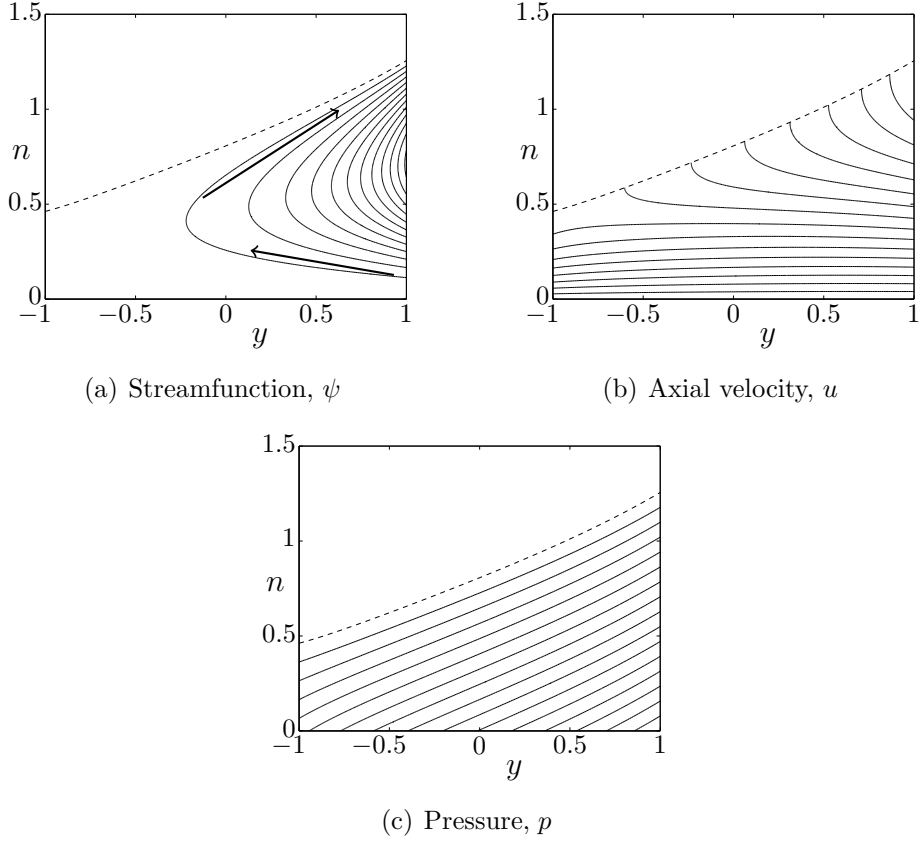


Figure 3.4: Streamlines of the secondary flow and contour plots of axial velocity and pressure, for $\lambda = 0.33$, $\epsilon = 0.67$ and $\hat{Q} = 0.4$. In (a), arrows indicate the direction of the secondary flow.

and channel bottom, however multiple streamlines meet the channel walls, violating the no-slip condition. As explained earlier, this is due to the thin-film scaling. Boundary layers will exist which are not captured by our leading order (in δ) equations. Stokes et al. (2013) compared numerical solutions to the full Navier-Stokes equations with their thin-film results, and found agreement everywhere away from the edges of the channel. Imposing no-slip on the side walls of the channel would cause streamlines to form closed curves, and we would observe a single clockwise-rotating closed cell in the channel cross-section.

In figure 3.4(b), the axial velocity increases as the distance from the channel bottom increases, and the maximum axial velocity occurs at the outside wall of the channel on the free surface. For some choices of the geometry, notably as the slope increases significantly towards the inside wall, the maximum axial velocity can move to the inside wall (figure 3.5), or somewhere between the two walls (figure 3.6), although it always occurs on the free-surface, $n = h(y)$ (the minimum axial velocity is, of course, zero, on the channel bottom). For any choice of parameters, at the free surface we always have a radial velocity $v > 0$ across the whole width of the channel, so we always have transport to the outside of the channel along the free surface. At the channel bottom, we always have radial velocity $v = 0$, but $\partial v / \partial n < 0$ so that near $n = 0$, we have transport to the inside wall of the channel.

Although a single rotating cell (as in figure 3.4(a)) is the most prevalent type of cross-sectional flow, the formation of multiple rotating cells is possible. Figure 3.5(a) shows a case for large λ with two clockwise rotating cells, one close to each wall, within the outer clockwise rotating flow. This change in the flow pattern has potentially important implications for particle segregation. Segregation requires particles of different density to collect in different regions of the channel cross-section and a secondary flow with multiple rotating cells may inhibit or facilitate particle segregation.

A question still under investigation is whether more than two rotating cells can form in a channel with rectangular cross-section. In visualising a large number of cross-sectional flow profiles, we have seen no evidence of more than two cells, nor does our intuition suggest a mechanism by which they could form. However, we cannot, as yet, prove this claim. We note that in arbitrarily shaped channels, studied in chapter 4, many rotating cells are possible.

The case of small slope and flux is also of interest. As shown in figure 3.6 we observe a free-surface with negative second derivative, and the maximum axial velocity occurs away from the channel walls (we note that this is the only

3. Particle-free flow in channels with rectangular cross-section

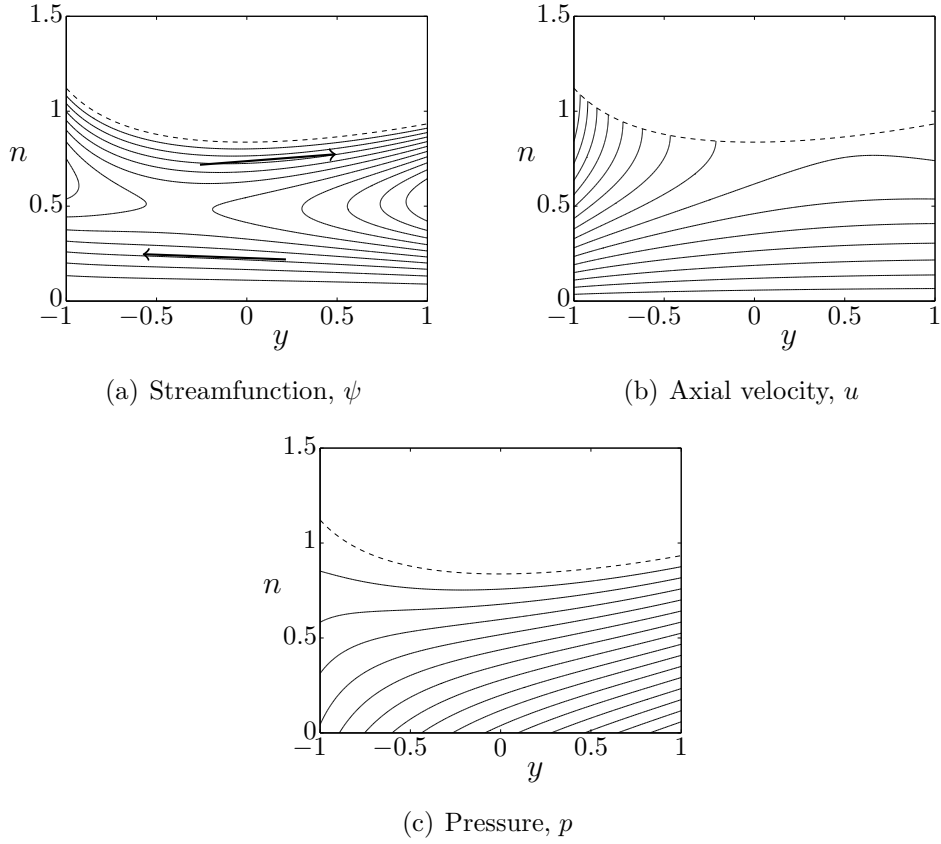


Figure 3.5: Streamlines of the secondary flow and contour plots of axial velocity and pressure, for $\lambda = 1.5$, $\epsilon = 0.8$ and $\hat{Q} = 0.5$. Arrows indicate the direction of the secondary flow in (a).

case consistent with a free-vortex primary flow approximation as assumed by Holland-Batt (1989, 2009)). As flux increases, centrifugal force acts to push the fluid towards the outside wall, reversing the sign of the second derivative of the free-surface profile in the vicinity of that wall.

3.5.3 Large fluid flux

In Stokes et al. (2013), considering the small ϵ and λ case, it was found that as $\hat{Q} \rightarrow \infty$, h_l , the fluid depth at the inside wall of the channel, and $\hat{\Omega}$, the

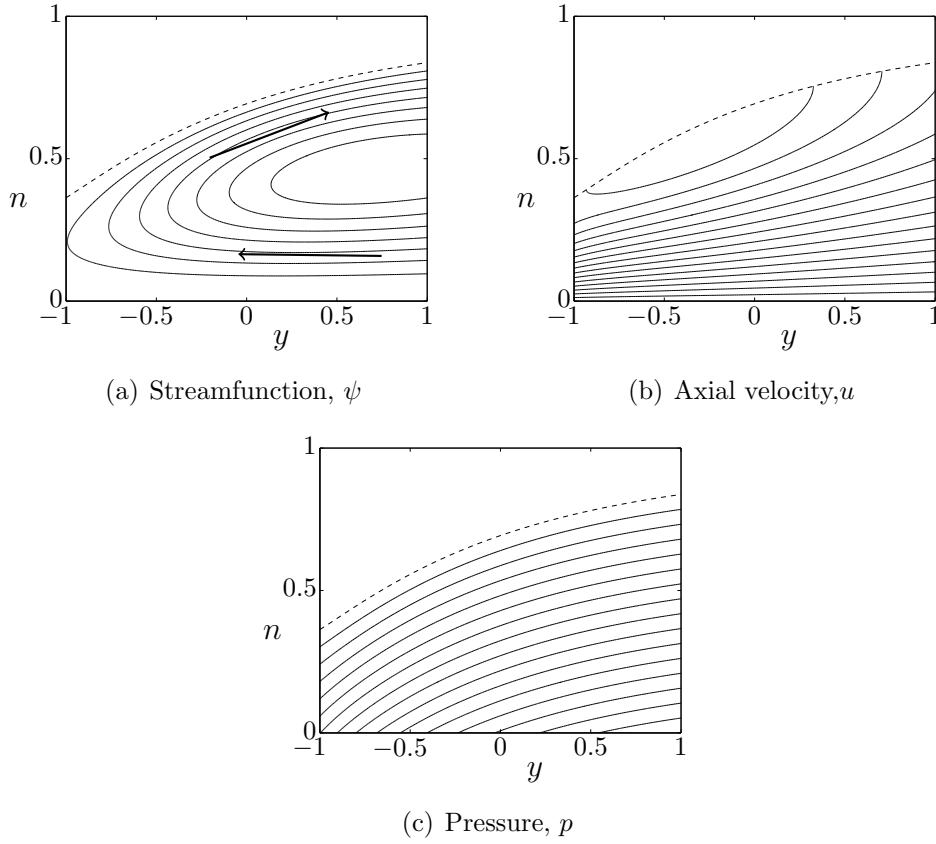


Figure 3.6: Streamlines of the secondary flow and contour plots of axial velocity and pressure, for $\lambda = 0.15$, $\epsilon = 0.75$ and $\hat{Q} = 0.2$. Arrows indicate the direction of the secondary flow in (a).

fluid cross-sectional area, each approached finite limiting values, whilst h_r , the fluid depth at the outside wall, became unbounded. We now examine if this remains true for the more general problem considered here.

Although the flux and area integrals, (3.4.21) and (3.4.23), cannot be evaluated in closed form, elementary manipulations of the free-surface equation

3. Particle-free flow in channels with rectangular cross-section

(3.4.13), allow us to express the cross-sectional area as

$$\begin{aligned}\hat{\Omega} = & \frac{1}{2h_l^2} \left(\frac{\lambda^2 + [1 - \epsilon]^2}{\lambda^2 + 1} \right)^{3/2} + \frac{1}{2} \frac{\epsilon \lambda^2}{(1 + \lambda^2)^{3/2}} \int_{-1}^1 \frac{9\sqrt{\Upsilon}}{4h^2} + 3 \frac{\sqrt{\Upsilon}}{\Lambda^2} \frac{1}{h^2} dy \\ & - \frac{1}{2h_r^2} \left(\frac{\lambda^2 + [1 + \epsilon]^2}{\lambda^2 + 1} \right)^{3/2},\end{aligned}\quad (3.5.4)$$

and the flux as

$$\begin{aligned}\hat{Q} = & \frac{3}{8} \frac{\lambda^2}{1 + \lambda^2} \log \left(\frac{1 + \epsilon}{1 - \epsilon} \right) - \frac{1}{3} \frac{\lambda^2 + (1 - \epsilon)^2}{1 + \lambda^2} \log(h_l) \\ & - \frac{2}{3} \frac{\epsilon}{1 + \lambda^2} \int_{-1}^1 (1 + \epsilon y) \log(h(y)) dy + \frac{1}{3} \frac{\lambda^2 + (1 + \epsilon)^2}{1 + \lambda^2} \log(h_r).\end{aligned}\quad (3.5.5)$$

We further note that there is a maximum possible fluid depth at $y = -1$, h_{l_M} , such that $0 < h_l < h_{l_M}$ where

$$h_{l_M} = \left(\frac{24}{19} \frac{(1 - \epsilon)(1 + \lambda^2)^{3/2}}{\epsilon \lambda^2 \sqrt{\lambda^2 + (1 - \epsilon)^2}} \left[1 - \left\{ \frac{(1 - \epsilon^2)^2 + \lambda^2(1 - \epsilon)^2}{(1 - \epsilon^2)^2 + \lambda^2(1 + \epsilon)^2} \right\}^{19/16} \right] \right)^{-1/3}, \quad (3.5.6)$$

which is found by considering the limit as $h_r \rightarrow \infty$ of (3.4.30) at $y = -1$.

We consider equations (3.5.4) and (3.5.5) in the limit $h_r \rightarrow \infty$. In (3.5.4), all three terms are bounded in this limit, so $\hat{\Omega}$ is bounded. In figure 3.7(a), the complete expression for $\hat{\Omega}$ (evaluated numerically) is plotted, along with the first two terms in (3.5.4), showing the area reaching a limiting value (approximately 2.1 for the parameter values chosen). It can be shown that the first three terms in (3.5.5) are bounded as $h_r \rightarrow \infty$, and hence

$$\hat{Q} \sim \frac{1}{3} \frac{\lambda^2 + (1 + \epsilon)^2}{1 + \lambda^2} \log(h_r) \quad \text{as } h_r \rightarrow \infty. \quad (3.5.7)$$

This behaviour is illustrated by figure 3.7(b), for the case $\lambda = 0.5$, $\epsilon = 0.5$. We have thus confirmed that for large fluxes ($\hat{Q} \rightarrow \infty$), the qualitative behaviour of h_l , h_r and $\hat{\Omega}$ is the same as that found in Stokes et al. (2013).

The maximum fluid depth at the inner wall, h_{l_M} is plotted against ϵ for different values of λ in figure 3.8. For $\epsilon < 1$, h_{l_M} is bounded. In the limit

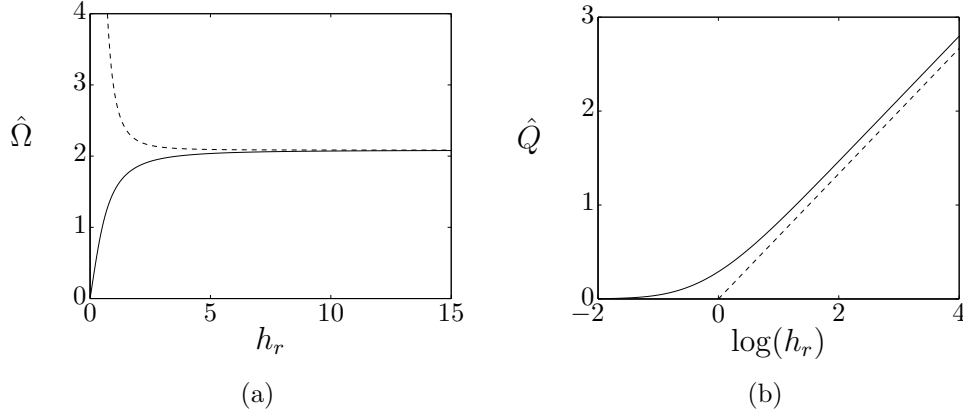


Figure 3.7: The dependence of (a) cross-sectional area $\hat{\Omega}$, and (b) flux \hat{Q} on h_r with $\epsilon = 0.5$ and $\lambda = 0.5$. Note different x -axes. The solid curves are given by (3.5.4) and (3.5.5) respectively; the dashed curves are (a) the first two terms, and (b) the last term of these expressions.

$\epsilon \rightarrow 0$, (3.5.6) reduces to $h_{l_M} = 6^{-1/3}$, which is independent of λ . Limits of h_{l_M} as $\lambda \rightarrow 0$ and $\lambda \rightarrow \infty$ are also plotted (dashed curves). It can be seen from the plot, and confirmed by taking limits, that as $\epsilon \rightarrow 1$, $h_{l_M} \rightarrow \infty$ for any $\lambda > 0$.

Figure 3.9 shows the effect of increasing the flux, \hat{Q} , on the cross-sectional area of the flow, $\hat{\Omega}$. As shown above, and in Stokes et al. (2013), $\hat{\Omega}$ approaches an upper bound as \hat{Q} becomes large. Roughly speaking, a flux of around two to three is sufficient for $\hat{\Omega}$ to approach its limiting value, corresponding to h_l nearing its limiting value h_{l_M} , and in the specific case $\epsilon = 0.5$ and $\lambda = 0.5$, equivalent to $h_r \approx 10$. This suggests that a flux of roughly two to three is representative of large flux. In this regime, increasing ϵ increases the cross-sectional area. However when flux is small a different relationship is observed. Figure 3.9(b) magnifies the $0 \leq \hat{Q} \leq 0.5$ region of figure 3.9(a), showing the difference more clearly. We see that $\hat{\Omega}$ does not vary significantly until ϵ nears unity, when it decreases. Thus for small flux, cross-sectional area is weakly dependent on ϵ over much of the parameter space, but for large flux the dependence is stronger. Plots (not shown) with fixed ϵ and varying λ ,

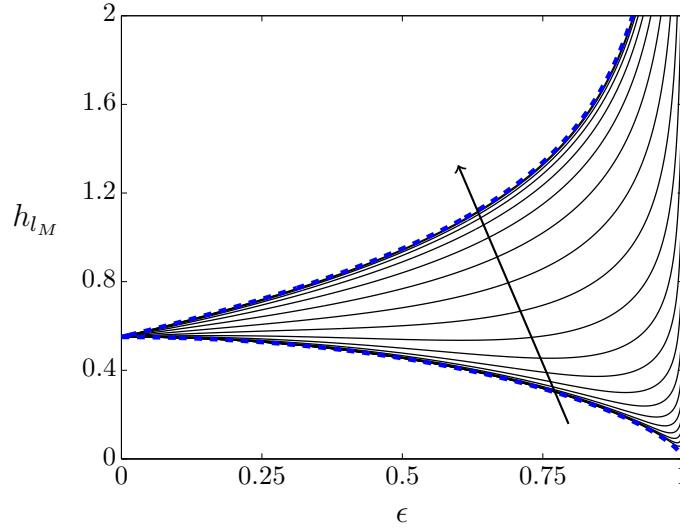


Figure 3.8: Maximum fluid depth at the inside wall, h_{l_M} , against ϵ . Different curves correspond to different values of λ , the arrow showing the direction of increasing λ . Dashed curves are the $\lambda \rightarrow 0$ and $\lambda \rightarrow \infty$ limits.

show little variation, meaning that cross-sectional area depends weakly on the slope of the channel bottom.

3.6 Conclusions

The general solution we obtain in this chapter is valid for rectangular channels with centrelines of arbitrary curvature and torsion. The case where torsion is large at the inside wall but small at the channel centreline, corresponding to ϵ very near 1, was identified in Stokes et al. (2013) as requiring further investigation. In that paper, torsion and curvature were considered constant across the width of the channel, but here we account for their variation. This explains differences observed between our results and those of Stokes et al. (2013).

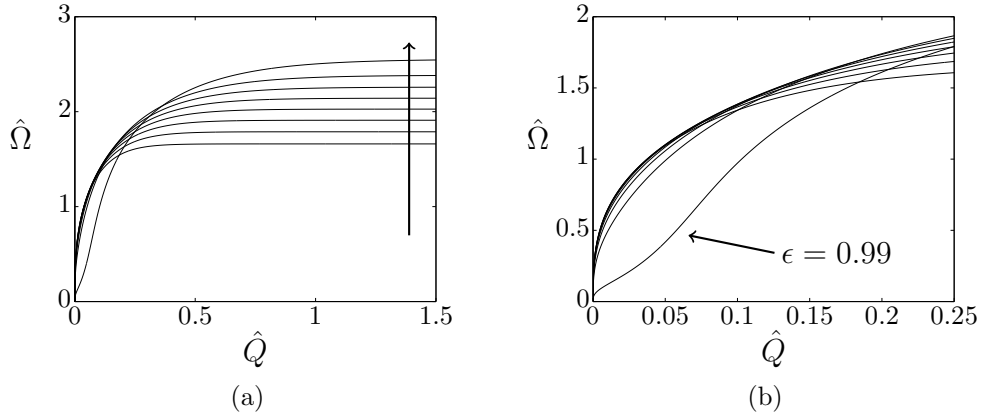


Figure 3.9: Fluid cross-sectional area against flux. Plotted for $\epsilon = 0.01, 0.15, 0.29, 0.43, 0.57, 0.71, 0.85, 0.99$, with $\lambda = 0.5$. The arrow in (a) shows the direction of increasing ϵ .

The free-surface profile is governed by the ordinary differential equation (3.4.13), which has an analytic solution, (3.4.30). Three parameters govern our solutions: ϵ , the modified curvature, λ , the slope of the channel, and \hat{Q} , the dimensionless fluid flux down the channel. All three parameters are important, and their effects are complicated, but we can make general statements about their effects on the solutions, and some conclusions hold independently of geometry. We find the fluid depth at the inside wall (h_l) is bounded for all curvature $\epsilon < 1$, and the fluid depth at the outside wall becomes unbounded ($h_r \rightarrow \infty$) as $\hat{Q} \rightarrow \infty$ for any geometry. We always have transport to the outside of the channel at the free-surface, and transport to the inside of the channel near the bottom. Rotating cells always rotate clockwise. Most other conclusions, however, are dependent on geometry.

The effects of geometry and flux can be characterised by considering the balance of gravitational and centrifugal effects. The steeper the channel, the more aligned the channel bottom with the vertical direction, and hence the stronger the gravitational effects on the flow. We have steep channels for large λ , and at the inside wall when ϵ is large, and in these cases the free surface has a negative gradient at the inside wall. Centrifugal effects are

dominant when the fluid flux is large, when ϵ is small, or λ is not large. They drive fluid to the outside wall of the channel which results in a free surface with positive gradient near this wall. For moderate parameter values we see these two effects competing.

For a channel with small curvature (large centreline radius), the solutions depend weakly on the slope of the centreline. We see the fluid depth increasing monotonically across the channel from inside to outside wall, a single clockwise rotating cell in the cross section, and the maximum axial velocity at the outside wall. For a channel with large curvature (small centreline radius), the solution depends strongly on the slope of the centreline and the flux, and solutions change qualitatively as these parameters vary. For example, in place of a single rotating cell in the cross section, two cells may develop, which has not been previously seen from analyses assuming small torsion or small slope.

The impact of flux and geometry on the flow solution, especially for channels with large curvature, has some practical implications. Whilst the shape of a channel (and thus λ and ϵ) would not change during operation of a spiral separator, the flux may vary, and in some regimes this would significantly affect the flow. This, in turn, might alter the particle separation capabilities of the spiral.

In the next chapter, we study channels with arbitrary cross-section, not just the rectangular channels considered in this chapter. We are interested in determining the effects of channel shape on the resulting flow, and whether the qualitative behaviours we have observed when ϵ and λ are varied also occur in non-rectangular channels. Having considered the effects of ϵ and λ in detail for rectangular channels, we will be able to compare the effects of changing the channel cross-section to the effects of changing ϵ and/or λ . A question that will be of particular interest is how the channel shape will affect the break-up of the flow into multiple rotating cells.

Chapter 4

Particle-free flow in shallow channels with arbitrary cross-section

In chapter 3, we studied flows in channels with rectangular cross-section. For these flows, we made surprising analytic progress. However, particle separators do not typically have rectangular cross-sections, and their shape is expected to have a significant effect on their separation characteristics. Using the equations derived in chapter 2, we now study flows in shallow channels of arbitrary shape, with the goal of understanding the effects of channel shape on the resulting flow. The breakup of the flow into multiple rotating cells was noted in the previous chapter, and this will be investigated further, to see how the channel shape affects the breakup. We consider shallow channels as a perturbation of rectangular channels, which is in accord with the thin-film approximation. This is also justified by the cross-sectional shape of spiral separators which, typically, have a depth that is small in comparison to their width.

4.1 Thin-film equations

The helically-symmetric steady Navier-Stokes equations as shown in section 2.3.6 are very complicated, and some simplifications are necessary to facilitate analytic progress. As in chapter 3, the assumption of helical symmetry means that the flow is independent of distance along helices of pitch $2\pi P$, and our coordinate system allows us to impose this condition by making all quantities independent of the angular coordinate, β . We nondimensionalise the governing equations using the channel half-width, a , and axial velocity scale, U , as follows, (using carets to denote dimensionless variables and parameters)

$$r = a(\hat{A} + \hat{y}), \quad z = a\delta\hat{z}, \quad (4.1.1)$$

$$(v^r, v^\beta, v^z) = (U\delta\hat{v}, U\hat{u}, U\delta^2\hat{w}), \quad (4.1.2)$$

$$p = \frac{\mu U}{a\delta}\hat{p}, \quad H(r) = a\delta\hat{H}(\hat{y}). \quad (4.1.3)$$

Recall that \hat{y} is a dimensionless radial position variable, measured from the designated centreline of the channel. Since the fluid depths in spiral separators are typically very small relative to the channel width, we use a thin-film approximation. We define a characteristic fluid depth, \bar{h} , so that $\delta = \bar{h}/a$ is a measure of the aspect ratio of the fluid. In the thin-film approximation, we assume $\delta \ll 1$. Explicit definitions of U and δ in terms of the physical parameters of the problem are different to those given in chapter 3, and will be given later.

We next recall some notation as used in chapter 3. The channel centreline has dimensionless radius $\hat{A} = A/a$, and we define $\epsilon = a/A = 1/\hat{A}$. The dimensionless pitch of the channel centreline is $\hat{P} = P/a$, and the slope of the channel centreline, λ , is given by $\lambda = \hat{P}/\hat{A}$. The torsion, τ , and curvature, κ , of the channel at \hat{y} are given by

$$\kappa(\hat{y}) = \frac{\epsilon}{(1 + \epsilon\hat{y})\Upsilon(\hat{y})}, \quad \tau(\hat{y}) = \Lambda(\hat{y})\kappa(\hat{y}), \quad (4.1.4)$$

where

$$\Lambda(\hat{y}) = \frac{\lambda}{1 + \epsilon\hat{y}}, \quad (4.1.5)$$

is the slope of the channel bottom at \hat{y} , and

$$\Upsilon(\hat{y}) = 1 + \Lambda(\hat{y})^2. \quad (4.1.6)$$

In chapter 3, we replaced the vertical coordinate direction with a direction normal to the channel bottom. In this chapter, we will not do this, and just use the vertical direction, along with the radial and axial directions. The normal coordinate direction is more difficult to visualise than the vertical direction, especially for non-rectangular channels, and increases the complexity of the equations. It can also lead to non-uniqueness of coordinates for points in the fluid domain.

After nondimensionalising the helically-symmetric Navier-Stokes equations (2.3.19), and taking the thin-film limit, $\delta \rightarrow 0$, we obtain, at leading order (dropping carets as all variables are dimensionless),

$$\frac{\partial^2 v}{\partial z^2} = -\frac{\epsilon \text{Re}}{(1 + \epsilon y)\Upsilon^2} u^2 + \frac{1}{\Upsilon} \frac{\partial p}{\partial y} - \frac{2\epsilon\Lambda}{(1 + \epsilon y)\Upsilon^{3/2}} \frac{\partial u}{\partial z} - \frac{1}{\Upsilon} \frac{\partial p}{\partial z} \frac{dH}{dy}, \quad (4.1.7a)$$

$$\frac{\partial^2 u}{\partial z^2} = -\frac{\Lambda}{\sqrt{\Upsilon}} \frac{\partial p}{\partial z}, \quad (4.1.7b)$$

$$\frac{\partial p}{\partial z} = -\frac{\text{Re}}{\text{Fr}^2} \frac{1}{\Upsilon}, \quad (4.1.7c)$$

and

$$\frac{\partial v}{\partial y} + \frac{\epsilon v}{1 + \epsilon y} + \frac{\partial w}{\partial z} = 0, \quad (4.1.8)$$

where we have defined the Reynolds number, Re , and Froude number, Fr , as

$$\text{Re} = \frac{\rho U a \delta}{\mu}, \quad \text{Fr} = \frac{U}{\sqrt{g a \delta}}. \quad (4.1.9)$$

The boundary conditions are no-slip on the channel bottom,

$$u = v = w = 0 \text{ on } z = 0, \quad (4.1.10)$$

no stress on the free surface,

$$p = \frac{\partial u}{\partial z} = \frac{\partial v}{\partial z} = 0 \text{ on } z = h(y), \quad (4.1.11)$$

and the kinematic condition at the free surface,

$$v \frac{dh}{dy} = w \text{ on } z = h(y). \quad (4.1.12)$$

As discussed in chapter 3, we cannot impose no-slip conditions at vertical channel walls, where they exist. This is a result of the thin-film scaling, and we would anticipate the presence of thin-boundary layers near vertical walls, which are not captured in our leading-order equations. As discussed in chapter 3, these are not expected to have a significant effect on the flow away from the vertical walls. Using a nearly-rectangular channel, we will demonstrate this in section 4.3.1.

4.2 Solution of the thin-film equations

We solve the Navier-Stokes equations (4.1.7a)–(4.1.7c) by integrating sequentially, subject to boundary conditions, to give the pressure,

$$p = -\frac{\text{Re}}{\text{Fr}^2} \frac{(z - h)}{\Upsilon}, \quad (4.2.1)$$

axial velocity,

$$u = \frac{\text{Re}}{\text{Fr}^2} \frac{\Lambda}{\Upsilon^{3/2}} \frac{z(z - 2h)}{2}, \quad (4.2.2)$$

and radial velocity,

$$\begin{aligned} v = & -\frac{\text{Re}^3}{\text{Fr}^4} \frac{\epsilon \Lambda^2}{(1 + \epsilon y) \Upsilon^5} \frac{z(z^5 - 6hz^4 + 10h^2z^3 - 16h^5)}{120} \\ & - 2 \frac{\text{Re}}{\text{Fr}^2} \frac{\epsilon \Lambda^2}{(1 + \epsilon y) \Upsilon^3} \frac{(z - h)^3 + h^3}{3} + \frac{\text{Re}}{\text{Fr}^2} \frac{1}{\Upsilon^2} \frac{d}{dy} (H + h) \frac{z(z - 2h)}{2}. \end{aligned} \quad (4.2.3)$$

As in chapter 3, by integrating the continuity equation (4.1.8), changing the order of differentiation and integration, and requiring that there be no net flux into or out of the fluid domain, we obtain

$$\int_0^{h(y)} v \, dz = 0 \quad (4.2.4)$$

which is be evaluated and rearranged to give a differential equation for the fluid depth $h(y)$, as

$$\frac{dh}{dy} = \frac{6}{35} \frac{\text{Re}^2}{\text{Fr}^2} \frac{\epsilon \Lambda^2}{(1 + \epsilon y) \Upsilon^3} h^4 - \frac{3}{2} \frac{\epsilon \Lambda^2}{(1 + \epsilon y) \Upsilon} h - \frac{dH}{dy}. \quad (4.2.5)$$

This is a Chini differential equation, and in general has no analytic solution. In the rectangular channel case with $H(y) = 0$, considered in chapter 3, the free surface equation can be solved analytically. In general however, we must solve equation (4.2.5) numerically. Substituting (4.2.5) into (4.2.3) gives a simpler form for the radial velocity component,

$$v = - \frac{\text{Re}^3}{\text{Fr}^4} \frac{\epsilon \Lambda^2}{(1 + \epsilon y) \Upsilon^5} \frac{7z^6 - 42hz^5 + 70h^2z^4 - 72h^4z^2 + 32h^5z}{840} - \frac{\text{Re}}{\text{Fr}^2} \frac{\epsilon \Lambda^2}{(1 + \epsilon y) \Upsilon^3} \frac{8z^3 - 15hz^2 + 6h^2z}{12}. \quad (4.2.6)$$

We note that due to the very large denominator in the first term, v is approximately zero when the second term is zero, which occurs when

$$z = \frac{15 - \sqrt{33}}{16} h \approx 0.5785h. \quad (4.2.7)$$

Thus the secondary flow has no radial component at roughly 58% of the fluid depth.

We define the streamfunction for the secondary flow, ψ , by,

$$\frac{\partial \psi}{\partial z} = (1 + \epsilon y)v, \quad \frac{\partial \psi}{\partial y} = -(1 + \epsilon y)w, \quad (4.2.8)$$

and by specifying $\psi = 0$ on the channel bottom $z = 0$, and free surface $z = h(y)$, which together form a closed streamline. Integrating the first

4. Particle-free flow in shallow channels with arbitrary cross-section

equation in (4.2.8), we obtain the streamfunction as

$$\begin{aligned} \psi = & -\frac{\text{Re}^3 \epsilon \Lambda^2}{\text{Fr}^4 \Upsilon^5} \frac{z^2(z-h)(z-2h)^2(z^2-2hz-4h^2)}{840} \\ & -\frac{\text{Re} \epsilon \Lambda^2}{\text{Fr}^2 \Upsilon^3} \frac{z^2(z-h)(2z-3h)}{12}, \end{aligned} \quad (4.2.9)$$

which could be substituted into the second equation in (4.2.8) to give the vertical velocity w .

The fluid flux down the channel, Q (scaled by $\delta a^2 U$), is given by

$$\begin{aligned} Q = & -\int_{y_l}^{y_r} \int_0^{h(y)} u(z, y) \, dz \, dy \\ = & \frac{1}{3} \frac{\text{Re}}{\text{Fr}^2} \int_{y_l}^{y_r} \frac{\Lambda h^3}{\Upsilon^{3/2}} \, dy, \end{aligned} \quad (4.2.10)$$

where $y = y_l$ and $y = y_r$ are the left and right contact points of the free surface with the channel wall(s) or channel bottom. The minus sign appears in equation (4.2.10) because the positive axial direction points in the upstream direction, thus u is negative. The cross-sectional area of the fluid, scaled by δa^2 , is given by

$$\Omega = \int_{y_l}^{y_r} h \, dy. \quad (4.2.11)$$

These integrals cannot be computed exactly (even in the rectangular-channel case) and must be determined numerically.

In order to examine solutions, we must prescribe the velocity scale, U , and thin-film parameter δ . Similar to chapter 3, to give non-trivial free surface shapes and flow solutions we require that the coefficient on the $z(z-2h)/2$ term in (4.2.2), and the coefficient on the h^4 term in (4.2.5) both have unit value at $y = 0$. These scalings give,

$$\frac{\text{Re}}{\text{Fr}^2} \frac{\lambda}{(1+\lambda^2)^{3/2}} = 1 \quad \text{and} \quad \frac{6}{35} \text{Re} \frac{\epsilon \lambda}{(1+\lambda^2)^{3/2}} = 1, \quad (4.2.12)$$

which can be rearranged, using the definitions of the Reynolds and Froude numbers as given previously, to give expressions for the velocity and film-thickness scales U and δ in terms of the geometric and fluid parameters,

as

$$U = \left[\left(\frac{35}{6\epsilon} \right)^2 \frac{1 + \lambda^2}{\lambda} \frac{g\mu}{\rho} \right]^{1/3} \quad \text{and} \quad \delta = \frac{1}{a} \left[\frac{35}{6} \frac{(1 + \lambda^2)^3}{\epsilon\lambda^2} \frac{\mu^2}{g\rho^2} \right]^{1/3}. \quad (4.2.13)$$

The thin-film assumption requires $\delta \ll 1$, and using typical values for a channel of half-width $a = 0.1$ m carrying water ($\rho = 10^3$ kg m⁻³, $\mu = 10^{-3}$ kg m⁻³), this means we require

$$\frac{(1 + \lambda^2)^3}{\epsilon\lambda^2} \ll 10^{10}, \quad (4.2.14)$$

which is always true for channels of physical interest, and fails only for very flat ($\lambda \rightarrow 0$), gently curving ($\epsilon \rightarrow 0$), or steeply sloping ($\lambda \rightarrow \infty$) channels.

4.2.1 Implementation

In chapter 2, in which $H(y) = 0$, $y_l = -1$ and $y_r = 1$, once the radius and pitch of the channel centreline were defined (using ϵ and λ), the only parameters remaining to be determined were h_l and h_r , the fluid depths at the left and right channel walls, and \hat{Q} , the fluid flux down the channel. Specifying any one of these three parameters determined the other two. The flux was chosen as the most physically relevant parameter to specify. For a channel with arbitrary cross section, we must add y_l and y_r to the parameters of the problem, which now number five, $\{y_l, y_r, h_l, h_r, \hat{Q}\}$. Three of these must be specified, which determine the other two. It is possible to have zero or non-zero fluid depth at either edge of the fluid domain, leading to several different cases. We note that $h_l \geq 0$ and $h_r \geq 0$, with non-zero values meaning there is a vertical channel wall at the corresponding y_l and/or y_r . For any channel shape, we can again specify the flux, and any two of $\{y_l, y_r, h_l, h_r\}$ depending on the problem of interest. The process to obtain a solution is summarised in the following steps

1. Choose the channel cross-sectional shape $H(y)$, geometric parameters ϵ and λ , and the flux \hat{Q} .

2. Choose values of two of the parameters from $\{y_l, y_r, h_l, h_r\}$.
3. Use a root-finding algorithm and the free surface equation to determine the remaining two unknown parameters to match the target flux.

We sometimes choose not to prescribe a flux but simply specify three of the four geometrical parameters and directly calculate the fourth and the resultant flux.

4.3 Results

We now investigate solutions of the thin-film equations. In chapter 3 we examined rectangular channels and drew several conclusions about the effects of the modified curvature ϵ and pitch λ of the channel centreline, and the flux \hat{Q} on the resultant flow. In section 4.3.1 we show some results from channels with rectangular cross-section, and by comparing with a nearly-rectangular channel (with no slip on the entire channel surface), demonstrate the small inaccuracy that arises from our inability to impose the no-slip boundary condition on vertical channel walls. We then move on to investigate non-rectangular channels more generally. In section 4.3.2 we consider channels with sloping bottoms, which for small slopes are very similar to rectangular channels. We also consider so-called tick-shaped channels, with larger slope and a vertical wall on only one side of the channel. Finally, in section 4.3.3 we look at some channels with curved bottoms.

4.3.1 Rectangular and nearly-rectangular channels

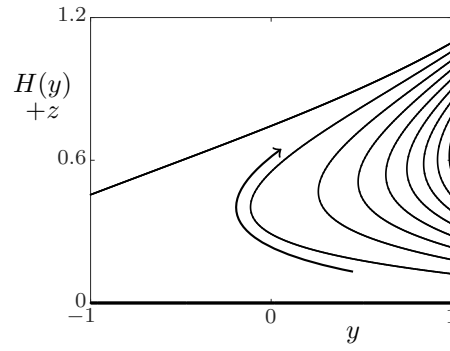
Channels with rectangular cross-section were extensively studied in chapter 3, and we briefly recapitulate some of those results to provide a point of comparison with channels of other shapes, noting that the vertical coor-

dinate direction used here is different to the normal direction used in that chapter. In figures 4.1 and 4.2, we plot free surface profiles and streamlines while varying λ or ϵ , and holding all other parameters constant. The flow always moves from the inside to the outside channel wall at the free surface, and from the outside to the inside wall near the channel bottom. The secondary flow is generally clockwise rotation around some point, but can break into separate clockwise rotating cells (see section 3.5.2). Increasing either λ or ϵ , which increases the slope $\Lambda(y)$ near the inside channel wall, tends to increase the fluid depth at the inside channel wall, whilst decreasing ϵ or λ tends to increase the fluid depth at the outside channel wall. In chapter 3 this behaviour was explained by the competition of two effects, gravitational force pushing fluid to the steepest part of the channel (the inside wall), and inertial forces pushing fluid to the outside channel wall.

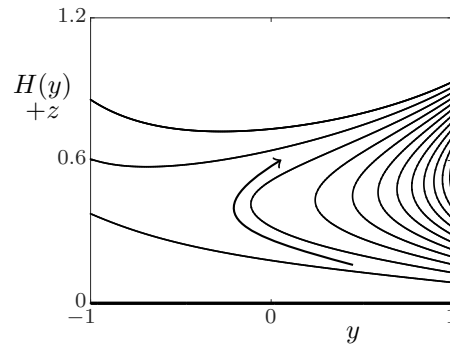
We now consider how our inability to apply the no-slip boundary condition at vertical channel walls affects our results. In section 4.1, it was claimed that in practice we would expect thin boundary layers near the channel walls, which would not have a significant impact on the results, and are not captured in our leading-order thin-film equations. Stokes et al. (2013) compared numerical simulations for a rectangular channel with thin-film results, valid in the limits of small ϵ and λ , which showed excellent agreement away from the channel side walls, and boundary layers near them. We here show the effect of boundary layers by comparing results for a rectangular channel with results for a nearly-rectangular channel with no discontinuities in the slope of the channel wall. We construct such a channel with side walls that smoothly join to the flat channel bottom, using quartic polynomials, as

$$H(y) = \begin{cases} k \frac{(y + y^*)^4}{(1 - y^*)^4}, & -1 \leq y \leq -y^* \\ 0, & -y^* < y < y^* \\ k \frac{(y - y^*)^4}{(1 - y^*)^4}, & y^* \leq y \leq 1 \end{cases}, \quad (4.3.1)$$

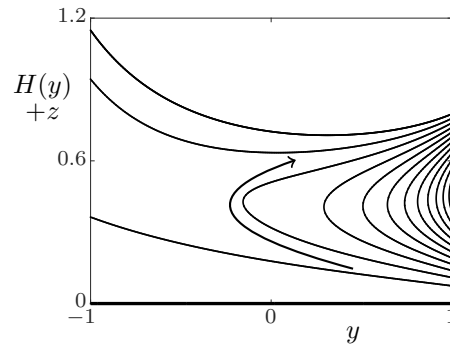
where $\pm y^*$ are the positions where the curved walls meet the horizontal channel bottom, and k is the height at the edges of the channel $y = \pm 1$. The



(a) $\lambda = 0.1$



(b) $\lambda = 0.8$



(c) $\lambda = 1.5$

Figure 4.1: Rectangular channel with $\epsilon = 0.5$, $\hat{Q} = 0.1$, and varying λ . Note the channel bottom is the bottom of the figure, $z = 0$. Arrows indicate direction of secondary flow.

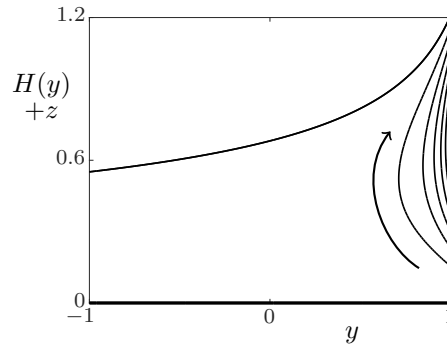
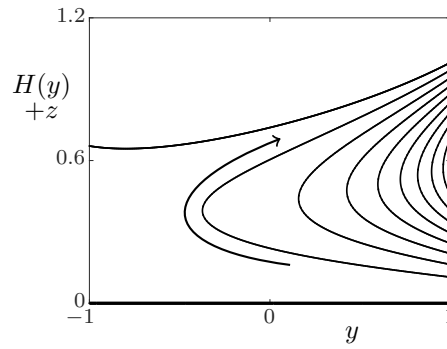
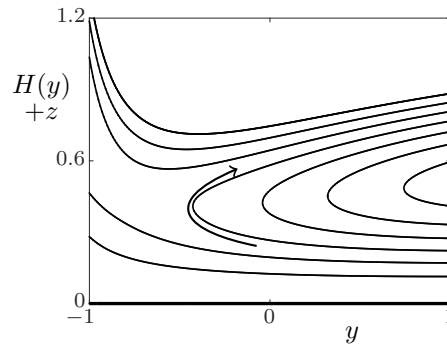
(a) $\epsilon = 0.1$ (b) $\epsilon = 0.5$ (c) $\epsilon = 0.8$

Figure 4.2: Rectangular channel with $\lambda = 0.5$, $\hat{Q} = 0.1$, and varying ϵ . Note the channel bottom is the bottom of the figure, $z = 0$. Arrows indicate direction of secondary flow.

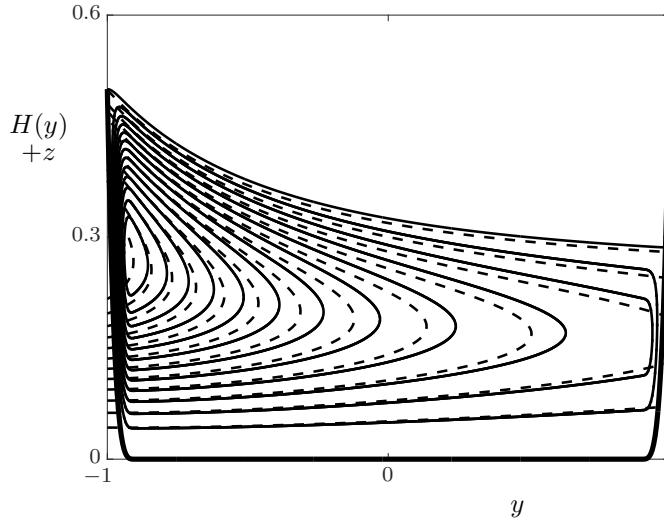


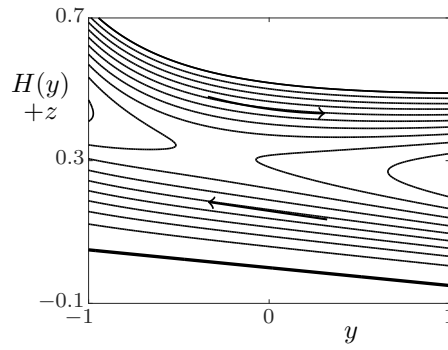
Figure 4.3: Rectangular and nearly-rectangular channel, $\epsilon = 0.5$, $\lambda = 0.7$. Dashed lines correspond to the rectangular channel, and solid lines to the nearly-rectangular approximation. Contour levels are the same in both cases. The free surface is different for each channel, and is represented by the highest streamline.

closer y^* is to 1, the steeper the channel walls, and the closer the approximation to a rectangular channel. The secondary flow for a channel with $k = 0.5$ and $y^* = 0.9$ is shown in figure 4.3 (solid curves), along with that for a rectangular channel with vertical walls (dashed curves). We see very good agreement in the interior of the channel, which, as expected, deteriorates near the edges. The most notable difference is the anticipated existence of boundary layers near the side walls of the nearly-rectangular channel which are not seen for the rectangular channel. The free surface profiles are very similar, although for the same flux the profile of the rectangular channel is slightly lower than the nearly-rectangular channel because of the extra cross-sectional area gained with vertical side walls. This correspondence between the two solutions justifies the study of channels with vertical side walls using the thin-film approximation, with the error introduced by the lack of no-slip boundary condition being a local effect that does not change the qualitative behaviour of the solution.

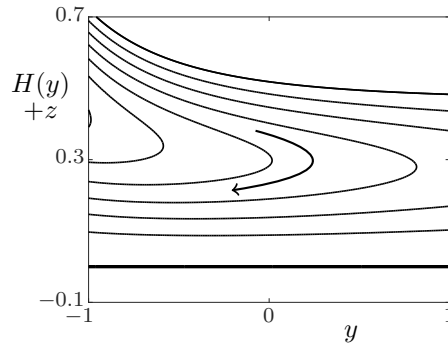
4.3.2 Channels with a sloping bottom

Next we consider channels with a bottom of constant slope k , i.e. $H(y) = ky$. Figure 4.4 shows solutions for three different slopes k , each with the same centreline geometry and flux, $(\epsilon, \lambda$ and $\hat{Q})$. There is little difference in the free surface profiles, but a significant effect of slope on the secondary flow. Figure 4.4(a) shows the secondary flow for a channel with negative slope, which has broken up into two rotating cells. For $k = 0$ and $k = 0.05$, the secondary flow does not exhibit multiple rotating cells. For channels with $\epsilon = 0.5$, $\lambda = 0.75$, and $\hat{Q} = 0.1$, multiple rotating cells are seen for channel slopes less than roughly $k = -0.02$. Thus, the break-up into multiple rotating cells, remarked upon in chapter 3, is not limited to rectangular channels, and is influenced by the slope of the channel bottom. The free surface profiles for the three different channel slopes are very similar, despite the significant changes in the secondary flow. The sensitivity of the free surface profile will be further discussed in section 4.3.3.

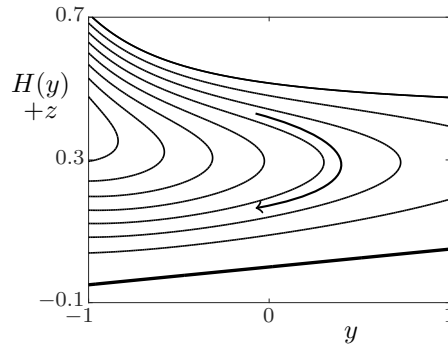
If the free surface contacts the bottom of the channel at one end and there is a vertical channel wall at the other, we have what we term a tick-shaped channel. We have two cases, a channel with positive slope and the vertical wall at the inside of the channel, or a channel with negative slope and a vertical wall at the outside of the channel. We cannot have a flat channel with a vertical wall at one side, as the only solution to the free surface equation in that case would be $h(y) = 0$, a dry channel. The main difference from the sloping channel case is that we specify $y_l = -1$ and $h_r = 0$ or $y_r = 1$ and $h_l = 0$ in addition to the flux, and must determine h_l and y_r , or h_r and y_l , respectively. In figure 4.5 we show the effect of changing the down-channel slope λ on flows in tick shaped channels defined by $H(y) = y/2$ and with $\epsilon = 0.5$ and $\hat{Q} = 0.15$. We see that as the slope λ increases, the fluid tends to move towards the inner channel wall, and the outer contact point also moves inwards. The same behaviour is observed when ϵ is increased (results not shown). This behaviour is qualitatively similar to the rectangular-channel



(a) $k = -0.05$



(b) $k = 0$



(c) $k = 0.05$

Figure 4.4: Sloping channels, $H(y) = ky$, for varying k , with $\epsilon = 0.5$, $\lambda = 0.75$ and $\hat{Q} = 0.1$. Arrows indicate direction of secondary flow. Thicker lines indicate the channel bottom.

case. Figure 4.6 shows the case of a channel bottom with negative slope, $H(y) = -y/2$. As λ increases, we see the inner contact point moving inwards, and the outside fluid depth decreasing. Although not as dramatic as for the upwards sloping tick-shaped channel, the same behaviour is again seen; increasing the slope tends to push fluid to the inside of the channel.

In the limiting case of a gently curving and sloping channel ($\epsilon \rightarrow 0$ and $\lambda \rightarrow 0$) with $H(y) = ky$, the free surface equation (4.2.5) can be written as,

$$\frac{dh}{dy} = h^4 - k. \quad (4.3.2)$$

For a channel bottom profile with positive slope, $k > 0$, this equation has an exact implicit solution. Defining $\chi = |k|^{1/4}$, one obtains

$$y - y_a = \frac{1}{4\chi^3} \log \left(\frac{\chi - h}{\chi + h} \right) - \frac{1}{2\chi^3} \arctan \left(\frac{h}{\chi} \right), \quad (4.3.3)$$

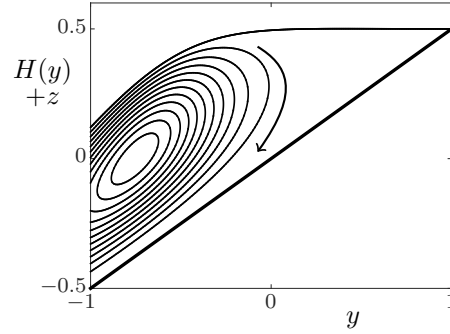
where y_a is the point where the free surface meets the channel bottom. For downwards sloping channels, with $k < 0$, the solution is more complicated:

$$y - y_a = \frac{1}{4\sqrt{2}\chi^3} \log \left(\frac{\chi^2 + \sqrt{2}\chi h + h^2}{\chi^2 - \sqrt{2}\chi h + h^2} \right) + \frac{1}{2\sqrt{2}\chi^3} \arctan \left(\frac{\sqrt{2}\chi h}{\chi^2 - h^2} \right). \quad (4.3.4)$$

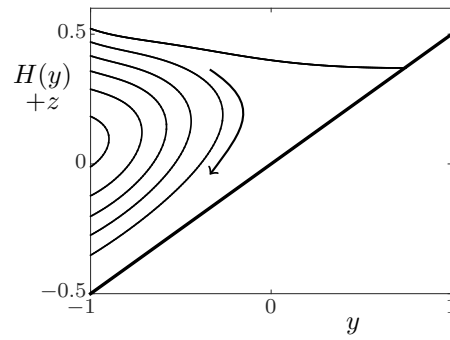
The asymptotic solution (4.3.3) was initially obtained by S. K. Wilson and B. R. Duffy in 2003, as part of collaborative work with Y. M. Stokes on helically-wound channels in the small curvature and small torsion limits, which has not previously been published.

Figure 4.7 shows a comparison between these implicit solutions and numerical solutions to the full free surface equation (4.2.5). Very good agreement is seen, even for the relatively moderate values of ϵ and λ .

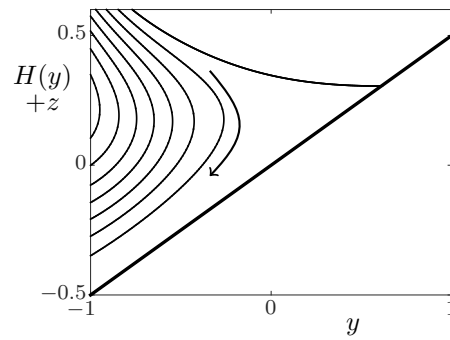
The solutions presented above apply to channels with positive cross-sectional slope $k > 0$ and a vertical wall at the inside of the channel, or to channels with $k < 0$ and a vertical wall at the outside of the channel. Other options at first seem possible, namely $k > 0$ and an outside vertical wall, or $k < 0$ and



(a) $\lambda = 0.2$



(b) $\lambda = 0.8$



(c) $\lambda = 1.4$

Figure 4.5: Tick shaped channel $H(y) = y/2$, varying λ , with $\epsilon = 0.5$ and $\hat{Q} = 0.15$. Arrows indicate direction of secondary flow.

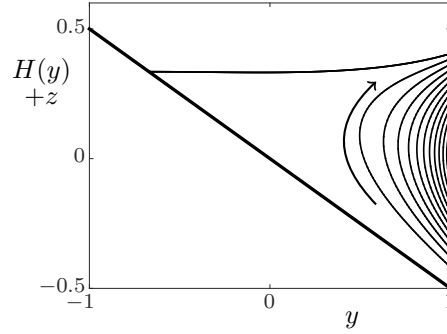
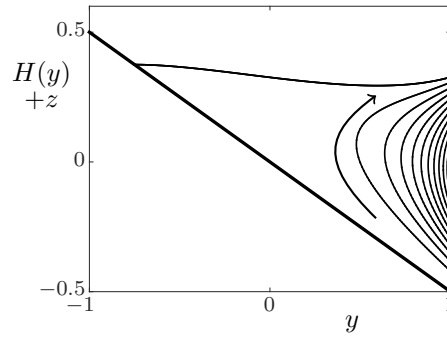
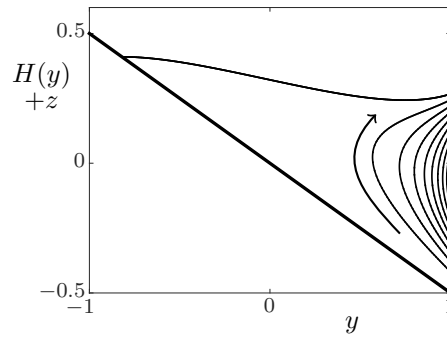
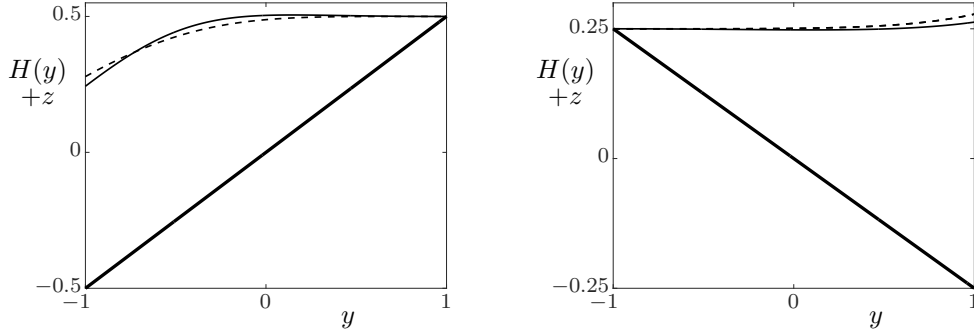
(a) $\lambda = 0.2$ (b) $\lambda = 0.8$ (c) $\lambda = 1.4$

Figure 4.6: Tick shaped channel $H(y) = -y/2$, varying λ , with $\epsilon = 0.5$ and $\hat{Q} = 0.07$. Arrows indicate direction of secondary flow.

4. Particle-free flow in shallow channels with arbitrary cross-section



(a) $H(y) = y/2$, $\epsilon = 0.4$, $\lambda = 0.4$, and $\hat{Q} \approx 0.125$. (b) $H(y) = -y/4$, $\epsilon = 0.1$, $\lambda = 0.4$, and $\hat{Q} \approx 0.021$.

Figure 4.7: Upwards and downwards sloping tick-shaped channels. The dashed line represents the analytic solution in the limit $\epsilon \rightarrow 0$ and $\lambda \rightarrow 0$, and the solid line represents the numerical solution. Note the different parameters and scale in each figure. In both figures, $y_l = -1$ and $y_r = 1$ are specified.

an inside vertical wall. However, these channels have no solution, because for the fluid to meet the channel bottom, its depth $h(y)$ must reach zero. Rearranging the free surface differential equation (4.2.5) gives, when $h(y) = 0$,

$$\frac{d}{dy}(h + H) = 0, \quad (4.3.5)$$

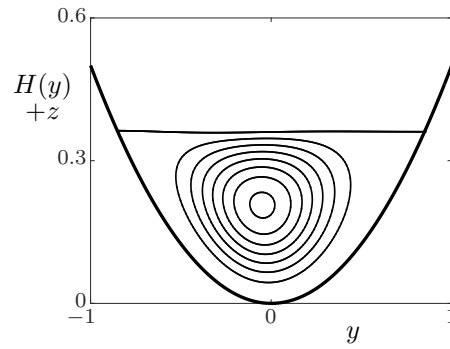
and so the free surface must be horizontal when the depth reaches 0. Geometrically, this means that the fluid can meet the channel bottom at the outside of the channel if $H'(y) > 0$ there (since $h'(y) < 0$ nearby), and at the inside of the channel if $H'(y) < 0$ there (since $h'(y) > 0$ nearby). For tick-shaped channels, these restrictions on the sign of $H'(y)$ near the free surface contact points are only be satisfied in the two types of channels with solutions in equations (4.3.3) and (4.3.4).

4.3.3 Channels with a curved bottom

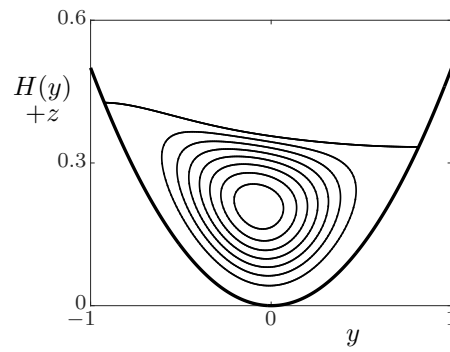
We now consider channels with curved bottoms. Whilst there are many choices, we will first consider a simple parabolic channel $H(y) = 0.5y^2$. In figure 4.8 we present plots for fixed $\epsilon = 0.5$, $\hat{Q} = 0.015$, and three different values of the down-channel slope of the channel centreline, λ . We first note that since there are no vertical channel walls in this case, the no-slip boundary condition is satisfied along the whole channel bottom, and with $h_l = h_r = 0$, we have only to determine the parameters y_l and y_r for a given flux, ϵ and λ . In figure 4.8, we see the change in y_l and y_r with λ , for our fixed ϵ and \hat{Q} . As for other channel shapes we have studied, we see that increasing λ tends to push the fluid to the inside channel wall, which also occurs when ϵ is increased (not shown).

In section 4.3.2, it was noted that the secondary flow could be very sensitive to channel shape, but the free surface was relatively less sensitive. We now show this for differently shaped channels. In figure 4.9 two channels are shown, one with one bump in the bottom and one with two bumps. Both channels have the same centreline radius and pitch, and the same flux. The channel bottom shape has a clear effect on the secondary flow, splitting it into several rotating cells. The free surface profiles, however, remain remarkably similar. The filled circles represent the centres (found using the 58% depth approximation found in equation (4.2.7)) of the rotating cells, and the crosses represent saddle points of the streamfunction. At both the filled circles and crosses, the secondary flow velocity is zero, and there is only an axial component of the fluid velocity.

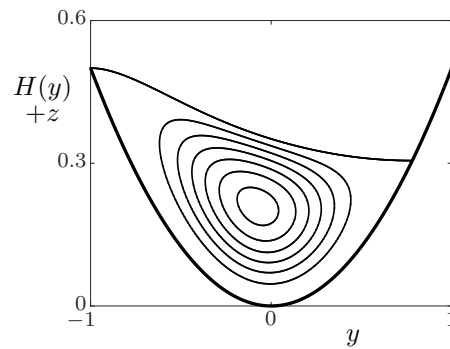
To further investigate the sensitivity of the secondary flow to the channel shape, we consider a rectangular channel with a small bump in the channel bottom. The results for a channel with a growing bump are shown in figure 4.10. In these plots, we prescribe $\hat{Q} = 1$, $y_l = -1$, and $y_r = 1$. We see that the free surface profile is again fairly similar for the three bump heights, but there is a breakup of the single rotating cell seen in figure 4.10(a), into



(a) $\lambda = 0.2$



(b) $\lambda = 0.6$



(c) $\lambda = 1$

Figure 4.8: Parabolic channels with $\epsilon = 0.5$, $\hat{Q} = 0.015$, and varying λ . Flow is clockwise around streamlines.

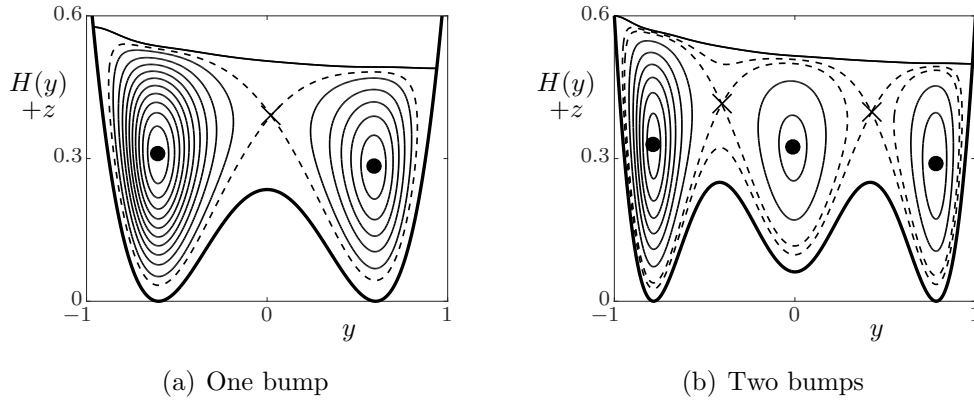
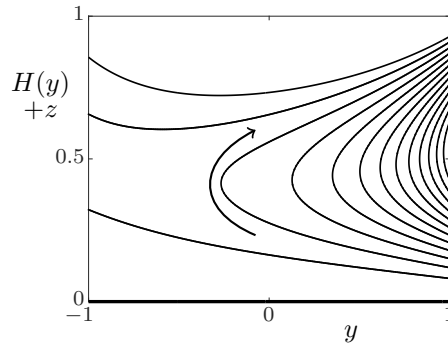


Figure 4.9: Bumpy channels, with $\epsilon = \lambda = 0.6$ and $\hat{Q} \approx 0.042$. Filled circles represent a local maximum of the streamfunction and centre of a clockwise rotating cell, and crosses are saddle points, which are also stagnation points of the secondary flow. Streamlines passing through the stagnation points are indicated as dashed curves.

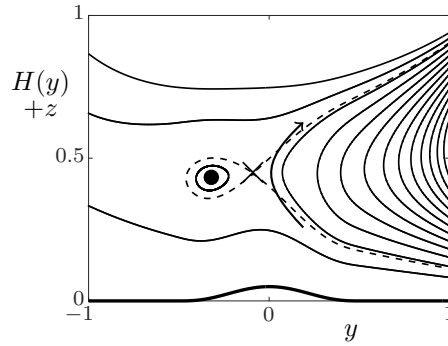
two rotating cells inside a larger rotating cell even when the height of the bump is small, at roughly 5% of the depth of the fluid. As in figure 4.9, the filled circles are the centres of local rotating cells of fluid, although the cells are far less pronounced in this case.

In figure 4.11, we repeat the growing-bump experiment using a parabolic channel with a narrow Gaussian bump, and find again that the flow separates into multiple rotating cells even for a small bump height of 0.05, roughly 10% of the fluid depth. For the larger bump with height 0.1, the separate rotating cells become quite large, and a significant proportion of the cross-sectional flow domain is taken up by these structures.

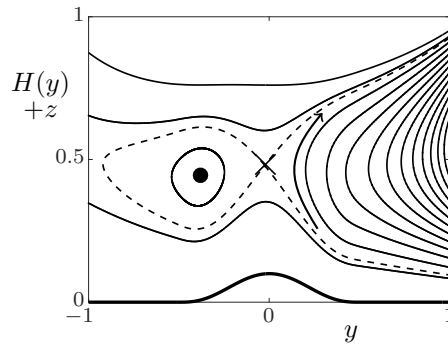
The breakup into multiple rotating cells is of interest in part due to its potential implications on particle separation efficiency in spiral separators. Whilst the break-up into multiple rotating cells can occur in rectangular channels due to the balance of gravitational and inertial effects, it is more readily seen as a result of the channel bottom shape.



(a) No bump

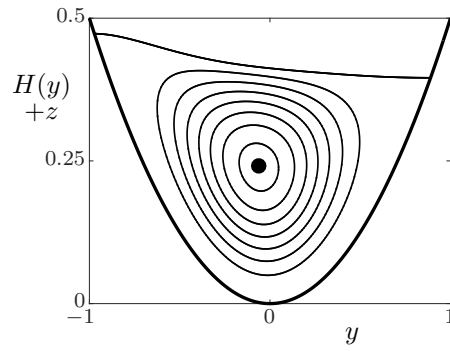


(b) Bump height 0.05

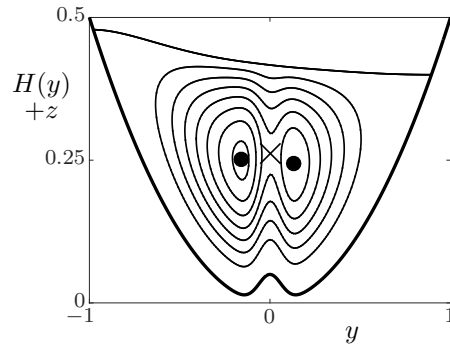


(c) Bump height 0.10

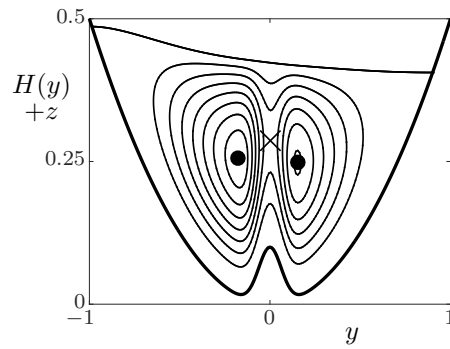
Figure 4.10: Channels with a growing bump in the bottom, $\epsilon = 0.5$, $\lambda = 0.8$, and $\hat{Q} = 1$. Filled circles represent a local maximum of the streamfunction and centre of a clockwise rotating cell, and crosses are saddle points. Dashed streamlines through the stagnation point have been added.



(a) No bump



(b) Bump height 0.05



(c) Bump height 0.10

Figure 4.11: Parabolic channels with a growing Gaussian bump in the bottom, $\epsilon = 0.5$, $\lambda = 0.5$, and $\hat{Q} \approx 0.02$. Filled circles represent a local maximum of the streamfunction and centre of a clockwise rotating cell, and crosses are saddle points.

4.4 Conclusions

We have considered helically-symmetric thin-film flow in helical channels with arbitrary cross-sections. Using a helicoidal body-fitted coordinate system, we obtained a system of equations that were solved to give a simple differential equation for the free surface shape requiring numerical solution. In the special case of small channel centreline torsion and curvature, we obtained analytic solutions for tick-shaped channels.

The effects of changing the slope and radius of the channel centreline (λ and ϵ) were studied extensively for rectangular channels in chapter 3, and we observe the same qualitative behaviours in channels of arbitrary cross-section. The steeper the inside wall of the channel (the larger λ or ϵ), the more the fluid builds up there, and where the channel is less steep, inertial effects push fluid to the outside of the channel. The balance between gravity and inertia may lead to multiple rotating cells of fluid. This was noted in chapter 3. Here we have found that the breakup into multiple rotating cells is also significantly affected by relatively small changes to the channel cross-sectional shape, for example, an increase/decrease in the slope of the channel bottom, or a bump in the channel bottom. In the parabolic channel, multiple rotating cells could not be induced by changing ϵ and λ , but did form as a result of a bump in the channel bottom.

We have found that the secondary flow is relatively sensitive to the channel bottom shape, but the free surface profile is far less sensitive. Bumps with height roughly 5–10% of the fluid depth are sufficient, in some cases, to cause a breakup of the flow into multiple rotating cells. A small change in the slope of a flat channel bottom can also cause such a breakup. This observation is potentially relevant for spiral separators, as it suggests that defects or damage to the channel, or even clumps of particles sticking to the channel bottom, could significantly change the secondary flow in the channel. Given such disturbances are likely to be localised, they may not affect the overall

operation of a spiral particle separator, but to investigate such effects would require a model for particle laden flow that does not assume helical symmetry. This is left for future work.

In the next chapter, we will introduce a model for particle-laden flow (that still assumes helical symmetry) in shallow channels with arbitrarily-shaped cross-sections.

Chapter 5

Particle-laden flow in shallow channels

In chapters 3 and 4 we studied particle-free flows in helical channels. In practice spiral particle separators carry slurries of fluid and particles, so in this chapter we introduce a model for monodisperse particle-laden flows in helical channels.

For spiral separators, an important design goal is to minimise the water needed to segregate a mixture of particles, and so the volume fraction of particles is generally high. This informs the choice of particle-transport model, as there is a two-way coupling between the particle and fluid motion. In particular, models that assume a dilute particle concentration and neglect the two-way coupling between the fluid and particle motion will not be applicable. There are several approaches to modelling flows with high particle concentrations, as discussed in section 1.3. Here we will consider the shear-induced migration model first proposed by Leighton and Acrivos (1987). This model treats the suspension as a Newtonian fluid with variable viscosity and density, both of which depend on the local particle volume fraction. It accounts for particles settling under the effect of gravity, and movement due

to shear which are expected to be the dominant effects in spiral separators. Other phenomena, such as Brownian diffusion, may be included but we leave this for future work. The Leighton and Acrivos (1987) model has previously been used to study particle-laden flow down an inclined plane (Murisic et al., 2011) and validated against experimental data. More recently, it has been used for particle-laden flows in helical channels with small slope, and rectangular cross-section (Lee et al., 2014). We now extend this latter work to the more general case with arbitrary channel slope and cross-sectional shape.

In this chapter, we present the full governing equations for the shear-induced migration model, since they differ in several respects from the standard Navier-Stokes equations presented in chapter 2. We then give a simplified thin-film model. The thin-film model cannot be solved analytically, but under the assumption that the particles are uniformly distributed in the vertical direction, the problem can be reduced to a differential equation for the free-surface profile, which must be solved numerically.

5.1 The particle-laden flow model

We consider a monodisperse suspension of uniformly-sized spherical particles with diameter d . As previously, $a\delta$ is a characteristic fluid depth. We require $d \ll a\delta$, so that the particles are small relative to the fluid depth, and the slurry can be treated as a continuum. We will later give a further restriction on d to ensure that the particles remain large enough to avoid the colloidal limit where Brownian diffusion dominates gravitational settling.

The local particle volume fraction is denoted ϕ , and can vary from 0 (no particles) to a maximum value $0 < \phi_m < 1$ roughly corresponding to the close-packing limit for spheres, where the flow can no longer be modelled as a Newtonian fluid. The local effective viscosity of the fluid is dependent on the particle volume fraction and comes from an empirical model, of which many

exist; see Murisic et al. (2013) for a discussion. We will leave dependence of μ on the particle volume fraction as a general function $\mu = \mu(\phi)$ whilst deriving equations, but when a particular equation is required, we will use the following model, known as the Krieger-Dougherty equation (Murisic et al., 2011),

$$\mu(\phi) = \mu_f \left(1 - \frac{\phi}{\phi_m}\right)^{-2}, \quad (5.1.1)$$

where μ_f is the viscosity of the clear fluid. Various values of ϕ_m are reported in the literature, we will use $\phi_m = 0.61$ as in Murisic et al. (2011). We assume the densities of the particles and fluid are constant, and the local mixture density is given by,

$$\rho(\phi) = \phi\rho_p + (1 - \phi)\rho_f, \quad (5.1.2)$$

where ρ_p and ρ_f are the densities of the particles and fluid, respectively.

As in Phillips et al. (1992), Murisic et al. (2011), and Lee et al. (2014), we assume the particles move with the mixture velocity \mathbf{v} plus components described by the particle flux vector \mathbf{J} . The particle flux vector we adopt describes the movement of particles relative to the suspending fluid due to the effects of gravitational sedimentation and shear-induced migration. The particle flux vector is given by Murisic et al. (2011) and Lee et al. (2014) as,

$$\mathbf{J} = \frac{d^2\phi(\rho_p - \rho_f)}{18\mu(\phi)}\omega(\phi)\mathbf{g} - \frac{K_c d^2}{4}\phi\nabla(\dot{\gamma}\phi) - \frac{K_v d^2}{4}\frac{\phi^2\dot{\gamma}}{\mu}\frac{d\mu}{d\phi}\nabla\phi, \quad (5.1.3)$$

where K_c and K_v are diffusion coefficients and $\dot{\gamma}$ is the local shear rate $\|\nabla\mathbf{v} + (\nabla\mathbf{v})^T\|/4$. This particle flux vector is valid when the diffusion due to shear is much larger than the Brownian diffusion of particles in the solvent. It is valid for unidirectional shear (Phillips et al., 1992), which, although not true in general for the problem of interest here, is the case at leader order. The first term in the expression for \mathbf{J} corresponds to sedimentation, the settling of particles on the channel bottom due to the influence of gravity, and the second and third terms correspond to shear-induced migration, the tendency of particles to move away from areas of high shear (such as near the channel walls) towards areas of low shear (such as the free surface near the centre of the channel). The function $\omega(\phi)$ is a hindrance function that models

the resistance to motion of a single particle based on the local concentration of particles. There are many different models for the hindrance function, however here we use the simple function $\omega(\phi) = 1 - \phi$, valid in the presence of shear (Schafflinger et al., 1990) and used in Murisic et al. (2013) and Lee et al. (2014).

We will model the flow in terms of the mixture velocity, given by the Navier-Stokes equations, an equation for conservation of total mass, and an equation for particle transport and conservation. Allowing for viscosity and density to vary in space, the steady Navier-Stokes equations can be written as,

$$\rho(\mathbf{v} \cdot \nabla \mathbf{v}) = -\nabla p + \mu \nabla \cdot \mathcal{S} + \nabla \mu \cdot \mathcal{S} - \rho g \mathbf{g}_z, \quad (5.1.4)$$

where \mathbf{v} is the mixture velocity, p is the pressure, $\rho = \rho(\phi)$ is the effective density, $\mu = \mu(\phi)$ is the effective viscosity, \mathcal{S} is the usual rate-of-strain tensor, and g is the acceleration due to gravity. In section 5.1.1 we derive the conservation equations for the total mixture and the particle phase, and in section 5.2 we give these equations in expanded component form.

5.1.1 Mass conservation

Consider a fluxed arbitrary fluid volume Ω with boundary $\partial\Omega$, and let \mathbf{n} be the outward pointing normal to $\partial\Omega$. The mass flux of particles across the boundary is

$$(\mathbf{v} \rho_p \phi + \rho_p \mathbf{J}) \cdot \mathbf{n}, \quad (5.1.5)$$

accounting for the movement of particles with the fluid, and due to the particle flux vector. Similarly, the mass flux of fluid across the boundary is

$$(\mathbf{v}(1 - \phi) \rho_f) \cdot \mathbf{n}. \quad (5.1.6)$$

Using the divergence theorem, we can therefore write two conservation equations for the fluid and particle phases as, respectively,

$$\frac{\partial}{\partial t} (\phi \rho_p) + \nabla \cdot (\mathbf{v} \rho_p \phi + \rho_p \mathbf{J}) = 0, \quad (5.1.7)$$

and

$$\frac{\partial}{\partial t}((1 - \phi)\rho_f) + \nabla \cdot (\mathbf{v}\rho_f(1 - \phi)) = 0. \quad (5.1.8)$$

Summing (5.1.7) and (5.1.8) gives the conservation equation of the total mixture,

$$\frac{\partial \rho}{\partial t} + \nabla \cdot (\rho \mathbf{v} + \rho_p \mathbf{J}) = 0, \quad (5.1.9)$$

using $\rho = \phi\rho_p + (1 - \phi)\rho_f$. By taking (5.1.7)/ ρ_p + (5.1.8)/ ρ_f , we obtain

$$\nabla \cdot (\mathbf{v} + \mathbf{J}) = 0, \quad (5.1.10)$$

and taking (5.1.8)/ ρ_f ,

$$\frac{D\phi}{Dt} = (1 - \phi)\nabla \cdot \mathbf{v}. \quad (5.1.11)$$

We use equations (5.1.10) and (5.1.11) to impose conservation of mass for the two phases.

Thus, in place of the usual continuity equation for incompressible flow, $\nabla \cdot \mathbf{v} = 0$, we have that $\mathbf{v} + \mathbf{J}$ is divergence-free. This changes some aspects of the derivation of the Navier-Stokes equations undertaken in chapter 2, where the usual continuity equation was used to help simplify the equations. The full Navier-Stokes and conservation equations derived here are given in the next section.

Our velocity \mathbf{v} is not solenoidal, however in other studies using the shear-induced migration model, the velocity has been assumed to be solenoidal. Phillips et al. (1992) and Murisic et al. (2013) required that the velocity \mathbf{v} be divergence-free, and an equation equivalent to equation (5.1.11) was given. Lee et al. (2014) gave two conservation equations equivalent to those we have derived above, and also required \mathbf{v} to be divergence-free. Thus two equations were added to the clear-fluid model, but only one variable (the particle volume fraction ϕ), implying that the system of governing equations obtained was overdetermined. The model was only self-consistent if $\nabla \cdot \mathbf{J} = 0$, which is not necessarily true. This is an important difference between these previous models and that presented here.

5.2 Governing equations for particle-laden flow in a helical channel

We now express the model equations given in the previous sections in our helicoidal coordinate system defined in chapter 2. As previously, we consider steady, helically-symmetric flow, and so quantities are independent of the angular coordinate β and time. Recall the components of $\mathbf{v} = (v^r, v^\beta, v^z)$, and similarly, the components of the particle flux vector are $\mathbf{J} = (J^r, 0, J^z)$. There is no J^β component because it would come from a derivative with respect to β , and is therefore zero by helical symmetry. Equation (5.1.10) is,

$$\frac{\partial v^r}{\partial r} + \frac{\partial v^z}{\partial z} + \frac{v^r}{r} + \frac{\partial J^r}{\partial r} + \frac{\partial J^z}{\partial z} + \frac{J^r}{r} = 0, \quad (5.2.1)$$

and equation (5.1.11) is,

$$v^r \frac{\partial \phi}{\partial r} + v^z \frac{\partial \phi}{\partial z} + (\phi - 1) \left(\frac{\partial v^r}{\partial r} + \frac{\partial v^z}{\partial z} + \frac{v^r}{r} \right) = 0. \quad (5.2.2)$$

Expressions for the differential operators appearing in equation (5.1.4) were found in section 2.2 for the constant viscosity and density case, and there are two significant changes. Firstly, we cannot use $\nabla \cdot \mathbf{v} = 0$ to simplify the divergence of the rate of strain tensor, and secondly, there are new terms arising from $\nabla \mu \cdot \mathcal{S}$, which is now non-zero. The extra term $\nabla \mu \cdot \mathcal{S}$ is expressed as $\mu_{,i} S^{ij} \mathbf{g}_j$, so we can now write the Navier-Stokes equations as, in the radial direction,

$$\begin{aligned} & \rho \left[v^r \frac{\partial v^r}{\partial r} + v^z \frac{\partial v^r}{\partial z} - r v^\beta v^\beta \right] \\ &= -\frac{\partial p}{\partial r} + H'(r) \frac{\partial p}{\partial z} + \mu \left[2 \frac{\partial^2 v^r}{\partial r^2} + \frac{2}{r} \frac{\partial v^r}{\partial r} - \left\{ \frac{2}{r} H'(r) + H''(r) \right\} \frac{\partial v^r}{\partial z} \right. \\ & \quad \left. - 3 H'(r) \frac{\partial^2 v^r}{\partial z \partial r} + \frac{\partial^2 v^z}{\partial r \partial z} + \Phi \frac{\partial^2 v^r}{\partial z^2} - H'(r) \frac{\partial^2 v^z}{\partial z^2} + \frac{2P}{r} \frac{\partial v^\beta}{\partial z} - \frac{2}{r^2} v^r \right] \\ & \quad + \frac{\partial \mu}{\partial r} \left(2 \frac{\partial v^r}{\partial r} - 2 H'(r) \frac{\partial v^r}{\partial z} \right) \\ & \quad + \frac{\partial \mu}{\partial z} \left(-H'(r) \frac{\partial v^r}{\partial r} + \Phi \frac{\partial v^r}{\partial z} + \frac{\partial v^z}{\partial r} - H'(r) \frac{\partial v^z}{\partial z} + H''(r) v^r \right), \quad (5.2.3a) \end{aligned}$$

in the axial direction,

$$\begin{aligned}
 & \rho \left[v^r \frac{\partial v^\beta}{\partial r} + v^z \frac{\partial v^\beta}{\partial z} + \frac{2}{r} v^r v^\beta \right] \\
 &= \frac{P}{r^2} \frac{\partial p}{\partial z} + \mu \left[\frac{\partial^2 v^\beta}{\partial r^2} - \left\{ H''(r) + \frac{3}{r} H'(r) \right\} \frac{\partial v^\beta}{\partial z} - 2H'(r) \frac{\partial^2 v^\beta}{\partial z \partial r} \right. \\
 & \quad \left. - \frac{P}{r^2} \frac{\partial^2 v^r}{\partial z \partial r} + \frac{2P}{r^3} \frac{\partial v^r}{\partial z} - \frac{P}{r^2} \frac{\partial^2 v^z}{\partial z^2} + \Phi \frac{\partial^2 v^\beta}{\partial z^2} - \frac{2P}{r^3} \frac{\partial v^r}{\partial z} + \frac{3}{r} \frac{\partial v^\beta}{\partial r} - \frac{3P}{r^3} \frac{\partial v^r}{\partial z} \right] \\
 & \quad + \frac{\partial \mu}{\partial r} \left(\frac{\partial v^\beta}{\partial r} - H'(r) \frac{\partial v^\beta}{\partial z} - \frac{P}{r^2} \frac{\partial v^r}{\partial z} \right) \\
 & \quad + \frac{\partial \mu}{\partial z} \left(-H'(r) \frac{\partial v^\beta}{\partial r} + \Phi \frac{\partial v^\beta}{\partial z} - \frac{2P}{r^3} v^r - \frac{P}{r^2} \frac{\partial v^z}{\partial z} \right), \tag{5.2.3b}
 \end{aligned}$$

and in the vertical direction,

$$\begin{aligned}
 & \rho \left[v^r \frac{\partial v^z}{\partial r} + v^z \frac{\partial v^z}{\partial z} + rH'(r)v^\beta v^\beta + H''(r)v^r v^r - \frac{2P}{r} v^\beta v^r \right] \\
 &= H'(r) \frac{\partial p}{\partial r} - \Phi \frac{\partial p}{\partial z} + \mu \left[\left\{ 2H''(r) - \frac{H'(r)}{r} \right\} \frac{\partial v^r}{\partial r} - H'(r) \frac{\partial^2 v^r}{\partial r^2} + \Phi \frac{\partial^2 v^r}{\partial z \partial r} \right. \\
 & \quad + \left\{ H'''(r) + \frac{H''(r)}{r} + \frac{2H'(r)}{r^2} \right\} v^r + \left\{ \frac{2P^2}{r^3} + \frac{\Phi}{r} - 2H''(r)H'(r) \right\} \frac{\partial v^r}{\partial z} \\
 & \quad + \frac{\partial^2 v^z}{\partial r^2} - \left\{ H''(r) + \frac{H'(r)}{r} \right\} \frac{\partial v^z}{\partial z} - 3H'(r) \frac{\partial^2 v^z}{\partial z \partial r} + 2\Phi \frac{\partial^2 v^z}{\partial z^2} + \frac{1}{r} \frac{\partial v^z}{\partial r} - \frac{2P}{r} \frac{\partial v^\beta}{\partial r} \Big] \\
 & \quad + \frac{\partial \mu}{\partial r} \left(-H'(r) \frac{\partial v^r}{\partial r} + \Phi \frac{\partial v^r}{\partial z} + \frac{\partial v^z}{\partial r} - H'(r) \frac{\partial v^z}{\partial z} + H''(r)v^r \right) \\
 & \quad + \frac{\partial \mu}{\partial z} \left(\frac{2P^2}{r^3} v^r + 2\Phi \frac{\partial v^z}{\partial z} - 2H'(r) \frac{\partial v^z}{\partial r} - 2H''(r)H'(r)v^r \right) - \rho g. \tag{5.2.3c}
 \end{aligned}$$

The no-slip and kinematic boundary conditions are unchanged from section 2.3.7. We have no-slip on the channel bottom,

$$v^r = v^\beta = v^z = 0, \quad \text{at } z = 0. \tag{5.2.4}$$

The free surface can be written as the solution to $F(r, z) = 0$, and a normal to the free-surface is given by $\mathbf{n} = \nabla F = (F_{,r}, 0, F_{,z})$. The no-stress condition

at the free-surface gives,

$$0 = F_{,r} \left(2\mu \frac{\partial v^r}{\partial r} - 2\mu H'(r) \frac{\partial v^r}{\partial z} - p \right) + F_{,z} \left(\mu \left[-H'(r) \frac{\partial v^r}{\partial r} + \frac{\partial v^z}{\partial r} + \Phi \frac{\partial v^r}{\partial z} - H'(r) \frac{\partial v^z}{\partial z} + H''(r) v^r \right] + H'(r) p \right), \quad (5.2.5a)$$

$$0 = \mu F_{,r} \left(\frac{\partial v^\beta}{\partial r} - H'(r) \frac{\partial v^\beta}{\partial z} - \frac{\Lambda}{r} \frac{\partial v^r}{\partial z} \right) + F_{,z} \left(\mu \left[-H'(r) \frac{\partial v^\beta}{\partial z} + \Phi \frac{\partial v^\beta}{\partial z} - \frac{2\Lambda}{r^2} v^r - \frac{\Lambda}{r} \frac{\partial v^z}{\partial z} \right] + \frac{\Lambda}{r} p \right), \quad (5.2.5b)$$

$$0 = F_{,r} \left(\mu \left[-H'(r) \frac{\partial v^r}{\partial r} + \frac{\partial v^z}{\partial r} + \Phi \frac{\partial v^r}{\partial z} - H'(r) \frac{\partial v^z}{\partial z} + H''(r) v^r \right] + H'(r) p \right) + F_{,z} \left(\mu \left[\frac{2\Lambda^2}{r} v^r + 2\Phi \frac{\partial v^z}{\partial z} - 2H'(r) \frac{\partial v^z}{\partial r} - 2H''(r) H'(r) v^r \right] - \Phi p \right). \quad (5.2.5c)$$

The kinematic condition is $\mathbf{v} \cdot \mathbf{n} = 0$ at the free surface $F(r, z) = 0$, and gives

$$v^r F_{,r} + v^z F_{,z} = 0. \quad (5.2.6)$$

These equations are complex, and so, as in previous chapters, we will exploit the geometry of the flow to simplify them.

5.3 Thin-film equations

We begin by nondimensionalising our equations using the same scalings as in chapter 4, along with additional scalings for the components of the particle flux vector and the fluid density and viscosity, ρ and μ , which are now

dependent on the particle volume fraction ϕ ,

$$\begin{aligned} \left(\hat{r}, \hat{\beta}, \hat{z} \right) &= \left(\frac{r}{a}, \delta\beta, \frac{z}{a\delta} \right), \quad \left(\hat{v}, \hat{u}, \hat{w} \right) = \left(\frac{v^r}{U\delta}, \frac{v^\beta}{U}, \frac{v^z}{U\delta^2} \right), \\ \left(\hat{j}^y, \hat{j}^\beta, \hat{j}^z \right) &= \frac{a^2\delta^2}{d^2U} \left(\frac{J^r}{\delta}, 0, J^z \right), \quad \hat{p} = \frac{a\delta}{U\mu_f} p, \\ \hat{\mu}(\phi) &= \frac{\mu(\phi)}{\mu_f}, \quad \hat{\rho}(\phi) = \frac{\rho(\phi)}{\rho_f} = \rho_s\phi + 1, \quad \hat{y} = \frac{r - A}{a}, \end{aligned} \quad (5.3.1)$$

where $\rho_s = (\rho_p - \rho_f)/\rho_f$ is the density difference between particles and fluid, relative to the fluid density. The Reynolds and Froude numbers are defined as,

$$\text{Re} = \frac{\rho_f U a \delta}{\mu_f}, \quad \text{Fr} = \frac{U}{\sqrt{g a \delta}}, \quad (5.3.2)$$

and they are specified as in equation (4.2.12),

$$\frac{\text{Re}}{\text{Fr}^2} \frac{\lambda}{(1 + \lambda^2)^{3/2}} = 1 \quad \text{and} \quad \frac{6}{35} \text{Re} \frac{\epsilon \lambda}{(1 + \lambda^2)^{3/2}} = 1. \quad (5.3.3)$$

We can use the first of these, along with the definition of the Reynolds and Froude numbers to give an equation for the axial velocity scale U ,

$$U = \frac{\lambda}{(1 + \lambda^2)^{3/2}} \frac{(a\delta)^2 g \rho_f}{\mu_f}. \quad (5.3.4)$$

The scaling of the particle flux vector includes the particle diameter d , which must be small, but we need to compare it to the fluid depth scaling, δ , in order to compare terms in the perturbation expansions of the governing equations. Previously we stated the requirement $d \ll a\delta$ so that the particles are small relative to the fluid depth, justifying the continuum modelling approach. If the particles are too small, however, Brownian diffusion becomes a dominant effect and settling due to gravity is negligible. To ensure this does not occur, and as in Lee et al. (2014) and Murisic et al. (2013), we want the settling distance along the channel, L_{settle} , of the particles to be small relative to the axial length scale of the channel. We assume that the channel is much longer than it is wide, and set the axial length scale as a/δ . Considering

5. Particle-laden flow in shallow channels

the film thickness, settling velocity, and axial velocity scales in the spirit of equation (2.3) in Murisic et al. (2013), we obtain,

$$\begin{aligned} L_{settle} &\approx \frac{\text{fluid depth}}{\text{settling velocity}} \times \text{axial velocity} \\ &\approx \frac{a\delta}{\frac{d^2 g(\rho_p - \rho_f)}{18\mu_f}} \frac{\rho_f g(a\delta)^2 \lambda}{\mu_f (1 + \lambda^2)^{3/2}} = \frac{(a\delta)^3}{d^2} \frac{18\rho_f \lambda}{(\rho_p - \rho_f)(1 + \lambda^2)^{3/2}}, \end{aligned} \quad (5.3.5)$$

For this settling length to be small relative to the axial length scale, we require

$$\frac{(a\delta)^3}{d^2} \ll \frac{a}{\delta}, \quad (5.3.6)$$

or $(d/a)^2 \gg \delta^4$. Combining this with the condition $d \ll a\delta$, we obtain,

$$\delta^4 \ll \left(\frac{d}{a}\right)^2 \ll \delta^2, \quad (5.3.7)$$

asymptotically as $\delta \rightarrow 0$, and so we set $(d/a)^2 = O(\delta^3)$ when comparing terms in the asymptotic expansions of the governing equations.

Using Maple we obtain the following system of equations at leading order in δ , where we have omitted the carets as all variables and parameters are nondimensional. The Navier-Stokes equations yield,

$$\frac{\partial}{\partial z} \left(\mu \frac{\partial v}{\partial z} \right) = -\frac{\text{Re} \epsilon \rho}{(1 + \epsilon y) \Upsilon^2} u^2 + \frac{1}{\Upsilon} \frac{\partial p}{\partial y} - \frac{1}{\Upsilon} \frac{dH}{dy} \frac{\partial p}{\partial z} - \frac{2\mu\epsilon\Lambda}{(1 + \epsilon y) \Upsilon^{3/2}} \frac{\partial u}{\partial z}, \quad (5.3.8a)$$

$$\frac{\partial}{\partial z} \left(\mu \frac{\partial u}{\partial z} \right) = \frac{\text{Re}}{\text{Fr}^2} \frac{\rho \Lambda}{\Upsilon^{3/2}}, \quad (5.3.8b)$$

$$\frac{\partial p}{\partial z} = -\frac{\text{Re}}{\text{Fr}^2} \frac{\rho}{\Upsilon}, \quad (5.3.8c)$$

the conservation equations (5.2.1) and (5.2.2) give,

$$\frac{\partial J^z}{\partial z} = 0, \quad (5.3.9)$$

$$v \frac{\partial \phi}{\partial r} + w \frac{\partial \phi}{\partial z} = (1 - \phi) \left(\frac{\partial v}{\partial r} + \frac{\partial u}{\partial z} + \frac{v}{r} \right), \quad (5.3.10)$$

and the boundary conditions give,

$$u = v = w = 0 \quad \text{at } z = 0, \quad (5.3.11)$$

$$p = 0, \quad \frac{\partial v}{\partial z} = 0, \quad \frac{\partial u}{\partial z} = 0, \quad w = \frac{dh}{dy}v, \quad \text{at } z = h(y), \quad (5.3.12)$$

$$J^z = 0, \quad \text{at } z = 0. \quad (5.3.13)$$

Although these equations are significantly simplified compared to the full Navier-Stokes equations, they cannot be solved analytically as, in general, the particle volume fraction will vary in both the y and z directions, and hence μ and ρ are functions of both y and z .

5.4 The thin-film solution for $\phi = \phi(y)$

Experimental work by Zhou et al. (2005), Murisic et al. (2011) and others on particle-laden thin film flows on inclined planes found three qualitatively different behaviours depending on the angle of inclination and initial particle volume fraction. The three regimes are termed settled, well-mixed, and ridged. In the settled regime, particles tend to settle quickly and clear fluid flows more quickly over the top of the particles. In the ridged regime, particles move more quickly than the surrounding fluid, and form a layer at the surface. Finally, in the well-mixed regime, the fluid and particle velocities are roughly the same, and the particles do not tend to congregate at the bottom or top of the fluid, but disperse uniformly throughout the film thickness.

In Lee et al. (2014), it was found that the only solutions that their thin-film governing equations could admit were of the well-mixed type. However, as discussed in section 5.1.1, we believe their system of equations was over-determined, and unnecessarily constrained the particle volume fraction ϕ to be independent of depth. For our model, this restriction need not necessarily apply. Nevertheless, motivated by the existence of well-mixed flows down inclined planes, we here seek solutions in helically-wound channels in the well-mixed regime, by assuming $\phi = \phi(y)$ so that the particle volume-fraction is independent of depth. We ask whether solutions exist, and if so, what they look like and if they differ significantly from those found by Lee

5. Particle-laden flow in shallow channels

et al. (2014) for channels of small slope. This has the benefit of making the governing equations significantly more tractable, enabling further analytic progress. The more general case where the particle volume-fraction varies with both depth and radial position is left for future work.

With $\phi = \phi(y)$, both the density and viscosity become functions of y only, and this allows the thin-film governing equations to be solved by sequential integration. Equation (5.3.8c) can be solved directly to give

$$p = -\frac{\text{Re}}{\text{Fr}^2} \frac{\rho}{\Upsilon} (z - h(y)), \quad (5.4.1)$$

and equation (5.3.8b) gives

$$u = \frac{\text{Re}}{\text{Fr}^2} \frac{\rho \Lambda}{\mu \Upsilon^{3/2}} \frac{z}{2} (z - 2h(y)). \quad (5.4.2)$$

Now equation (5.3.9) can be integrated with respect to z to give $J^z = C(y)$ for some $C(y)$, and the boundary condition $J^z|_{z=0} = 0$ gives $J^z = 0$, so gravitational settling is balanced by shear-induced migration. Writing the z -component of the particle flux vector explicitly gives an equation involving ϕ , μ , and $u_{,z}$,

$$0 = -\frac{\text{Re}}{\text{Fr}^2} \frac{d^2 \phi \rho_s}{18\mu} \omega(\phi) + \frac{K_c d^2}{4} \phi (u_{,z} \phi)_{,z} + \frac{K_v d^2}{4} \frac{\phi^2 u_{,z}}{\mu} \frac{d\mu}{d\phi} \phi_{,z}, \quad (5.4.3)$$

which can be rearranged as

$$\frac{2\rho_s \text{Re}}{9\text{Fr}^2 K_c} \omega(\phi) - \phi (\mu u_{,z})_{,z} - \left[1 + 2 \frac{K_v - K_c}{K_c} \frac{\phi}{\phi_m - \phi} \right] \phi_{,z} (\mu u_{,z}) = 0. \quad (5.4.4)$$

Now $\phi_{,z} = 0$ by assumption, and we can use (5.3.8b) to replace $\mu u_{,z}$, so that

$$\frac{2\rho_s \text{Re}}{9\text{Fr}^2 K_c} \omega(\phi) - \frac{\text{Re}}{\text{Fr}^2} \frac{\rho \Lambda \phi}{\Upsilon^{3/2}} = 0. \quad (5.4.5)$$

Given the hindrance function $\omega(\phi) = 1 - \phi$, this gives,

$$\frac{2\Upsilon^{3/2} \rho_s}{9\Lambda K_c} (1 - \phi) - \phi (1 + \rho_s \phi) = 0, \quad (5.4.6)$$

which gives a quadratic equation for $\phi(y)$,

$$\phi^2 + \left(\frac{1}{\rho_s} + \frac{2\Upsilon^{3/2}}{9\Lambda K_c} \right) \phi - \frac{2\Upsilon^{3/2}}{9\Lambda K_c} = 0, \quad (5.4.7)$$

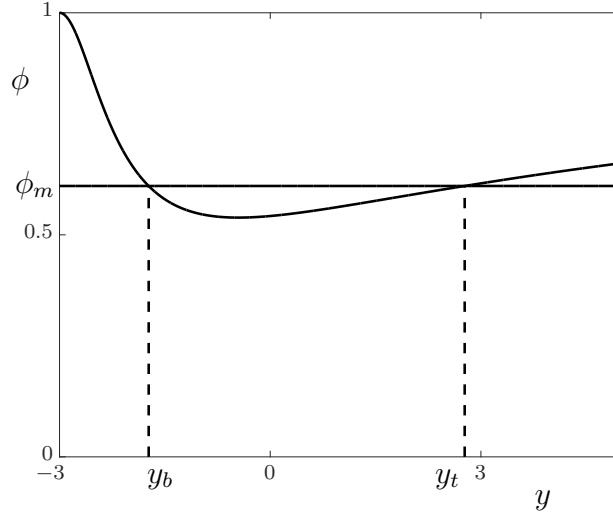


Figure 5.1: Particle volume fraction for a channel with $\lambda = 0.6$, $\epsilon = 1/3$, $\rho_s = 1.5$, and $\phi_m = 0.61$.

with solution

$$\phi = - \left(\frac{\Upsilon^{3/2}}{9\Lambda K_c} + \frac{1}{2\rho_s} \right) + \sqrt{\left(\frac{\Upsilon^{3/2}}{9\Lambda K_c} + \frac{1}{2\rho_s} \right)^2 + \frac{2\Upsilon^{3/2}}{9\Lambda K_c}}. \quad (5.4.8)$$

Note that the particle volume fraction given in equation (5.4.8) is a function of $\Lambda(y)$, (the slope of the channel bottom) and must also satisfy $0 \leq \phi < \phi_m = 0.61$ in the particle-rich region in order for our model to be valid. Figure 5.1 shows a typical profile for ϕ . Note that $\phi(y) \rightarrow 1$ as $y \rightarrow \infty$ and $y \rightarrow -1/\epsilon^+$, and takes a minimum value at $y = (\sqrt{2}\lambda - 1)/\epsilon$, where $\Lambda = 1/\sqrt{2}$. For $\rho_s > 3.45$, the minimum value of $\phi(y)$ is larger than ϕ_m , which limits the density of the particles to be below this limit.

To have $\phi(y) < \phi_m$ everywhere in the channel, we must have the channel fully within $[y_b, y_t]$, the end-points of which satisfy $\phi(y) = \phi_m$, and can be calculated numerically. This restricts our choice of channel centreline geometry, and will be discussed further in section 5.5. Significantly, the particle volume fraction (5.4.8) is not a monotonic increasing function of y , as it was in Lee et al. (2014) due to their small-slope assumption.

5. Particle-laden flow in shallow channels

Having determined ϕ , we next find the radial velocity, v , by integrating equation (5.3.8a) twice. Rearranging and substituting for u and p gives,

$$\begin{aligned} \frac{\partial^2 v}{\partial z^2} = & - \frac{\text{Re}^3 \epsilon \rho^3 \Lambda^2}{\text{Fr}^4 (1 + \epsilon y) \mu^3 \Upsilon^5} \frac{z^2 (z - 2h(y))^2}{4} \\ & + \left(- \frac{\text{Re}}{\text{Fr}^2} \frac{1}{\mu \Upsilon^2} \frac{d\rho}{dy} - \frac{\text{Re}}{\text{Fr}^2} \frac{4\epsilon \rho \Lambda^2}{(1 + \epsilon y) \mu \Upsilon^3} \right) (z - h) \\ & + \frac{\text{Re}}{\text{Fr}^2} \frac{\rho}{\mu \Upsilon^2} \left(\frac{dH}{dy} + \frac{dh}{dy} \right), \end{aligned} \quad (5.4.9)$$

and hence,

$$\begin{aligned} v = & - \frac{\text{Re}^3 \epsilon \rho^3 \Lambda^2}{\text{Fr}^4 (1 + \epsilon y) \mu^3 \Upsilon^5} \frac{z}{120} (z^5 - 6hz^4 + 10h^2z^3 - 16h^5) + \\ & \left(- \frac{\text{Re}}{\text{Fr}^2} \frac{1}{\mu \Upsilon^2} \frac{d\rho}{dy} - \frac{\text{Re}}{\text{Fr}^2} \frac{4\epsilon \rho \Lambda^2}{(1 + \epsilon y) \mu \Upsilon^3} \right) \frac{(z - h)^3 + h^3}{6} \\ & + \frac{\text{Re}}{\text{Fr}^2} \frac{\rho}{\mu \Upsilon^2} \left(\frac{dH}{dy} + \frac{dh}{dy} \right) \frac{z(z - 2h)}{2}. \end{aligned} \quad (5.4.10)$$

Equation (5.3.10) can be written as,

$$\frac{\partial}{\partial y} \left(\frac{(1 - \phi)(1 + \epsilon y)v}{\epsilon} \right) + \frac{\partial}{\partial z} \left(\frac{(1 - \phi)(1 + \epsilon y)w}{\epsilon} \right) = 0, \quad (5.4.11)$$

and integrated with respect to z and rearranged using Leibniz's integral rule to give,

$$\begin{aligned} \frac{\partial}{\partial y} \int_0^{h(y)} \frac{(1 - \phi)(1 + \epsilon y)v}{\epsilon} dz - \left[\frac{(1 - \phi)(1 + \epsilon y)v}{\epsilon} \right]_{z=h(y)} \frac{dh}{dy} \\ + \left[\frac{(1 - \phi)(1 + \epsilon y)w}{\epsilon} \right]_{z=0}^{h(y)} = 0. \end{aligned} \quad (5.4.12)$$

Using the kinematic and no-slip boundary conditions gives

$$\frac{\partial}{\partial y} \int_0^{h(y)} \frac{(1 - \phi)(1 + \epsilon y)v}{\epsilon} dz = 0, \quad (5.4.13)$$

which can be integrated to yield

$$\frac{(1 - \phi)(1 + \epsilon y)}{\epsilon} \int_0^{h(y)} v dz = C, \quad (5.4.14)$$

where C is a constant which effectively controls the net radial flow at any position y . We set $C = 0$ so that there is no net flow into or out of the fluid domain, to obtain,

$$\int_0^{h(y)} v \, dz = 0. \quad (5.4.15)$$

Substituting v into this integral equation gives

$$\begin{aligned} 0 = & \int_0^{h(y)} -\frac{\text{Re}^3 \epsilon \rho^3 \Lambda^2}{\text{Fr}^4 (1 + \epsilon y) \mu^3 \Upsilon^5} \frac{z}{120} (z^5 - 6hz^4 + 10h^2z^3 - 16h^5) + \\ & \left(-\frac{\text{Re}}{\text{Fr}^2} \frac{1}{\mu \Upsilon^2} \frac{d\rho}{dy} - \frac{\text{Re}}{\text{Fr}^2} \frac{4\epsilon \rho \Lambda^2}{(1 + \epsilon y) \mu \Upsilon^3} \right) \frac{(z - h)^3 + h^3}{6} \\ & + \frac{\text{Re}}{\text{Fr}^2} \frac{\rho}{\mu \Upsilon^2} \left(\frac{dH}{dy} + \frac{dh}{dy} \right) \frac{z(z - 2h)}{2} dz, \end{aligned} \quad (5.4.16)$$

and on integrating we find

$$\begin{aligned} 0 = & -\frac{\text{Re}^3 \epsilon \rho^3 \Lambda^2}{\text{Fr}^4 (1 + \epsilon y) \mu^3 \Upsilon^5} \left[\frac{z^2}{840} (z^5 - 7hz^4 + 14h^2z^3 - 56h^5) \right]_{z=0}^h \\ & + \left(-\frac{\text{Re}}{\text{Fr}^2} \frac{1}{\mu \Upsilon^2} \frac{d\rho}{dy} - \frac{\text{Re}}{\text{Fr}^2} \frac{4\epsilon \rho \Lambda^2}{(1 + \epsilon y) \mu \Upsilon^3} \right) \left[\frac{z^2}{24} (z^2 - 4hz + 6h^2) \right]_{z=0}^h \\ & + \frac{\text{Re}}{\text{Fr}^2} \frac{\rho}{\mu \Upsilon^2} \left(\frac{dH}{dy} + \frac{dh}{dy} \right) \left[\frac{z^2}{6} (z - 3h) \right]_{z=0}^h, \end{aligned} \quad (5.4.17)$$

and hence,

$$\begin{aligned} 0 = & \frac{48h^7}{840} \frac{\text{Re}^3 \epsilon \rho^3 \Lambda^2}{\text{Fr}^4 (1 + \epsilon y) \mu^3 \Upsilon^5} + \frac{h^4}{8} \left(-\frac{\text{Re}}{\text{Fr}^2} \frac{1}{\mu \Upsilon^2} \frac{d\rho}{dy} - \frac{\text{Re}}{\text{Fr}^2} \frac{4\epsilon \rho \Lambda^2}{(1 + \epsilon y) \mu \Upsilon^3} \right) \\ & - \frac{h^3}{3} \frac{\text{Re}}{\text{Fr}^2} \frac{\rho}{\mu \Upsilon^2} \left(\frac{dH}{dy} + \frac{dh}{dy} \right). \end{aligned} \quad (5.4.18)$$

Rearranging for the fluid depth $h(y)$, we finally obtain

$$\frac{dh}{dy} = \frac{6}{35} \frac{\text{Re}^2}{\text{Fr}^2} \frac{\epsilon \rho^2 \Lambda^2}{(1 + \epsilon y) \mu^2 \Upsilon^3} h^4 - \frac{3}{2} \frac{\Lambda^2 \epsilon}{\Upsilon (1 + \epsilon y)} h - \frac{3}{8} \frac{1}{\rho} \frac{\partial \rho}{\partial y} h - \frac{dH}{dy}. \quad (5.4.19)$$

This equation differs from the clear-fluid free-surface equation (4.2.5) in having an extra term, linear in h , involving the gradient of the density. As a Chini differential equation, this equation has no analytic solution in general. In the rectangular channel case $H = 0$, the equivalent clear-fluid equation (4.2.5)

5. Particle-laden flow in shallow channels

did have an analytic solution, but equation (5.4.19) does not, due to the presence of the additional term involving the density gradient.

Substituting the free surface equation into v gives,

$$v = -\frac{\text{Re}^3}{\text{Fr}^4} \frac{\epsilon \rho^3 \Lambda^2}{(1 + \epsilon y) \mu^3 \Upsilon^5} \frac{z(z - 2h) [7z(z - 2h)(z - 2hz - 2h^2) - 16h^4]}{840} - \frac{\text{Re}}{\text{Fr}^2} \frac{1}{\mu \Upsilon^2} \left(\frac{d\rho}{dy} + \frac{4\epsilon \rho \Lambda^2}{(1 + \epsilon y) \Upsilon} \right) \frac{z(8z^2 - 15hz + 6h^2)}{48}. \quad (5.4.20)$$

A streamfunction is defined by,

$$\frac{\partial \psi}{\partial z} = (1 + \epsilon y)(1 - \phi)v, \quad \frac{\partial \psi}{\partial y} = -(1 + \epsilon y)(1 - \phi)w, \quad (5.4.21)$$

and, using (5.4.20) and requiring $\psi = 0$ on the channel bottom $z = 0$, we find,

$$\psi = -\frac{\text{Re}}{\text{Fr}^2} \frac{1 - \phi}{\mu \Upsilon^2} \left[\frac{\text{Re}^2}{\text{Fr}^2} \frac{\epsilon \rho^3 \Lambda^2}{\mu^2 \Upsilon^3} \frac{z^2(z - h)(z - 2h)^2(z^2 - 2hz - 4h^2)}{840} + \left((1 + \epsilon y) \frac{d\rho}{dy} + \frac{4\epsilon \rho \Lambda^2}{\Upsilon} \right) \frac{z^2(2z - 3h)(z - h)}{48} \right]. \quad (5.4.22)$$

The second equation in (5.4.21) can be used to find the vertical velocity w (not given due to its complexity).

As we are now dealing with particle-laden flow, there are two fluxes that are relevant, the total mixture flux and the flux of particles. The total flux down the channel Q (scaled by $\delta a^2 U$) is given, as in previous chapters, by

$$Q = -\int_{y_l}^{y_r} \int_0^{h(y)} u(z, y) dz dy = \frac{1}{3} \frac{\text{Re}}{\text{Fr}^2} \int_{y_l}^{y_r} \frac{\rho \Lambda h^3}{\mu \Upsilon^{3/2}} dy, \quad (5.4.23)$$

where y_l and y_r represent the inner and outer extents of the fluid domain. The particle flux Q_p (scaled by $\delta a^2 U$) can be written as

$$Q_p = -\int_{y_l^*}^{y_r^*} \int_0^{h(y)} \phi(y) u(z, y) dz dy = \frac{1}{3} \frac{\text{Re}}{\text{Fr}^2} \int_{y_l^*}^{y_r^*} \frac{\rho \phi \Lambda h^3}{\mu \Upsilon^{3/2}} dy. \quad (5.4.24)$$

where y_l^* and y_r^* represent the extents of the particle-rich region of the flow, which do not necessarily correspond to the whole fluid domain. The particle-rich region must be contained in the fluid region, so we must have $y_l \leq y_l^* < y_r^* \leq y_r$. The negative signs in the two fluxes given above are due to the axial coordinate direction pointing up the channel, meaning u is always negative.

5.5 Results

Having obtained a solution to the thin-film system of equations under the assumption that particles are uniformly dispersed in the vertical direction, we now present and discuss some particular cases. In section 4.2.1, we discussed how a solution was obtained for particle-free flow in an arbitrarily-shaped channel. In this chapter, we have introduced one more variable, the particle volume fraction, and for a chosen channel geometry expanded the set of parameters to $\{y_l, h_l, y_r, h_r, Q, y_l^*, y_r^*, Q_p\}$, where the last three are new. Of these new parameters, we must specify two. We will choose to specify the flux of particles Q_p and y_l^* , as discussed below.

By considering spiral particle separators, we expect that, in steady state conditions, the particle-rich region of the flow should be near the inside wall of the channel, and extend part or all of the way to the outside channel wall. The volume fraction of particles ϕ is dependent on radial position y , and the quantity of particles together with $\phi(y)$ determines how wide the particle-rich zone will be. Lee et al. (2014) provided an intuitive explanation as to why this configuration of particles is expected to be stable. Their argument also applies here, and we describe it now.

Let us first assume that the particles collect near the inside channel wall, and there is a clear fluid region in the outer region of the channel cross-section. The outward flow near the free surface will carry particles radially outwards into the particle-free region, where, because the particle volume fraction will

be low, they will be in the settled regime, and will rapidly equilibrate to the channel bottom. The equilibration will be fast by the assumption of short settling length. The secondary flow, which is radially inwards near the channel bottom, then carries the particles back into the particle-rich region. So in practice we would expect that if such a configuration of particles was reached, it would remain stable.

Now assume that there is a configuration with a particle-free region near the inside wall and a particle-rich region further outwards. On the boundary between the particle-rich and particle-free regions, the flow near the channel bottom will carry particles into the particle-free region. Again, the particles will tend to be in the settled regime due to the low volume fraction. Thus the particles will stay near the channel bottom, and the secondary flow will continue to carry them to the inside channel wall, and they will not return to the particle-rich region. This configuration of particles is therefore not stable, and over time the particles will collect in a region next to the inside wall of the channel. Thus we search for solutions with the particle-rich region near the inside channel wall and the particle-free region near the outside wall. This means we set $y_i^* = y_i$.

We solve the governing equations separately in the particle-rich and particle-free regions, and couple them by requiring the free-surface be continuous at the boundary between the two regions. At the interface between the particle-rich and particle-free regions of the flow, the fluid properties are discontinuous. In practice we would expect a thin boundary layer between the two regions, which is not captured in our leading order equations. We expect that the effect of this boundary layer would be limited to a region close to the interface, as seen in section 4.3.1 for boundary layers at vertical channel walls.

We will be particularly interested in considering how well a channel can focus the particle-rich region of the flow. For given fluxes of particles and fluid, minimising the size of the particle-rich region is expected to be advantageous,

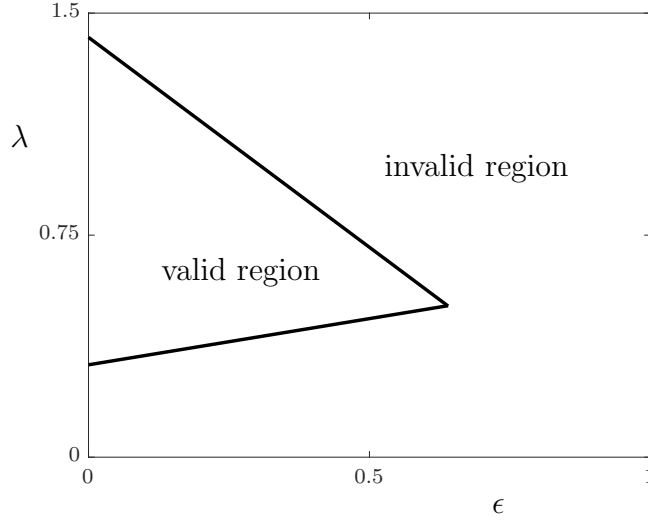


Figure 5.2: Boundary of the region where $\phi(y) < \phi_m$ everywhere in the channel, with $\rho_s = 1.5$. The valid region is the interior of the triangle.

as channels which minimise the size of the particle-rich region for a monodisperse slurry (as considered here) are more likely to segregate the different particles in polydisperse slurries.

Throughout this section, we use dashed streamlines for the particle-laden section of the flow, and solid streamlines for the particle-free fluid. A solid vertical line indicates the boundary between particle-free and particle-rich regions at $y = y_r^*$. In all plots we set $K_c = 0.41$, which has been empirically determined from experiments (Phillips et al., 1992), and $\phi_m = 0.61$ as previously discussed. Unless stated otherwise, we will use $\rho_s = 1.5$.

As previously discussed, the particle volume fraction $\phi(y)$ must satisfy $\phi(y) < \phi_m$ everywhere in the channel for our model to be valid. We have $y_l^* = y_l$, and y_r^* is determined by our choice of Q_p . There is a maximum value of Q_p , which is reached when $y_r^* = y_r$, when the particle-rich region fills the whole fluid domain. Where $\phi(y) > \phi_m$, our model is not valid. Thus we restrict ϵ and λ so that $\phi(y) < \phi_m$ in the solutions we present. Figure 5.2 shows the region in the ϵ - λ plane where $\phi(y) < \phi_m$ for all $-1 \leq y \leq 1$, for $\rho_s = 1.5$.

5.5.1 The effect of centreline geometry

Changing ϵ and λ in particle-free flows has been studied in detail in sections 3.5 and 4.3, and we now seek to understand the effect of ϵ and λ on particle-rich flows.

Figure 5.3 shows the effect of changing ϵ on the resulting flow in a rectangular channel. The total flux and particle flux are the same in each plot, $Q = 0.19$ and $Q_p = 0.001$. The addition of the particle-rich zone causes significant differences from clear-fluid solutions, with the sharp change in the free-surface slope at the interface between the particle-rich and particle-free regions, the separate secondary flow profiles in the two regions, and much lower axial velocity in the particle rich region. Additionally, the streamlines in the particle-rich and particle-free regions are not plotted at the same contour levels, the magnitude of the streamfunction in the particle-free region is larger than the streamfunction in the particle-rich region. We conclude that the flow has divided into two distinct regions with no flow between the two. There are some similarities with the clear-fluid solutions from chapters 3 and 4; increasing ϵ still tends to push the slurry towards the inside of the channel, increasing the depth there and decreasing it at the outside of the channel.

The particle volume fraction $\phi(y)$ is also shown in figure 5.3. In all three cases, the particle-rich region of the flow has a very high volume fraction of particles, near to $\phi_m = 0.61$. The effect of ϵ on the location of the interface between the particle-rich and particle-free regions of the flow (y_r^*) is complex. As ϵ increases, y_r^* initially decreases, but as ϵ increases further, y_r^* starts increasing again. Depending on the slope of the channel centreline λ , we can observe three behaviours, y_r^* decreasing as ϵ increases, y_r^* increasing as ϵ increases, and y_r^* decreasing then increasing as ϵ increases (the case seen in figure 5.3). Figure 5.4 shows the dependence of y_r^* on the channel centreline geometry (ϵ and λ), for a channel with total flux $Q = 0.3$ and particle flux $Q_p = 0.001$. This plot helps to make sense of these three behaviours. We

see that, for fixed ϵ , there can be a decrease in y_r^* as λ increases, followed by an increase in y_r^* as λ increases further. A further useful result that can be seen from this plot is the values of ϵ and λ for which the particle-rich region is smallest. As mentioned earlier, reducing the radial extent of the particle-rich region could potentially be beneficial in spiral particle separators. For $\rho_s = 1.5$, the case considered in figure 5.4, the radial extent of the particle-rich region is minimised when λ and ϵ are both roughly 0.5.

Figure 5.5 shows the effect of changing λ on the resulting flow in a parabolic channel $H(y) = y^2$. The particle flux and total mixture fluxes are the same for all three plots, $Q = 0.05$ and $Q_p = 0.0005$. There is little qualitative difference in the solutions except for the change in the location of the interface between the particle-rich and particle-free regions. Figure 5.6 shows contours of y_r^* , similar to figure 5.4. Not only is the effect of λ relatively minor, but the effect of ϵ is even smaller, with the contour levels nearly horizontal. The difference between the smallest and largest values of y_r^* in the plot is only 0.4, compared to over 0.8 for the rectangular channel considered perviously, so y_r^* is not significantly affected by the channel centreline geometry for parabolic channels. The centreline geometry that minimises the radial extent of the particle rich region is $\epsilon \approx 0.55$ and $\lambda \approx 0.61$, however, the channel cross-section has a more significant impact on the secondary flow and particle volume fraction distribution. The parabolic channel allows less freedom for the secondary flow and free-surface profile to change than in the rectangular channel case. In the next section, we will see whether the channel geometry can be changed in order to reduce the radial extent of the particle-rich region.

5.5.2 The effect of a trench in channel bottom

Motivated by spiral particle separators, which often feature a trench near the inside wall, we consider a rectangular channel with a growing trench. The trench is a quartic polynomial that joins to the flat channel bottom with continuous first derivative, with maximum depth k and half-width b . The

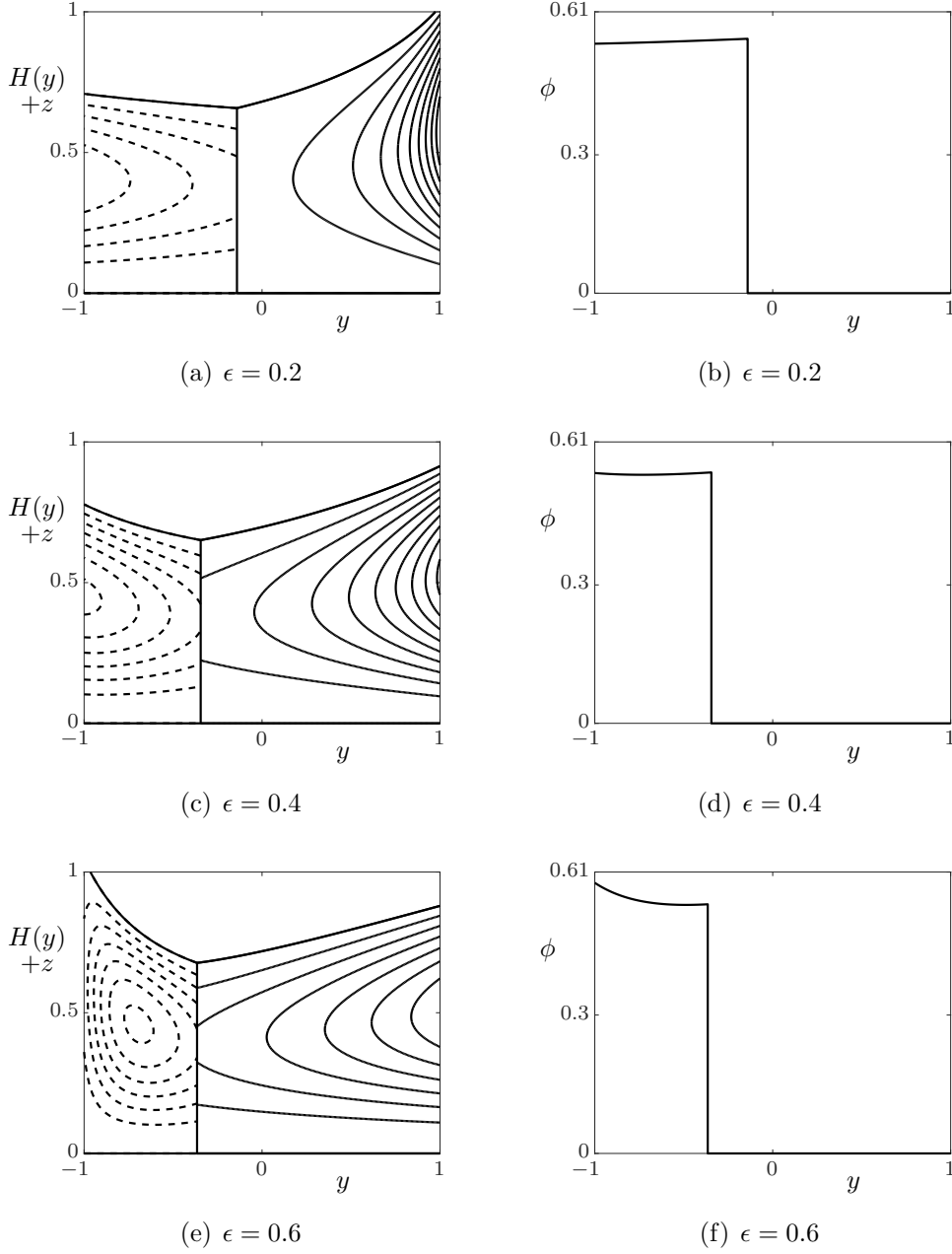


Figure 5.3: Rectangular channels with $\lambda = 0.5$ while varying ϵ , with $Q = 0.3$ and $Q_p = 0.001$. The left column shows free-surface profile and stream-function of the secondary flow in the particle-rich (dashed lines) and particle-free (solid lines) regions. The right column shows the particle volume fraction at each y .

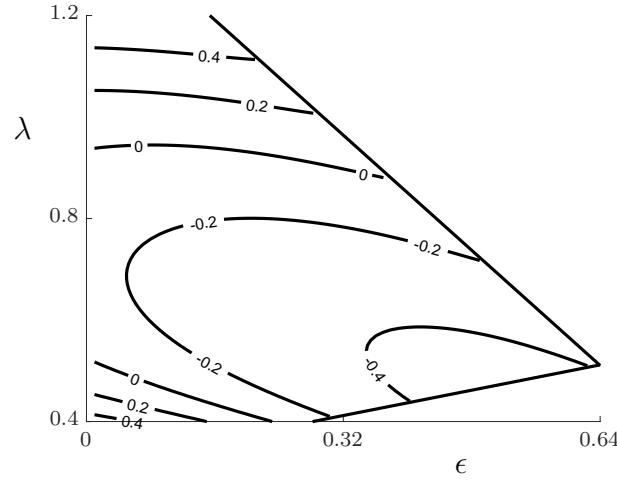
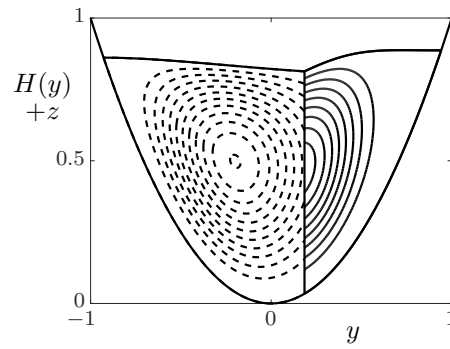


Figure 5.4: Contours of y_r^* for a rectangular channel with $Q = 0.3$, $Q_p = 0.001$. Straight lines show the boundary of the region where $\phi(y) < \phi_m$ everywhere in the channel.

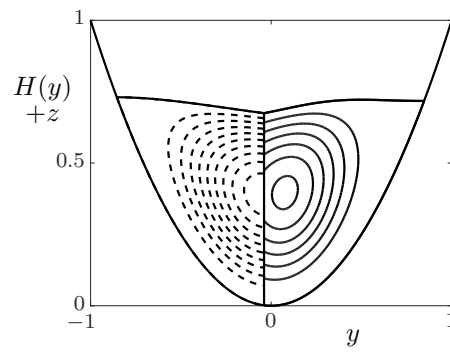
equation of the channel bottom is,

$$H(y) = \begin{cases} -kb^{-4} (y + 1 - 2b)^2 (y + 1)^2, & -1 \leq y \leq -1 + 2b, \\ 0, & -1 + 2b < y \leq 1. \end{cases} \quad (5.5.1)$$

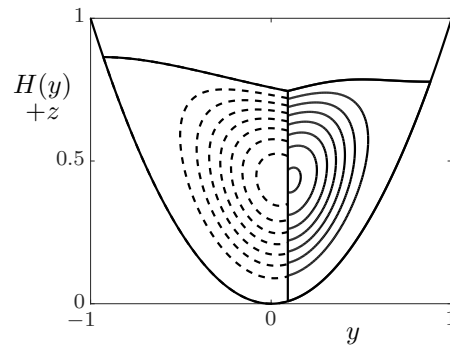
Figure 5.7 shows the results for such a channel with $\epsilon = 0.3$, $\lambda = 0.5$, and $b = 0.3$, $Q = 0.18$, $Q_p = 0.0017$ and a deepening trench (k increasing). The particle-rich region does contract as the trench deepens, and the effect is significant. To capture the particle-rich region of the flow with no trench requires splitting the flow roughly at its centreline, $y = 0$, but with a trench of depth 0.3 and width 0.6, the interface between the particle-rich and particle-free regions is at $y \approx -0.34$. The free-surface profile does not change significantly as the trench depth increases, in line with the conclusions from chapter 4, but the trench means there is more cross-sectional area near the inside wall, and so more particles can fit within a certain distance from the inside wall of the channel. The trench has little effect on the secondary flow in the particle-free region, but does entrain a rotating cell of particle-rich fluid. Whilst we expect boundary layers near the vertical channel walls which would cause all the streamlines to connect up and form closed curves



(a) $\lambda = 0.4$



(b) $\lambda = 0.7$



(c) $\lambda = 1$

Figure 5.5: Parabolic channels $H(y) = y^2$, with $\epsilon = 0.25$ while varying λ , for $Q = 0.05$ and $Q_p = 0.0005$.

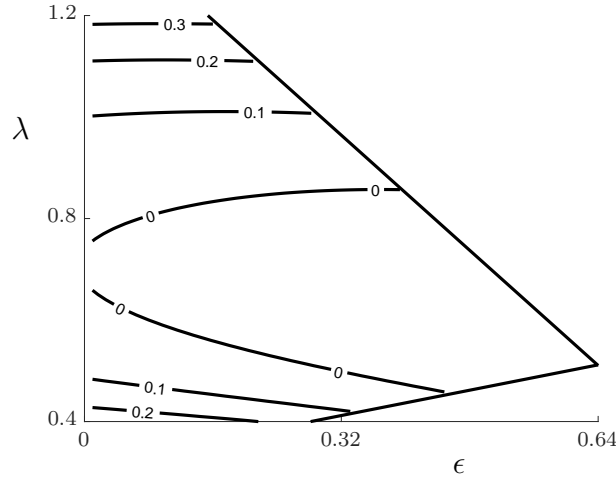
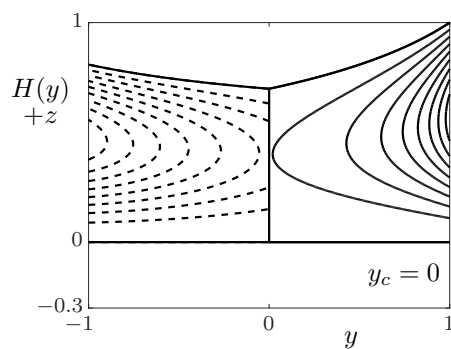


Figure 5.6: Contours of y_r^* for a parabolic channel $H(y) = y^2$, with $Q = 0.05$ and $Q_p = 0.0005$. Straight lines show the boundary of the region where $\phi(y) < \phi_m$ everywhere in the channel.

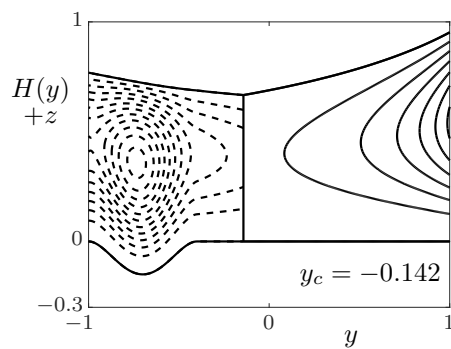
(discussed in detail in section 4.3.1), the trench moves the centre of rotation radially outwards from the inside wall.

5.5.3 The effect of particle density

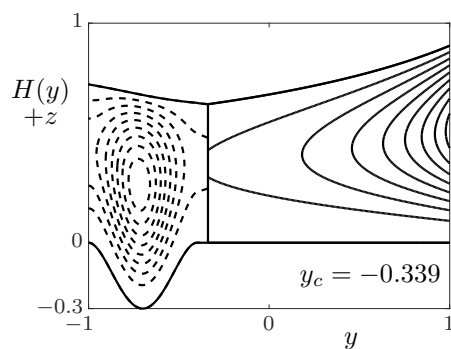
Figure 5.8 shows a rectangular channel, with $\epsilon = 0.2$, $\lambda = 0.7$, $Q = 0.122$ and $Q_p = 0.0007$, carrying particles of increasing density. We first note that ρ_s is not the actual particle density, but is defined in terms of the particle and fluid densities as $\rho_s = (\rho_p - \rho_f)/\rho_f$, and the effective nondimensional mixture density is $\rho = 1 + \phi\rho_s$, so increasing ρ_s increases the density of the particle phase. As the density increases, the size of the particle-rich region increases dramatically. This is not necessarily intuitive; as ρ_s increases we would expect the particles to flow faster down the channel under the influence of gravity. However, the axial flow velocity u (equation (5.4.2)) includes a term ρ/μ which, for $\epsilon = 0.2$ and $\lambda = 0.7$, becomes very small as ρ_s increases, i.e. the viscosity increases more quickly than the density. In fact, for the



(a) $k = 0$



(b) $k = 0.15$



(c) $k = 0.3$

Figure 5.7: Rectangular channels with $\epsilon = 0.3$, $\lambda = 0.5$, $Q = 0.18$ and $Q_p = 0.0017$, with a growing trench (of depth k and half-width $b = 0.3$) near the inside wall.

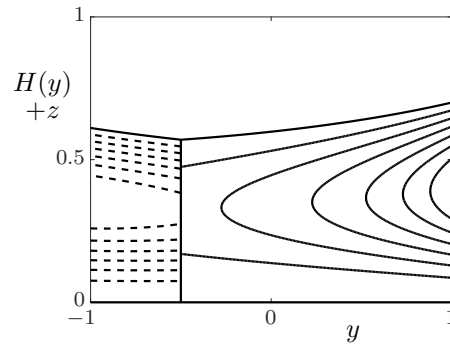
full range of parameters considered in this section (ϵ and λ restricted so that $\phi(y) < \phi_m$ everywhere in the channel), ρ/μ decreases as ρ_s increases. Since ρ/μ multiplies u , the axial velocity decreases, and so the particle-rich region must grow to accommodate the same particle flux down the channel.

The primary contribution to the decrease in ρ/μ is the rapid increase in the effective viscosity of the fluid, since $\phi(y)$ is close to ϕ_m . Given its effective viscosity is very high, the particle-rich fluid flows slowly. The particle-free fluid moves much faster, and hence the particle flux is much smaller than the total mixture flux, and therefore the channel carries a relatively small amount of particles per unit volume of clear fluid. Reducing the amount of fluid needed to separate a slurry is a design objective for spiral particle particle separators, so the situation we have described here would make for a poor separator.

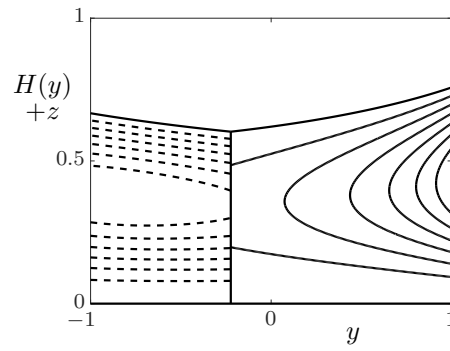
The solution shown in figure 5.8 is quite sensitive to ρ_s . As ρ_s increases, the region in the ϵ - λ plane where $\phi(y) < \phi_m$ everywhere in the channel gets smaller, so that the choice of centreline geometry becomes increasingly restricted. For valid combinations of the parameters of this problem (ϵ , λ , and ρ_s), $\phi(y)$ is relatively large, so that we are close to the limit of validity of the model equations $\phi \rightarrow \phi_m$. As $\phi \rightarrow \phi_m$, the viscosity $\mu \rightarrow \infty$. The leading order asymptotic expansions of the Navier-Stokes equations (5.3.8a) to (5.3.8c) assume that the nondimensional viscosity is $O(1)$, but this assumption fails to hold as $\phi \rightarrow \phi_m$, and so the leading order model we have used will not be valid for very high particle volume fraction.

5.6 Conclusions

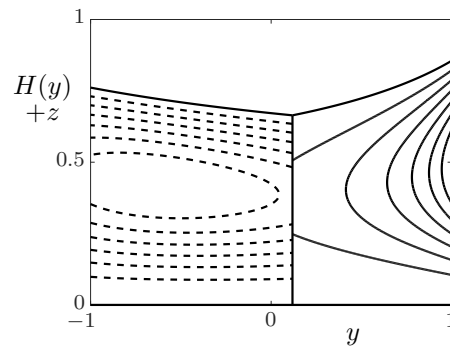
In this chapter we have introduced a particle-laden flow model, and, by modifying the equations given in chapter 2, derived a system of equations (5.2.3a)–(5.2.3c) governing particle laden flow in helically-wound channels with arbi-



(a) $\rho_s = 1.2$



(b) $\rho_s = 1.6$



(c) $\rho_s = 2$

Figure 5.8: Rectangular channels with $\epsilon = 0.2$ and $\lambda = 0.7$ carrying particles with increasing ρ_s .

trary centreline pitch and radius, and arbitrary cross-sectional shape. The thin-film scaling was used to give a much simpler system of equations (5.3.8a)–(5.3.8c), although these were still too complicated to be solved analytically. Motivated by experimental results, and a previous study (Lee et al., 2014), we restricted our attention to finding solutions with uniform particle volume fraction in the vertical direction. This assumption allowed significant analytic progress to be made, with only the free-surface differential equation requiring numerical solution. However, we found that there is a limited range of values of ϵ and λ for which such solutions exist.

The solution to the simplified system of equations gave some insights about the effect of particles on the fluid flow. The basic features of flows in helical channels that have been observed and discussed in chapters 3 and 4 still apply to particle-laden flows, but the change in the density of the fluid (due to the presence of particles) changes the balance between gravitational and inertial effects. Increasing ϵ or λ tends to push the fluid closer to the inside wall of the channel, and vice versa.

For a given flux of particles and total mixture flux, the particle-rich region can be focussed by changing the channel centreline pitch and radius. Optimal values were identified for two particular cases. The particle rich region could also be focussed by introducing a trench near the inside wall of the channel, essentially by increasing the cross-sectional area there. Commercially available spiral particle separators often feature deeper trenches near their inside wall, and our modelling is able to show the benefit in reducing y_r^* that arises from them. A claimed benefit of the trenches in commercial separators is that particles settle into them and are trapped there, however our assumption that particles are evenly distributed in the vertical direction means we cannot investigate this phenomena.

It is unlikely that the particle volume fraction in spiral particle separators is independent of depth, and some of our results point to this. We found the velocity our model predicts for the particle-rich region of the flow is very low,

with a very high effective viscosity. The optimal channel centreline geometry that minimised the radial extent of the particle-rich region was on the edge of the allowable range of ϵ and λ . This could mean that to minimise the size of the particle-rich region, ϵ and λ would be outside the range we could study, and the particles would be in the ridged or (more likely) settled regimes.

There is significant scope for further research into flows of particle laden fluids in helical channels. Numerical solutions of the thin-film system of equations (5.3.8a)–(5.3.10), with $\phi = \phi(y, z)$ would allow a wider range of channel centreline geometries to be studied, and could provide insight into the limitations mentioned in the previous paragraph. Dynamic simulations of the unsteady thin-film Navier-Stokes equations could provide significant insight into particle segregation in spiral separators, and could help verify the steady solutions we have presented here. The shear-induced migration model is not the only particle-laden flow model, and a different model (such as the suspension balance model of Nott and Brady (1994)) could be investigated.

As mentioned in section 5.5.3, the particle volume fraction can become very large, and the Krieger-Dougherty equation for the viscosity may not be realistic. The very large viscosity it predicts could potentially affect the asymptotic expansion of the governing equations. The model used in this chapter treated the slurry as a Newtonian fluid, and at very high particle volume fractions, this is not necessarily the case, and the particle-rich fluid may be better modelled as non-Newtonian or even as a granular material.

Our model is valid for monodisperse slurries, with a single species of particle, however spiral particle separators are intended to separate different species of particles. Models for flows of slurries consisting of two or more species of particles are less well understood than monodisperse slurries, and there is significant scope to improve modelling of such complex fluids.

Chapter 6

Conclusions

In this thesis, we have studied steady, helically-symmetric flow in helical channels. Starting with particle-free flow, in chapter 2, we expressed the Navier-Stokes equations in a non-orthogonal body-fitted coordinate system in which the channel bottom is a coordinate surface. In chapter 3, we took the thin-film limit of the Navier-Stokes equations, and solved the system of governing equations for channels of rectangular cross-section. In chapter 4 we extended the results from chapter 3 to shallow channels of arbitrary cross-section. Finally, in chapter 5, a model for particle-laden flow was introduced. Detailed conclusions were given at the end of each chapter, but here we summarise the important conclusions and discuss potential avenues of further research.

For channels with rectangular cross-section, studied in chapter 3, the thin-film governing equations have an analytic solution, which was used to investigate the effects of channel centreline geometry and flux down the channel. The secondary flow is always outwards at the free surface, and inwards near the channel bottom, producing a clockwise rotating cell of fluid. Increasing the slope of the channel centreline, or decreasing its radius, increases the relative effect of gravity, which pushes fluid towards the inside of the channel.

6. Conclusions

Decreasing the channel slope, or increasing the radius, tends to increase the relative effect of inertia, pushing fluid to the outside of the channel. When these effects balance, the secondary flow can break up into multiple clockwise rotating cells within a surrounding layer of clockwise rotating fluid. This effect, somewhat analagous to Dean vortices seen in helical pipe flow, is a novel result of this research and was identified as requiring further investigation for channels of arbitrary cross-section.

In chapter 4, channels with arbitrary cross-sectional shape were studied. In this case, no analytic solution could be obtained, and the free-surface differential equation had to be solved numerically. In the special case of channels with straight, sloped cross-sections and small centreline curvature and slope, analytic solutions were found. The qualitative behaviour observed in chapter 3 for rectangular channels was found to occur in channels with other cross-sections. Increasing the centreline slope and/or decreasing the centreline radius caused the fluid to move to the inside of the channel, and vice versa. A novel finding was that the free-surface was relatively insensitive to the channel cross-sectional shape, whilst the secondary flow was more sensitive. This finding is relevant to spiral particle separators, since the separation characteristics of a separator are expected to depend heavily on the secondary flow. Given small changes to the channel bottom can cause significant changes to the secondary flow, small defects in the channel bottom could have significant effects on the separation efficiency of a spiral particle separator.

At vertical channel walls, we cannot impose the no-slip boundary condition, and in practice would expect to see boundary layers form near the channel walls, with good agreement elsewhere. Stokes et al. (2013) found numerical solutions to support this hypothesis and showed that the thin-film modelling approach gave accurate and useful results away from the channel walls. In chapter 4, we approximated vertical channel walls with steeply curving walls, for which we could apply the no-slip boundary condition on the whole channel surface. Comparing the results from channels with vertical walls without no-

slip to nearly-rectangular channels with steeply curving walls, we found good agreement away from the channel walls. This suggests that even with the lack of no-slip boundary condition on vertical walls, our model can yield useful qualitative understanding. We note that in spiral particle separators, the flow is laminar in the inner region, but often turbulent near the outside wall of the channel (Holtham, 1992), and since our model assumes laminar flow everywhere it is expected that, in practice, we would see discrepancies near the outside channel wall, whether or not the no-slip condition was satisfied.

In chapter 5, the shear-induced migration model for monodisperse particle-laden flow was introduced and a system of governing equations was given. This model is very complicated, and even in the thin-film limit with a rectangular channel cannot be solved analytically. The assumption that particles disperse uniformly throughout the fluid depth was made in order to facilitate solution. The solutions featured a particle-rich region near the inside channel wall and a particle-free region elsewhere. For a given flux of particles and total mixture flux, changing the radius and pitch of the channel centreline affected the location of the interface between the particle-rich and particle-free regions. Focussing the particles into a smaller region of the channel was discussed, and optimal values of ϵ and λ given in two cases. The effect of a trench in the channel bottom in the particle-rich region of the flow was also investigated. Some shortcomings of the model were discussed in section 5.6.

There is significant potential for further research into flows in helical channels. Chapter 5 is an exploratory investigation into monodisperse particle-laden flow, and there is significant scope for future research. Numerical solution to the thin-film system of equations with $\phi = \phi(y, z)$ would provide significant insight into particle-laden flows in spiral particle separators. The shear-induced-migration model is not the only model for particle-laden flows, and other models could be considered. Flows in spiral particle separators often have a turbulent region near the outside wall, which has not been considered in this project. Turbulence is expected to have an effect on the particle transport within a spiral particle separator, and hence be important in modelling

particle separation. However, it is noted that the particles tend to move towards the inside of the channel, and the turbulent region is near the outside of the channel, so in steady state conditions the particles are not expected to be subject to turbulence. Surface tension has not been considered here, and could have an important effect on the flow, particularly where the free-surface is strongly curved. In other applications of flows in helically-wound channels, such as microfluidic spirals, surface tension is expected to play a significant role in determining the flow.

In this project, only steady-state, helically-symmetric flows have been studied, however it would be of interest to study the transition region from the inlet until the flow reaches a steady state, to determine whether the steady state profiles found in this project appear, and how long such a transition takes to occur. In the particle-laden case, dynamic simulations could help track the particle-separation process, providing insights and making predictions that could aid design of particle separators. Studying channels with geometry that changes along their length could help investigate the effects of localised disruptions or defects in the channel bottom. As discussed in chapters 4 and 5, small changes to the channel cross-sectional shape can cause significant changes to the secondary flow, and hence could potentially affect particle separation efficiency.

Bibliography

- D. J. Arnold, Y. M. Stokes, and J. E. F. Green. Thin-film flow in helically-wound rectangular channels of arbitrary torsion and curvature. *J. Fluid Mech.*, 764:76–94, 2015.
- D. J. Arnold, Y. M. Stokes, and J. E. F. Green. Thin-film flow in helically-wound shallow channels of arbitrary cross-sectional shape. *Phys. Fluids*, submitted, 2016.
- G. K. Batchelor. The effect of Brownian motion on the bulk stress in a suspension of spherical particles. *J. Fluid Mech.*, 83(1):97–117, 1977.
- G. K. Batchelor and J. T. Green. The determination of the bulk stress in a suspension of spherical particles to order c^2 . *J. Fluid Mech.*, 56(3):401–427, 1972.
- S. A. Berger, L. Talbot, and L.-S. Yao. Flow in curved pipes. *Ann. Rev. Fluid Mech.*, 15:461–512, 1983.
- C. J. Bolinder. The effect of torsion on the bifurcation structure of laminar flow in a helical square duct. *J. Fluid Eng.-T. ASME*, 117(2):242–248, 1995.
- D. Boucher, Z. Deng, T. Leadbeater, R. Langlois, M. Renaud, and K. E. Waters. PEPT studies of heavy particle flow within a spiral concentrator. *Miner. Eng.*, 62:120–128, 2014.

- D. Boucher, Z. Deng, T. Leadbeater, R. Langlois, and K. E. Waters. Speed analysis of quartz and hematite particles in a spiral concentrator by PEPT. *Miner. Eng.*, 2015.
- B. P. Cook, A. L. Bertozzi, and A. E. Hosoi. Shock solutions for particle-laden thin films. *SIAM J. Appl. Math.*, 68(3):760–783, 2008.
- S. K. Das, K. M. Godiwakka, L. Panda, K. K. Bhattacharya, R. Singh, and S. P. Mehrotra. Mathematical modeling of separation characteristics of a coal-washing spiral. *Int. J. Miner. Process.*, 84:118–132, 2007.
- P. Daskopoulos and A. M. Lenhoff. Flow in curved ducts: bifurcation structure for stationary ducts. *J. Fluid Mech.*, 203:125–148, 1989.
- W. R. Dean. XVI. Note on the motion of fluid in a curved pipe. *Phil. Mag.*, 4(20):208–223, 1927.
- W. R. Dean. Fluid motion in a curved channel. *Proc. R. Soc. Lond. A*, 121(787):402–420, November 1928.
- A. Einstein. Eine neue bestimmung der moleküldimensionen. *Ann. Phys.*, 19:289–306, 1906.
- A. C. Eringen. *Nonlinear theory of continuous media*. McGraw Hill, 1962.
- J. Eustice. Flow of water in curved pipes. *Proc. R. Soc. Lond. A*, 84(568):107–118, July 1910.
- J. Eustice. Experiments on stream-line motion in curved pipes. *Proc. R. Soc. Lond. A*, 85(576):119–131, April 1911.
- D. Gammack and P. E. Hydon. Flow in pipes with non-uniform curvature and torsion. *J. Fluid Mech.*, 433:357–382, 2001.
- M. Germano. On the effect of torsion on a helical pipe flow. *J. Fluid Mech.*, 125:1–8, 1982.

- A. B. Holland-Batt. A quantitative model of the motion of particles in the RSM/Mintek on-stream particle size analyser. *Powder Technol.*, 11:11–25, 1975.
- A. B. Holland-Batt. Spiral separation: theory and simulation. *Trans. Instn. Min. Metall. (Sect. C: Mineral Process. Extr. Metall.)*, 98:C46–C60, 1989.
- A. B. Holland-Batt. Some design considerations for spiral separators. *Miner. Eng.*, 8(11):1381–1395, 1995a.
- A. B. Holland-Batt. The dynamics of sluice and spiral separators. *Miner. Eng.*, 8(1/2):3–21, 1995b.
- A. B. Holland-Batt. A method for the prediction of the primary flow on large diameter spiral troughs. *Miner. Eng.*, 22(4):352–356, 2009.
- A. B. Holland-Batt and P. N. Holtham. Particle and fluid motion on spiral separators. *Miner. Eng.*, 4(3/4):457–482, 1991.
- P. N. Holtham. Flow visualisation of secondary currents on spiral separators. *Miner. Eng.*, 3(3/4):279–286, 1990.
- P. N. Holtham. Primary and secondary fluid velocities on spiral separators. *Miner. Eng.*, 5(1):79–91, 1992.
- I. B. Humphreys. Helical chute concentrator and the method of concentration practiced thereby. US Patent 2431559, April 1943.
- H. Ito. Flow in curved pipes. *JSME Int. J.*, 30(262):543–552, 1987.
- S. Lee, Y. M. Stokes, and A. L. Bertozzi. A model for particle laden flow in a spiral concentrator. In Y. Bai, J. Wang, and F. Daining, editors, *23rd International Congress of Theoretical and Applied Mechanics (ICTAM)*, Procedia IUTAM, 2012.
- S. Lee, Y. M. Stokes, and A. L. Bertozzi. Behaviour of a particle-laden flow in a spiral channel. *Phys. Fluids*, 26, 2014.

- D. Leighton and A. Acrivos. The shear-induced migration of particles in concentrated suspensions. *J. Fluid Mech.*, 181:415–439, 1987.
- D. G. Lynch, S. L. Waters, and T. J. Pedley. Flow in a tube with non-uniform time-dependent curvature: governing equations and simple examples. *J. Fluid Mech.*, 323:237–265, 1996.
- D. Manoussaki and R. S. Chadwick. Effects of geometry on fluid loading in a coiled cochlea. *SIAM J. Appl. Math.*, 61(2):369–386, August 2000.
- B. W. Matthews, C. A. J. Fletcher, and A. C. Partridge. Computational simulation of fluid and dilute particulate flows on spiral concentrators. *Appl. Math. Model.*, 22:965–979, 1998.
- B. W. Matthews, C. A. J. Fletcher, A. C. Partridge, and S. Vasquez. Computations of curved free surface water flow on spiral concentrators. *J. Hydraul. Eng.*, 125:1126–1139, 1999.
- N. Murisic, J. Ho, V. Hu, P. Latterman, T. Koch, K. Lin, M. Mata, and A. L. Bertozzi. Particle-laden viscous thin-film flows on an incline: Experiments compared with a theory based on shear-induced migration and particle settling. *Physica D: Nonlinear phenomena*, 240(20):1661–1673, October 2011.
- N. Murisic, B. Pausader, D. Peschka, and A. L. Bertozzi. Dynamics of particle settling and resuspension in viscous liquid films. *J. Fluid Mech.*, 717:203–231, 2013.
- P. R. Nott and J. F. Brady. Pressure-driven flow of suspensions: simulation and theory. *J. Fluid Mech.*, 275:157–199, 1994.
- F. Pardee. Separator for ore, coal, &c. US Patent 629595, July 1899.
- R. J. Phillips, R. C. Armstrong, R. A. Brown, A. L. Graham, and J. R. Abbott. A constitutive equation for concentrated suspensions that accounts for shear-induced particle migration. *Phys. Fluids A*, 4(1):30–40, January 1992.

- R. G. Richards, J. L. Hunter, and A. B. Holland-Batt. Spiral concentrators for fine coal treatment. *Coal Prep.*, 1(2):207–229, 1985.
- U. Schaffinger, A. Acrivos, and K. Zhang. Viscous resuspension of a sediment within a laminar and stratified flow. *Int. J. Multiphase Flow*, 16(4):567–578, 1990.
- J. H. Siggers and S. L. Waters. Unsteady flows in pipes with finite curvature. *J. Fluid Mech.*, 600:133–165, 2008.
- J. G. Simmonds. *A Brief on Tensor Analysis*. Undergraduate Texts in Mathematics. Springer-Verlag, 2nd edition, 1994.
- Y. M. Stokes. Flow in spiral channels of small curvature and torsion. In A. C. King and Y. D. Shikhmurzaev, editors, *IUTAM symposium on free surface flows*, volume 62 of *Fluid mechanics and its applications*, pages 289–296. Kluwer Academic Publishers, 2001a.
- Y. M. Stokes. Computing flow in a spiral particle separator. In B. B. Dally, editor, *Proceedings of the 14th Australasian fluid mechanics conference*, pages 677–680. University of Adelaide, 2001b.
- Y. M. Stokes, S. K. Wilson, and B. R. Duffy. Thin-film flow in open helically-wound channels. In M. Behnia, W. Lin, and G. D. McBain, editors, *Proceedings of the 15th Australasian fluid mechanics conference*. The University of Sydney, December 2004.
- Y. M. Stokes, B. R. Duffy, S. K. Wilson, and H. Tronnolone. Thin-film flow in helically wound rectangular channels with small torsion. *Phys. Fluids*, 25(8):083103, 2013.
- J. Thomson. On the origin of windings of rivers in alluvial plains with remarks on the flow of water round bends in pipes. *Proc. R. Soc. Lond*, 25(171–178):5–8, January 1876.
- J. Thomson. Experimental demonstration in respect to the origin of windings of rivers in alluvial plains, and to the mode of flow of water round bends of pipes. *Proc. R. Soc. Lond*, 26(179–184):356–357, January 1877.

- E. R. Tuttle. Laminar flow in twisted pipes. *J. Fluid Mech.*, 219:545–570, 1990.
- C. Y. Wang. On the low-Reynolds-number flow in a helical pipe. *J. Fluid Mech.*, 108:185–194, 1981.
- J. Wang and J. R. G. Andrews. Numerical simulations of liquid flow on spiral concentrators. *Miner. Eng.*, 7(11):1363–1385, 1994.
- K. H. Winters. A bifurcation study of laminar flow in a curved tube of rectangular cross-section. *J. Fluid Mech.*, 180:343–369, 1987.
- L. Zabielski and A. J. Mestel. Steady flow in a helically symmetric pipe. *J. Fluid Mech.*, 370:297–320, 1998a.
- L. Zabielski and A. J. Mestel. Unsteady blood flow in a helically symmetric pipe. *J. Fluid Mech.*, 370:321–345, 1998b.
- J. Zhou, B Dupuy, A. L. Bertozzi, and A. E. Hosoi. Theory for shock dynamics in particle-laden thin films. *Phys. Rev. Lett.*, 94(117803), 2005.